การปรับปรุงความสม่ำเสมอของควอนตัมด็อตแบบจัดเรียงตัวเอง ชนิดอินเดียมอาร์เซไนด์/แกลเลียมอาร์เซไนด์ โดยการปลูกผลึกด้วยลำโมเลกุล

นายสุวิทย์ กิระวิทยา

วิทยานิพนธ์นี้เป็นส่วนหนึ่งของการศึกษาตามหลักสูตรปริญญาวิศวกรรมศาสตรดุษฎีบัณฑิต
สาขาวิชาวิศวกรรมไฟฟ้า ภาควิชาวิศวกรรมไฟฟ้า
คณะวิศวกรรมศาสตร์ จุฬาลงกรณ์มหาวิทยาลัย
ปีการศึกษา 2545

ISBN 974-171-644-3

HOMOGENEITY IMPROVEMENT OF INAS/GAAS SELF-ASSEMBLED QUANTUM DOTS GROWN BY MOLECULAR BEAM EPITAXY

Mr. Suwit Kiravittaya

A Dissertation Submitted in Partial Fulfillment of the Requirements
for the Degree of Doctor of Engineering in Electrical Engineering
Department of Electrical Engineering
Faculty of Engineering
Chulalongkorn University
Academic year 2002
ISBN 974-171-644-3

Thesis Title	Homogeneity Improvement of InAs/GaAs Self-Assembled Quantum Dots Grown by Molecular Beam Epitaxy
By	Mr. Suwit Kiravittaya
Field of Study	Electrical Engineering
Thesis Advisor	Professor Dr. Somsak Panyakeow
Thesis Co-advisor	Associate Professor Dr. Montri Sawadsaringkarn
Thesis Co-advisor	Dr. Oliver G. Schmidt

Accepted by the Faculty of Engineering, Chulalongkorn University in Partial Fulfillment of the Requirements for the Doctor's Degree

………………………………………… Dean of Faculty of Engineering
(Professor Somsak Panyakeow , D.Eng.)

THESIS COMMITTEE

………………………………………… Chairman
(Professor Virulh Sa-yakanit , Ph.D.)

………………………………………… Thesis Advisor
(Professor Somsak Panyakeow , D.Eng.)

………………………………………… Thesis Co-advisor
(Associate Professor Montri Sawadsaringkarn , D.Ing.)

………………………………………… Member
(Professor Yasuhiko Arakawa , D.Eng.)

………………………………………… Member
(Karl Eberl , Ph.D.)

สุวิทย์ กิระวิทยา : การเพิ่มความสม่ำเสมอของควอนตัมด็อตแบบจัดเรียงตัวเอง ชนิดอินเดียมอาร์เซไนด์/แกลเลียมอาร์เซไนด์ โดยการปลูกผลึกด้วยลำโมเลกุล. (HOMOGENEITY IMPROVEMENT OF INAS/GAAS SELF-ASSEMBLED QUANTUM DOTS GROWN BY MOLECULAR BEAM EPITAXY) อ. ที่ปรึกษา : ศ.ดร. สมศักดิ์ ปัญญาแก้ว, อ. ที่ปรึกษาร่วม : รศ.ดร. มนตรี สวัสดิ์ศฤงฆาร และ Dr. Oliver G. Schmidt, 94 หน้า. ISBN 974-171-644-3.

วิทยานิพนธ์นี้นำเสนอวิธีการปรับปรุงความสม่ำเสมอของควอนตัมด็อตแบบจัดเรียงตัวเอง ชนิดอินเดียมอาร์เซไนด์/แกลเลียมอาร์เซไนด์ วิธีการที่ใช้สร้างโครงสร้างควอนตัมด็อต คือ การปลูกผลึกแบบจัดเรียงตัวเองในโหมดสทานสกี-คราสตานอฟ (Stranski-Krastanow) ด้วยการปลูกผลึกด้วยลำโมเลกุล วิธีวิเคราะห์ตัวอย่างชิ้นงานในการทดลองได้แก่ การวัดด้วยแรงอะตอม (Atomic Force Microscopy) และ การวัดโฟโตลูมิเนสเซนต์ (Photoluminescence) ที่อุณหภูมิห้อง

ควอนตัมด็อตที่ศึกษานี้มีทั้งชนิด ควอนตัมด็อตขนาดใหญ่ (ความสูงเฉลี่ย ประมาณ 10.7 นาโนเมตร, เส้นผ่านศูนย์กลางเฉลี่ย ประมาณ 37 นาโนเมตร) ความหนาแน่นน้อย ($3\text{-}6\times10^9$ ด็อตต่อตารางเซนติเมตร) และ ควอนตัมด็อตขนาดเล็ก (ความสูงเฉลี่ย ประมาณ 4.5 นาโนเมตร, เส้นผ่านศูนย์กลางเฉลี่ย ประมาณ 33 นาโนเมตร) ความหนาแน่นมาก (4×10^{10} ด็อตต่อตารางเซนติเมตร) ซึ่งควอนตัมด็อตที่มีขนาดต่างกันนี้ สามารถสร้างได้โดยการใช้อัตราเร็วในการปลูกผลึกชั้นอินเดียมอาร์เซไนด์เท่ากับ 0.01 และ 0.2 ชั้นอะตอมต่อวินาที ตามลำดับ ในการทดลองนี้ เราควบคุมให้อุณหภูมิปลูกชั้นควอนตัมด็อตคงที่ ที่ 500 องศาเซลเซียส และ ปริมาณอะตอมอินเดียมอาร์เซไนด์ที่ปลูกลงไปคงที่ ที่เท่ากับ 1.8 ชั้นอะตอม

ผลการศึกษาพบว่า สำหรับควอนตัมด็อตขนาดใหญ่ จะสามารถใช้การทำการขัดจังหวะหลังทำการปลูกชั้นควอนตัมด็อต เป็นเวลา 30 วินาที ก่อนทำการปลูกกลบด้วยแกลเลียมอาร์เซไนด์ ในการปรับปรุงความสม่ำเสมอของควอนตัมด็อตได้ โดยความสม่ำเสมอที่เพิ่มขึ้นนี้วัดได้ในรูปของความกว้างของสเปกตรัมโฟโตลูมิเนสเซนต์ ที่ลดลงจาก 38 มิลลิอิเล็กตรอนโวลต์ เป็น 32 มิลลิอิเล็กตรอนโวลต์ ผลการทดลองนี้สามารถอธิบายได้ด้วยปรากฏการณ์การแพร่ของอะตอมบนผิวที่ขึ้นกับพลังงานความเครียดของผิวที่มีควอนตัมด็อตอยู่ด้วย

ในกรณีควอนตัมด็อตขนาดเล็ก เราสามารถปรับปรุงความสม่ำเสมอของชั้นควอนตัมด็อตได้โดยการใช้เทคนิคการระเหยและปลูกซ้ำหลาย ๆ ครั้ง (repetitive desorption-regrowth) โดยการปล่อยให้อะตอมบนผิวระเหยออกไป แล้วทำการปลูกเพิ่มเติมลงไปหลาย ๆ ครั้งนี้ทำให้ควอนตัมด็อตที่คงอยู่บนผิว มีความสม่ำเสมอเพิ่มขึ้น จากการกระจายเชิงขนาด (ความสูง) 67% เป็น 21%

สุดท้ายนี้ เรายังสามารถปรับปรุงความสม่ำเสมอของควอนตัมด็อตทั้งสองขนาด ได้โดยการปลูกกลบชั้นควอนตัมด็อตที่อุณหภูมิต่ำ (470 องศาเซลเซียส) โดยการวัดโฟโตลูมิเนสเซนต์ ทำให้ทราบว่า ควอนตัมด็อตขนาดใหญ่ที่ปลูกกลบที่อุณหภูมิต่ำนี้เปล่งแสงที่ความยาวคลื่น 1.3 ไมครอน และมีสเปกตรัมโฟโตลูมิเนสเซนต์ กว้าง 23 มิลลิอิเล็กตรอนโวลต์ และสำหรับควอนตัมด็อตขนาดเล็ก การปลูกกลบที่อุณหภูมิต่ำนี้ ก็ทำให้ได้สเปกตรัมโฟโตลูมิเนสเซนต์แคบลงอย่างมาก (26 มิลลิอิเล็กตรอนโวลต์) เมื่อเทียบกับสเปกตรัมโฟโตลูมิเนสเซนต์ของควอนตัมด็อตขนาดเล็ก ที่ปลูกกลบที่อุณหภูมิปลูกชั้นควอนตัมด็อต (51 มิลลิอิเล็กตรอนโวลต์)

ภาควิชา ....วิศวกรรมไฟฟ้า........ ลายมือชื่อนิสิต ....
สาขาวิชา ....วิศวกรรมไฟฟ้า........ ลายมือชื่ออาจารย์ที่ปรึกษา ....
ปีการศึกษา ....2545.......... ลายมือชื่ออาจารย์ที่ปรึกษาร่วม ....
ลายมือชื่ออาจารย์ที่ปรึกษาร่วม ....

4171826021 : MAJOR ELECTRICAL ENGINEERING

KEY WORD: HOMOGENEITY / SELF-ASSEMBLED QUANTUM DOTS / INAS/GAAS / MOLECULAR BEAM EPITAXY

SUWIT KIRAVITTAYA : HOMOGENEITY IMPROVEMENT OF INAS/GAAS SELF-ASSEMBLED QUANTUM DOTS GROWN BY MOLECULAR BEAM EPITAXY. THESIS ADVISOR : PROF. DR. SOMSAK PANYAKEOW, THESIS CO-ADVISOR : ASSOC. PROF. DR. MONTRI SAWADSARINGKARN AND DR. OLIVER G. SCHMIDT, 94 pp. ISBN 974-171-644-3.

Different methods to improve the size homogeneity of InAs/GaAs self-assembled quantum dots (QDs) have been investigated in this work. The QD fabrication process relies on self-assembled growth in the Stranski-Krastanow mode by molecular beam epitaxy. The homogeneity of the QD ensembles was measured by *ex situ* atomic force microscopy (AFM) and room-temperature photoluminescence (PL).

The investigated QD arrays consist of large, low-density QDs (average height of about 10.7 nm, average diameter of about 37 nm and density of about $3\text{-}6\times10^{9}$ cm^{-2}) and small, high-density QDs (average height of about 4.5 nm, average diameter of about 33 nm and density of about 4×10^{10} cm^{-2}). The two different QD types were grown by using InAs growth rates of 0.01 and 0.2 monolayer/s, respectively. The QD growth temperature was fixed at 500°C and the amount of deposited InAs was 1.8 monolayer.

We found that for the large QDs a 30 s growth interruption prior to capping the QDs with GaAs improves the size homogeneity of the QD ensemble. The homogeneity improvement was measured in terms of PL linewidths, which narrows from 38 meV to 32 meV in case the growth interruption was introduced. This phenomenon can be explained by strain-dependent adatom diffusion processes on surface incorporated with QDs.

In case of small QDs, we improve the size homogeneity by a newly developed repetitive desorption-regrowth. By this repetitive desorption-regrowth, the QDs improve their size (height) distribution from 67% to 21%.

Finally, we improve the PL linewidth of both large and small QDs by capping at low temperature (470°C). The PL results reveal that low temperature capping of large QDs redshifts the emission wavelength to 1.3 μm with a narrow peak linewidth of 23 meV. For the small QDs low temperature capping also narrows the linewidth from 51 meV (capped at QD growth temperature) to 26 meV.

Department ......Electrical Engineering......	Student's signature ....
Field of study ......Electrical Engineering......	Advisor's signature ....
Academic year ....2002.........	Co-advisor's signature ....
	Co-advisor's signature ....

Acknowledgements

The author would like to give special thanks to his family for endless and encouraging support throughout this work.

The author gratefully acknowledges all those who provided invaluable help and encouragement during the research both at the Semiconductor Device Research Laboratory (SDRL), Department of Electrical Engineering, Faculty of Engineering, Chulalongkorn University, Bangkok, Thailand and at the MBE group, Max-Planck-Institute for Solid State Research, Stuttgart, Germany. In particular, the author is deeply indebted to Professor Dr. Somsak Panyakeow, Associate Professor Dr. Montri Sawadsaringkarn, and Dr. Oliver G. Schmidt, who are the advisor and co-advisors; as well as also Dr. Karl Eberl, Professor Dr. Ignaz Eisele, Associate Professor Dr. Choompol Anterasena, Assistant Professor Dr. Somchai Ratanathammaphan, and Assistant Professor Dr. Songphol Kanjanachuchai.

As always, this thesis could not have been completed without special helps of colleagues and members in the MBE group and the SDRL. These are colleagues at Max-Planck-Institute: Dr. Yusui Nakamura, Mrs. Claudia Müller, Mr. Henry Heidemeyer, Ms. Yvonne Manz, Mr. Ulrich Denker, Mr. Karsten Tötemeyer, Mr. Wolfgang Winter, Dr. Michael W. Dashiell, Mr. Christoph Deneke, Dr. Martin O. Lipinski, Dr. Neng Yun Jin-Phillipp, and colleagues at Chulalongkorn University: Mr. Supachok Thainoi, Dr. Suwat Sopitpan, Mrs. Kwanruan Thainoi. In addition, the author would like to thank for seamless collaboration with Ms. Rudeesun Songmuang at both Chulalongkorn University and Max-Planck-Institute.

Special thanks go to the Royal Golden Jubilee (RGJ) scholarship for the research fund in Thailand and DAAD-RGJ scholarship for funding of a the short research program at Max-Planck-Institute for Solid State Research, Stuttgart, Germany.

CONTENTS

CONTENTS (continued)

LIST OF FIGURES

LIST OF FIGURES (continued)

Page

LIST OF FIGURES (continued)

Page

LIST OF FIGURES (continued)

LIST OF FIGURES (continued)

LIST OF FIGURES (continued)

Page

LIST OF FIGURES (continued)

LIST OF FIGURES (continued)

LIST OF FIGURES (continued)

LIST OF FIGURES (continued)

LIST OF SYMBOLS

∇^2	Laplacian operator
α	control parameter
a	hydrostatic deformation potential
a_e	lattice constant of deposited material
a_S	lattice constant of substrate material
A	surface area
AFM	atomic force microscopy
AlAs	aluminium arsenide
AlGaAs	aluminium gallium arsenide
AlP	aluminium phosphide
$AsBr_3$	arsenic tribromide
b	valence band (001) axial deformation potential or base of pyramidal quantum dot
CB	conduction band
CC	conventionally capped
CEO	cleaved edge overgrowth
δ	delta function
Δ	total spectrum broadening from all excited quantum dot
$\Delta\gamma$	change of surface free energy
ΔE_g	shift of conduction band minimum due to strain
$D_\mathrm{bulk}(E)$	bulk density of state
$D_\mathrm{QW}(E)$	quantum well density of state
$D_\mathrm{QWR}(E)$	quantum wire density of state
$D_\mathrm{QD}(E)$	quantum dot density of state
D.O.S.	density of state
ε	misfit
ε_0	lattice mismatch
ε_ax	uniaxial strain component
ε_vol	hydrostatic strain component
ε_xx	axial strain in x-direction

LIST OF SYMBOLS (continued)

ε_{yy}	axial strain in *y*-direction
ε_{zz}	axial strain in *z*-direction
ε_{xz}	shear strain on *x*-plane directed through *z*-direction
ε_{xy}	shear strain on *x*-plane directed through *y*-direction
ε_{yz}	shear strain on *y*-plane directed through *z*-direction
$\varepsilon_{//}$	in-plane strain
$\varepsilon_{\perp}$	strain in perpendicular to the growth direction
E	carrier energy or total energy per unit cell
E_0	characteristic energy
E_g	band gap energy
$E_{l,x}$	quantized energy in *x*-direction
$E_{m,y}$	quantized energy in *y*-direction
$E_{n,z}$	quantized energy in *z*-direction
$E(\mathrm{el})$	elastic strain energy
E_{WL}	energy of wetting layer
E_{rip}	energy of ripened island
E_{island}	energy of single island
E_{elastic}	elastic strain energy
E_{surface}	island surface energy
E_{edge}	island edge energy
$F(\mathbf{r})$	envelope wave function
FWHM	full width at half maximum
γ_e	surface free energy of the epilayer/vacuum interface
γ_i	surface free energy of epilayer/substrate interface
γ_S	surface free energy of the substrate/vacuum interface
g^{sat}	maximum optical gain
$\boldsymbol{G}$	reciprocal lattice vector
GaAs	gallium arsenide
GaP	gallium phosphide
Ge	germanium

LIST OF SYMBOLS (continued)

GI	growth interruption
h	Planck's constant
	or height of pyramidal quantum dot
$\hbar$	reduced Planck's constant
h_c	critical thickness of strained layer
HH	heavy-hole band
i	critical island size
InAs	indium arsenide
InGaAs	indium gallium arsenide
InGaP	indium gallium phosphide
InP	indium phosphide
k	amplitude of wave vector
k_B	Boltzmann's constant
$k_{//}$	amplitude of in-plane (y-z) wave vector
$k_{\perp}$	amplitude of wave vector in x-direction
$\mathbf{k} = (k_x, k_y, k_z)$	carrier wave vector
$\boldsymbol{k}_{in}$	wave vectors of incident electron
$\boldsymbol{k}_{diff}$	wave vectors of diffraction electron
λ	elastic modulus
$\lambda_{de\ Broglie}$	de Broglie wavelength
l	quantum number in x-direction
L	macroscopic length scale
	or base size of pyramidal quantum dot
L_0	characteristic length
L_{opt}	optimal island size
L_x	nanometer length scale in x direction
L_y	nanometer length scale in y direction
L_z	nanometer length scale in z direction
LH	light-hole band
LTC	low temperature capping, low temperature capped

LIST OF SYMBOLS (continued)

m	quantum number in y-direction
m^*	effective mass
m_{eff}	carrier effective mass
MBE	molecular beam epitaxial
	or molecular beam epitaxy
MFC	mass flow controller
ML	monolayer
Mo	molybdenum
n	quantum number in z-direction
N_D	volume density of quantum dot
N_{e}	number of state per unit surface
N_{wi}	area density of quantum wire
p	carrier momentum
PBN	pyrolytic boron nitride
PL	photoluminescence
Q	total deposited material (monolayer)
Q_1	deposited material that form wetting layer
Q_2	deposited material that form coherent 3D island
QW	quantum well
QWR	quantum wire
QD	quantum dot
ρ	quantum dot density
r_{GaAs}	growth rate of gallium arsenide
r_{InAs}	growth rate of indium arsenide
r_{InGaAs}	growth rates of indium gallium arsenide
$\mathbf{r} = (x, y, z)$	carrier position vector
RHEED	reflection high-electron energy diffraction
Re	rhenium
RT	room temperature
σ	Poisson’s ratio
sccm	standard cubic centimeter

LIST OF SYMBOLS (continued)

Si	silicon
SiGe	silicon germanium
SO	spin-split-off band
STM	scanning tunneling microscopy
Θ	Heaviside’s unit step function
t	film thickness
T	temperature
$V(\mathbf{r})$	confinement potential
W	tungsten
WL	wetting layer

CHAPTER 1

Introduction

1.1 Historical Background

Semiconductor technology has been rapidly developed since the invention of solid-state transistor in 1947. Since electronic properties of semiconductors are tunable, several novel device concepts have been demonstrated and resulted in many applications, especially in electronics and optoelectronic fields. Starting with a semiconductor material (e.g. Si, GaAs), elaborate processing yields a number of useful electronic devices. However, device structures based on a single material, i.e., *homostructure*, have some limitations due to intrinsic nature of the material properties.

During the last decade, *heterostructure* has emerged and has been shown to improve the properties of many devices. By combining two different materials, energy band offset can be used to confine charge carriers in one or more directions. Device properties can thus be changed in controllable directions. Engineering of material systems and device structures can overcome some limitations presented in homostructure technologies. An example of which can be seen in a laser fabricated using heterostructure. Such lasers exhibit low threshold current due to charge carrier confinement in the active region. The importance of the technology has been recognized: Kroemer and Alferov were awarded the Nobel prize in Physics in 2000 for their work on semiconductor heterostructures used in high-speed- and opto-electronics.

In optoelectronics, GaAs is a well-developed material system. Comparing with II-VI and other III-V based materials, GaAs is easy to fabricate and has suitable mechanical properties. Several novel optoelectronic devices based on GaAs have been realized as a result. In addition, epitaxial growth of semiconductor structure has been developed using this material (e.g. Cho, 1983). However, there are some disadvantages in using GaAs material system. For example, it is lattice matched to only AlGaAs. The corresponding wavelengths of GaAs-based optical devices lie between 625 nm ($Al_{0.45}Ga_{0.55}As$) and 870 nm (GaAs). Therefore, the applications of GaAs-based devices in optoelectronics are limited to visible and near-infrared spectrum ranges.

There are intensive studies on the growth of high-quality InGaAs layer on GaAs. The materials are about 7% lattice mismatch. The growth of InGaAs layer is limited to a critical thickness before the relaxation, which believed to cause defect formation. In 1993, Leonard et al. investigated the growth of InGaAs, with high indium content (50%), on GaAs (001) substrate at beyond the critical thickness. They found that the quantum-sized islands were obtained during the initial state of the growth. These grown islands were dislocation-free and acted as three-dimensional carrier confinement structure or so-called self-assembled quantum dot (QD). Due to the simplicity of this growth technique, several groups started to fabricate the self-assembled QD for novel device applications. However, the QDs formed by this specific growth mode experienced large size fluctuations, which limits the realization of device with improved performance. To minimize the size fluctuation, growth parameters have to be well understood and optimized. Special growth techniques were proposed to minimize the size distribution; for example, Yamaguchi et al. (2000) proposed the tuning of arsenic pressure to utilize the self size-limiting effect while Nishi et al. (1999) proposed the strain reduction in QDs by growth of InGaAs capping layers.

1.2 Objective

The objective of this work is to develop different methods to improve the size homogeneity of InAs/GaAs self-assembled QDs. Our methods focus on the modification of the QD growth conditions and on the control of the QD evolution after their formation.

1.3 Overview

This thesis presents a detailed study of the growth of InAs/GaAs self-assembled QDs by molecular beam epitaxy (MBE). The main purpose is to explore the physics of the growth phenomena and to improve the size uniformity of these self-assembled QD structure.

The thesis is organized as follows: The basic concepts of low-dimensional nanostructures are reviewed in chapter 2. This also includes fabrication techniques and theories of self-assembled QD formation. Chapter 3 gives the experimental details. In chapter 4, results from experiments on the growth of InAs/GaAs self-assembled QDs are presented. The effects of amount of material deposition, growth rate, and capping layer are studied in this chapter. The studies are based on atomic force microscopy (AFM) and photoluminescence (PL) results. Main results of this thesis are presented in chapter 5 whose several techniques to improve size homogeneity are shown. The techniques involve growth interruption, repetitive desorption-regrowth, low temperature capping, and *in situ* etching. These techniques can be used to improve the homogeneity of either large or small QD arrays. Finally, chapter 6 concludes this work.

CHAPTER 2

Zero-Dimensional Nanostructures: Quantum Dots

The basic concepts of quantum dot (QD) structure, which is a low-dimensional semiconductor nanostructure, are reviewed in this chapter. A comparison of important intrinsic properties of nanostructures is presented. The effects of strain on the band structure are reviewed because of their importance for the description of self-assembled QDs.

In another part of this chapter, several methods to fabricate the QD structure are presented based on epitaxial growth and/or patterning processes. The method includes combination of lithography and etching techniques, selective growth of QDs, *in situ* cleaved edge overgrowth techniques, and self-assembled growth. Finally, the theories about the self-assembled growth, which is the method used to fabricate the QDs in this thesis, are presented.

2.1 Basic Concepts of Low-Dimensional Nanostructures

It is generally known that the band theory of crystals has been rigidly developed from the quantum theory for atoms since the last century (See e.g. Yu and Cardona, 1999; Kittel, 1996). From the quantum theory, we know that when we place atoms, which have discrete energy levels, together then they become solid. The energy levels of solid crystal become energy bands. There are several bands in a solid crystal structure. From the engineering point of view the most relevant bands are the conduction band and the valence band which are separated in energy by the band gap. The conduction band is free of electrons at 0 K, while the valence band is full with electron at 0 K. At $T > 0$ K, these two bands are partially filled with electrons and holes, which act as charge carriers in devices operations. Controlling the carrier motion in these two bands is the subject of band gap engineering. We, therefore, consider only these two bands.

In low-dimensional nanostructures large carriers are spatially confined in one or more directions and the length scale in confining direction is in the order of the de Broglie wavelength (carrier wavelength). The de Broglie wavelength, $\lambda_{\text{de Broglie}}$, depends on the carrier effective mass, m_{eff}, and temperature, T:

$$\lambda_{\text{de Broglie}} = h/p = h/\sqrt{(3\, m_{\text{eff}}\, k_B T)} \qquad (2.1)$$

where h is Planck's constant, p is carrier momentum, and k_B is Boltzmann's constant. The de Broglie wavelength for electrons in III-V semiconductor materials is in the order of 20 nm at 300 K. Several aspects of carrier confinement effects (i.e. physics of low-dimensional nanostructure) are useful for semiconductor device applications. For example, intersubband transition of carrier in quantum well structure can be used to realize GaAs-based far-infrared detectors, which operate at wavelength beyond 9 μm (Cheng, 1999).

Figure 2.1 shows a schematic comparison between a bulk semiconductor, a waveguide for visible light, a QD, and an atom. The structural size of the QD should be comparable to the de Broglie wavelength. The condition is analogous to the waveguide structure, which should be in the micrometer range to confine the light with micrometer wavelength. The electronic structure of the bulk material

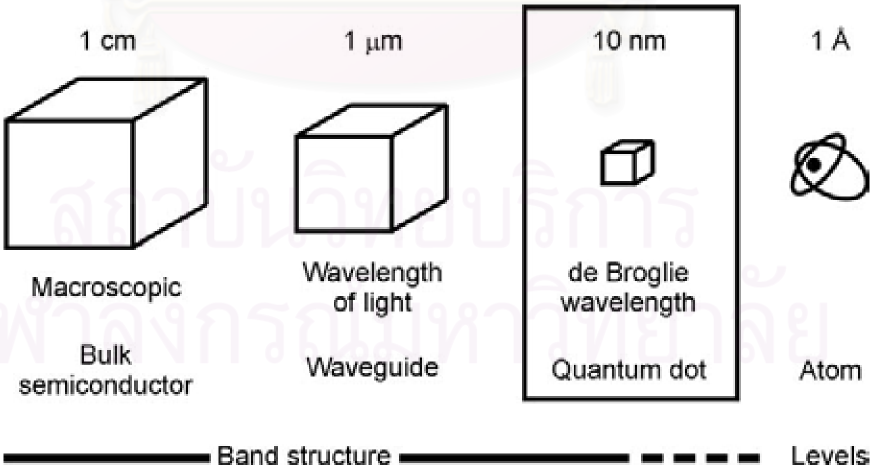

Figure 2.1 Schematic comparison of typical dimensions of bulk semiconductor, waveguide for visible light, QD, and atom (Redrawn from Bimberg et al., 1999).

and the atom are different. The electronic structure in the case of the atom is described by discrete energy levels, while in the case of the bulk-crystal structure we use band theory. Because the structural size is varied continuously, there exists a description between the two cases (discrete levels and continuum band structure).

The densities of states of bulk semiconductor and low-dimensional nanostructures are illustrated in Figure 2.2 (Sugawara, 1999). The band offsets between the low-dimensional nanostructures and the surrounding material provide the energy potential to confine the carriers. In case of a type I band alignment, in which electrons and holes are confined in the same material, the potential height is defined by the band offset in the conduction or valence bands (Weisbuch and Vinter, 1991; Esaki, 1986). Electrons and holes in a quantum well can freely move in the *x-y* plane; those in a quantum wire can only move in *x* direction. In a QD, the charge carriers are completely localized. This 3-D confinement results in a quantization of the carrier energy and in a variation of the carrier density of states.

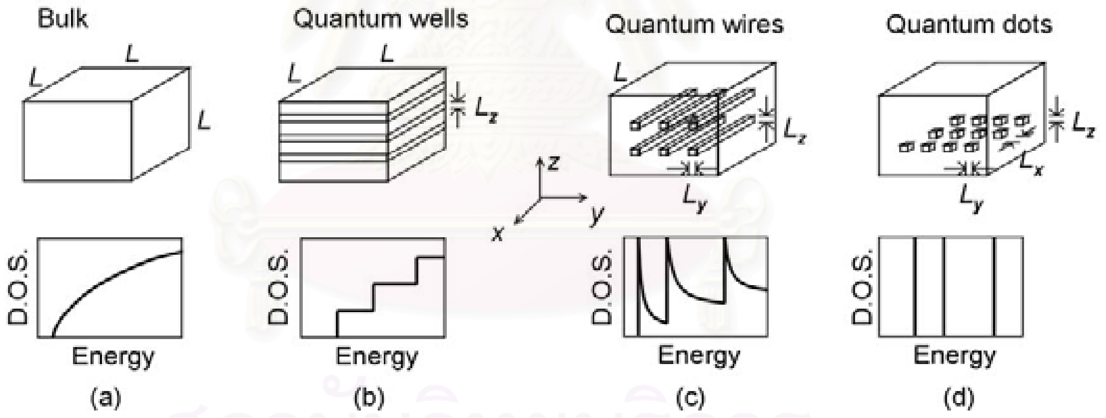

Figure 2.2 Schematic views and graphs of (a) bulk, (b) quantum wells, (c) quantum wires, and (d) QD and their density of states (D.O.S.). *L* is in macroscopic scale (~cm), while L_x, L_y, L_z, are in nanoscale (Sugawara, 1999).

An effective-mass approximation can effectively describe the electronic states of bulk semiconductors (Wolfe et al., 1989). In semiconductor quantum wells, this approximation is widely used for the calculation of quantized energy levels (Bastard and Brum, 1986). The calculation results have been confirmed by experimental data based on optical measurement techniques (Weisbuch and Vinter, 1991). The main assumption of the effective-mass approximation is that the envelope wave function does not significantly vary in the unit cell with a length scale of subnanometers; this assumption applies to all low-dimensional nanostructures like those in Figure 2.2. Assuming parabolic band dispersion, band-edge electron states of semiconductors can be described by the Schrödinger equation as

$$\left[-\frac{\hbar^2}{2m^*}\nabla^2 + V(\mathbf{r})\right]F(\mathbf{r}) = E\,F(\mathbf{r}) \tag{2.2}$$

Here m^* is the effective mass, $\hbar$ is the reduced Planck's constant, $\mathbf{r} = (x,y,z)$ is the carrier position vector, $V(\mathbf{r})$ is the confinement potential due to band offset; $F(\mathbf{r})$ is the envelope wave function, and E is the carrier energy.

From eq. (2.2), the carrier energy E in case of bulk, quantum well (QW), quantum wire (QWR) and QD can be written as

$$E_{\text{bulk}} = E(\mathbf{k}) = \frac{\hbar^2 k^2}{2m^*} \tag{2.3}$$

$$E_{\text{QW}} = E(\mathbf{k}) = \frac{\hbar^2 {k_{//}}^2}{2m^*} + E_{n,z} \tag{2.4}$$

$$E_{\text{QWR}} = E(\mathbf{k}) = \frac{\hbar^2 {k_{\perp}}^2}{2m^*} + E_{m,y} + E_{n,z} \tag{2.5}$$

$$E_{\text{QD}} = E_{l,x} + E_{m,y} + E_{n,z} \tag{2.6}$$

where $\mathbf{k} = (k_x, k_y, k_z)$ is the wavevector of carriers, $k^2 = k_x^2 + k_y^2 + k_z^2$, ${k_{//}}^2 = k_x^2 + k_y^2$, and ${k_{\perp}}^2 = k_x^2$. The energies $E_{l,x}$, $E_{m,y}$, and $E_{n,z}$, which are a function of the potential $V(\mathbf{r})$, depend on the quantum numbers l, m, and n. These energies can be determined by solving eq. (2.2) using either analytical method (with some approximations) or numerical methods.

The density of states per unit volume (D.O.S.), which is the number of states between the energy *E* and *E* + *dE*, of each quantum nanostructure is written as (Sugawara, 1999)

$$D_{\text{bulk}}(E) = \frac{1}{2\pi^2}\left(\frac{2m^*}{\hbar^2}\right)^{3/2} E^{1/2} \qquad (2.7)$$

$$D_{\text{QW}}(E) = \frac{m^*}{\pi\hbar^2}\sum_n \Theta(E - E_{n,z}) \qquad (2.8)$$

$$D_{\text{QWR}}(E) = \frac{N_{wi}}{\pi}\frac{\sqrt{2m^*}}{\hbar}\sum_{m,\,n}\frac{1}{\sqrt{E - E_{m,y} - E_{n,z}}} \qquad (2.9)$$

$$D_{\text{QD}}(E) = 2N_D \sum_{l,\,m,\,n}\delta(E - E_{l,x} - E_{m,y} - E_{n,z}) \qquad (2.10)$$

where Θ is the Heaviside's unit step function, N_{wi} is the area density of the quantum wires (the number of quantum wires divided by the quantum-wire region area in the *y*-*z* plane), δ is the delta function, and N_D is the volume density of the QD. The density of states in eqs. (2.7)-(2.10) are schematically shown with the corresponding structures in Figure 2.2. It is noteworthy that since the delta-function-like density of states of the QD structure is similar to the discrete energy levels of atoms; the QD structure is sometimes called *artificial atom*.

The ideal cases described above exclude several phenomena, which may occur during the fabrication of the nanostructures, especially during the growth process. In case of QDs, there are a number of phenomena that modify both the structural and the electronic properties, which will be considered in detail later.

The change of density of states for the low-dimensional nanostructures (Figure 2.2) considerably affects the fundamental properties of the devices, which use these nanostructures as an active layer (Arakawa and Sakaki, 1982). In case of the QD structures, there are several theoretical and experimental proves that semiconductor lasers based on QDs experience the lowest threshold current density due to the delta-function-like density of states (Asada et al., 1986). Expectedly, QD lasers provide the lowest threshold current density of 13 A/cm^2 (Eliseev et al., 2001). Figure 2.3 shows the historical evolution of the threshold current of semiconductor lasers (Alferov, 2001). Extensive reviews of the development QD lasers are given by Grundmann (2000) and Alferov (2001).

To utilize QDs as an active layer for semiconductor lasers, there are two particularly important considerations. Firstly, the density of QDs must be high enough to achieve the lasing condition (gain overcomes the loss). Secondly, the QD size distribution should be narrow since the optical gain spectra depend on the size distribution. In other words, QDs should have the same size in order to reduce the charge carriers needed for the population inversion condition. The maximum optical gain, g^{sat}, for a QD laser can be written as (Zhukov et al., 2000)

$$g^{sat} \propto N_e/\Delta \qquad (2.11)$$

where N_e is the number of states per unit surface. For the ground level, N_e is equal to the doubled surface density of the QD array, N_D. Δ is the total spectrum broadening from all excited QDs. From eq. (2.11), it is possible to increase the maximum optical

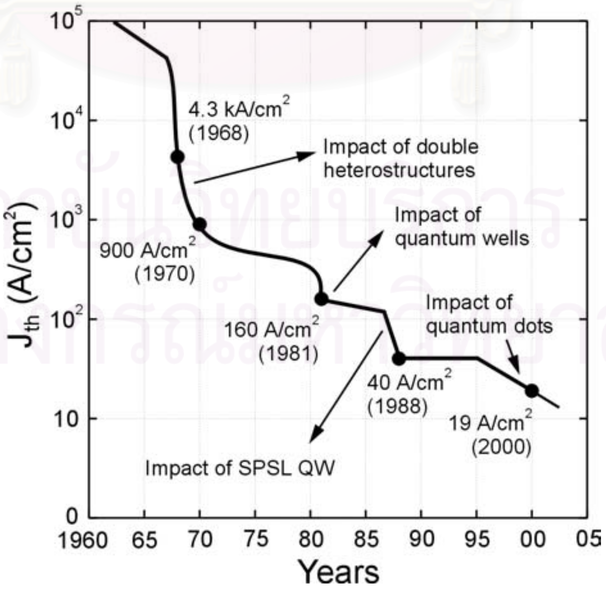

Figure 2.3 Evolution of the threshold current of semiconductor lasers (Alferov, 2001).

gain by increasing the QD density and/or reducing the size distribution of the QD ensemble.

In summary, we introduced the concept of low-dimensional nanostructures, i.e. QWs, QWRs, and QDs compared with bulk semiconductors. The general theoretical view of the size and the electronic properties, i.e., density of states was presented. The QD laser was briefly introduced. In the next section, the effect of strain on the band structure of QDs is presented.

2.2 Strain Effects on Low-Dimensional Nanostructures

As self-assembled QDs are obtained by highly lattice mismatched heteroepitaxy, it is important to understand the effects of strain on the material properties. Figure 2.4 shows the structural aspects of lattice-matched and lattice-mismatched system. In the case of lattice-matched epitaxy, the deposited material has *almost* the same lattice constant as that of the substrate material, e.g. AlGaAs/GaAs. If the deposited material has a different lattice constant from the substrate, it induces stress/strain to the system. The strain is classified into two types namely compressive (Figure 2.4(b)) and tensile (Figure 2.4(c)).

During coherent growth of the layers, the deposited atoms match the in-plane lattice constant of the substrate material, as schematically shown in the lower panel of Figure 2.4(b) and (c). This condition induces the biaxial stress (force) in the lateral direction. The in-plane strain, $\varepsilon_{//}$, is given by

$$\varepsilon_{//} = \varepsilon_{xx} = \varepsilon_{yy} = (a_s - a_e)/a_e \qquad (2.11)$$

where a_e is the lattice constant of the deposited material and a_s is the lattice constant of the substrate. The biaxial stress also changes the lattice constant of the deposited material in growth direction. The strain in the growth direction is defined as

$$\varepsilon_{\perp} = \varepsilon_{zz} = -\,(2\,\sigma\,/\,(1-\sigma))\,\varepsilon_{//} \qquad (2.12)$$

where σ is Poisson's ratio. For tetrahedral semiconductors, σ is approximately 1/3, so

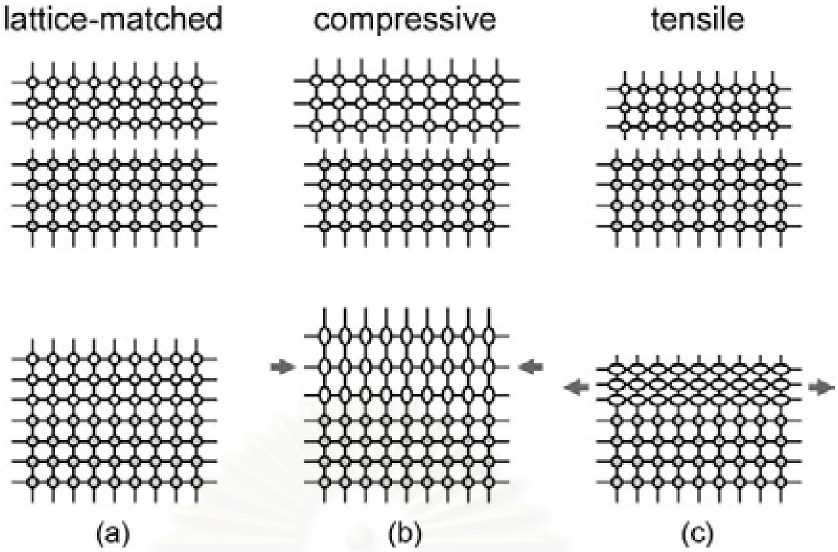

Figure 2.4 Schematic representation of (a) unstrained layer, (b) compressive strained layer, and (c) tensile strained layer. The closed circles represent atoms of the substrate material and the open circles are atoms of the deposited material. In (b) and (c) the lattice constant of the deposited material are different from the epitaxial layer. The arrows in (b) and (c) represent forces (stresses) exerted on the epitaxial layer.

that $\varepsilon_{\perp} \approx \varepsilon_{//}$. The total strain can be described by a uniaxial component, ε_{ax},

$$\varepsilon_{ax} = \varepsilon_{\perp} - \varepsilon_{//} \tag{2.13}$$

and a hydrostatic component ε_{vol} (= $\Delta V/V$),

$$\varepsilon_{vol} = \varepsilon_{xx} + \varepsilon_{yy} + \varepsilon_{zz} \approx \varepsilon_{//} \tag{2.14}$$

ε_{ax} and ε_{vol} are the terms used to predict the band gap of strained layers by deformation potential theory.

Deformation potential theory is limited to coherent growth of strained layer. Therefore, if one deposits strained material beyond a critical thickness, the total energy exceed the energy of the relaxed system. The relaxation process occurs. This usually forms dislocation defect. The critical thickness of the strained layer h_c was first studied by Frank and van der Merwe in thermodynamic equilibrium. This value depends on several parameters, not only on material properties but also on growth conditions. The theoretical and experimental data on this subject can be found in many references (O'Reilly, 1989; Morkoç et al., 1993; Tsao, 1993; Pimpinelli and Villain, 1998).

The effects of strain on the band structure can be expressed in terms of deformation potentials. The conduction band is shifted upwards for compressive strain and downwards for tensile strain. From the deformation potential theory (O'Reilly, 1989), the conduction band minimum is shifted with respect to the average valence band energy by

$$\Delta E_{\mathrm{g}} = a\,\varepsilon_{\mathrm{vol}} \tag{2.15}$$

where *a* (eV) is the hydrostatic deformation potential. The heavy-hole and light-hole bands, which are initially degenerated, decoupled and shifted in opposite directions as depicted in the Figure 2.5. The heavy-hole band shifts by an energy *S* with respect to the mean valence band edge energy. The energy *S* depends on the uniaxial strain as

$$S = -b\,\varepsilon_{\mathrm{ax}} \tag{2.16}$$

where *b* (eV) is the valence band (001) axial deformation potential. In the case of a strained quantum well structures, the energy band diagram of the valence band can be schematically drawn as shown in the lower part of Figure 2.5. Note that the actual number of quantized energy levels of both heavy holes and light holes also depend on the size of the structure and the material parameters.

For the case of self-assembled QD structure, the strain distribution is more complicated due to the three-dimensional nature of this structure. This strain distribution has been widely calculated by several groups (Wang and Zunger, 1999; Bimberg et al., 1999) based on various approaches such as using Green's tensor (Faux and Pearson, 2000). However, the lack of knowledge in exact QD shape, size and composition hinders the accurate prediction of this effect. A numerical calculation for a pyramidal QD using finite difference scheme by Bimberg et al. (1999) is given in Figure 2.6.

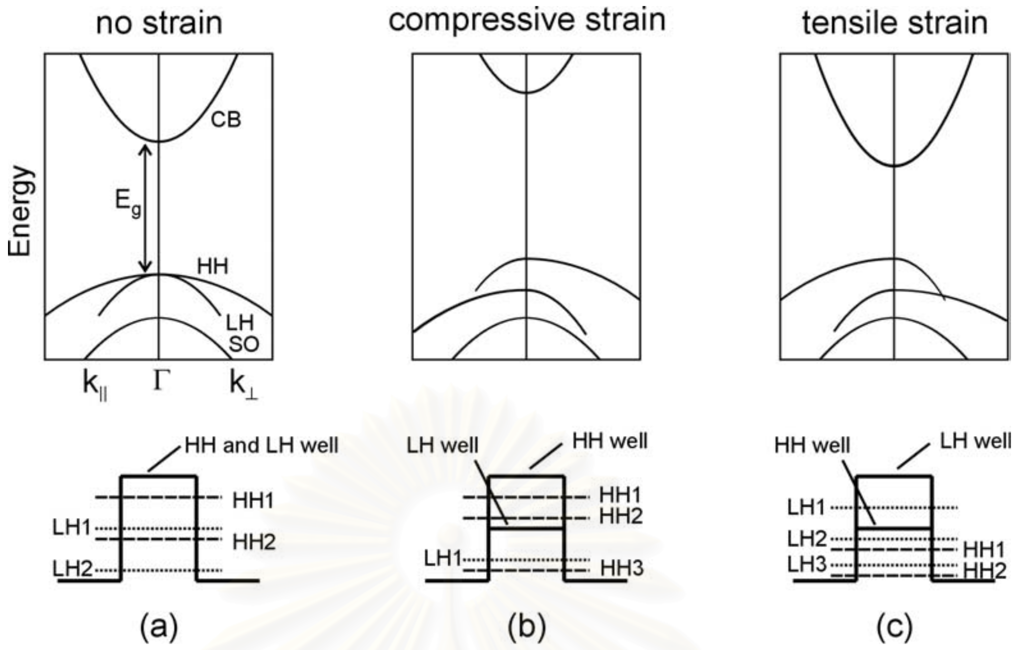

Figure 2.5 (a) A schematic representation of the band structure of an unstrained direct-gap tetrahedral semiconductor. The light-hole (LH) and heavy-hole (HH) bands are degenerate at the Brillouin zone centre Γ and the spin-split-off (SO) band lies lower in energy. The lowest conduction band (CB) is separated by the band gap energy E_g from the valence bands. Note that the $\boldsymbol{k}_{\|}$ is perpendicular to the growth and strain direction. (b) Under biaxial compression, the hydrostatic component of the compression increase the mean band gap, while the uniaxial component splits the degeneracy of the valence band maximum and introduce an anisotropic valence band structure. (c) Under biaxial tension, the mean band gap reduces and the valence band splitting is reversed. The lower panel shows the valence band diagram of the quantum well structure in case of (a) unstrained, (b) compressive strained, and (c) tensile strain. (Redrawn from O'Reilly, 1989)

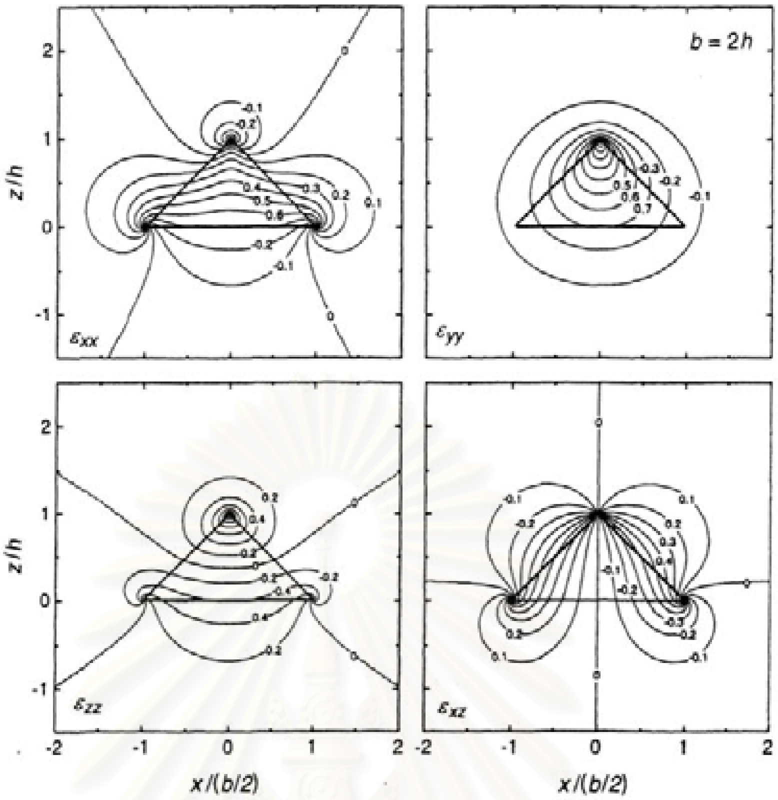

Figure 2.6 Strain distribution for a pyramidal QD with a 45° facet angle in the (*xz*) plane through the pyramid top. Identical isotropic elastic constants and σ = 1/3 are taken throughout the structure. ε_{xx}, ε_{yy}, ε_{zz}, ε_{xz} are shown; due to symmetry in this plane, ε_{xy}, and ε_{yz}, are zero. (Bimberg et al., 1999)

Although the most obvious effect of strain is a change in the band structure. Other effects such as piezoelectric effects need to be considered for detailed investigations (Davies, 1998; Pan and Yang, 2002).

2.3 Quantum Dot Fabrication Methods

In this section, different examples of QD fabrication methods are presented. This includes are lithographic patterning and etching of the quantum-well structure, growth on nonplanar patterned substrate, and cleaved-edge overgrowth. The self-assembled growth of QDs is explained in more detail in the next section.

2.3.1 Lithographic Patterning and Etching of the Quantum Well Structures

Figure 2.7 shows a schematic of the fabrication procedure for a free-standing QD. In Figure 2.7(a), the one-dimensional carrier confinement or the quantum well structure is initially grown by conventional growth techniques such as molecular beam epitaxy (Chapter 3) or metal-organic chemical vapor deposition. The layer structure is usually lattice-matched AlGaAs/GaAs. Later the nanoscale lithographic patterning is *ex situ* performed as shown in Figure 2.7(b). Typically, the pattern is an array of holes or dots depending on the type of photoresist. The conventional technique to realize the pattern is e-beam lithography because it has the highest resolution limitation among other lithography techniques. Finally, dry or wet etching is used to fabricate a free-standing QD.

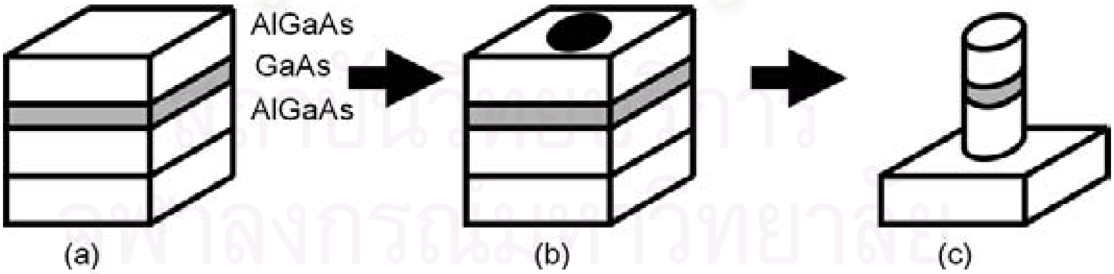

Figure 2.7 Sequence of fabrication procedure for a QD fabricated by lithographic patterning and etching of a quantum well structure. The quantum well structure is first grown (a), then the nanoscale pattern is lithographically transferred to the sample (b). Finally, etching is performed to provide carrier confinement in lateral directions (c) (Bimberg et al., 1999).

However, the surrounding surface of the QD fabricated by this method is substantially damaged during the etching process, which make these QDs useless for optical investigation or device fabrication. Moreover, due to the limited resolution of the lithography, the confinement is weak and quantum effects can only be observed at low temperatures.

2.3.2 Growth on Nonplanar Patterned Substrate

Three-dimensional carrier confinement can also be realized by the growth on nonplanar patterned substrates as demonstrated by Rajkumar et al. (1993). A schematic of this growth technique is shown in Figure 2.8. First, truncated triangular-based pyramidal mesas are created using patterning by conventional photolithography, followed by wet chemical etching of a (111)B GaAs substrate. The obtained mesas have {100} sidewalls and top lateral dimension less than 1 μm. Then, cleaning and growth on this patterned structure is performed. Due to the fact that the growth rates on each plane are different, the QD structure can be realized by changing the deposited material during growth.

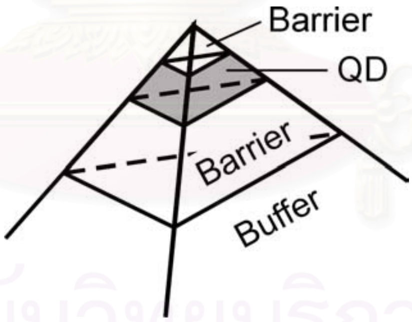

Figure 2.8 Growth on nonplanar patterned substrates. First the nonplanar substrate ((111)B GaAs in this case) is patterned by conventional photolithography and wet chemical etching. Truncated triangular-based pyramidal mesas with top lateral dimensions less than 1 μm are created. After growth, three-dimensionally confined structure (QD) are realized. (Bimberg et al., 1999)

By using this technique, defect-free QDs can be fabricated but the lateral size of the microscale mesa structure prevents the realization of high-density QD arrays. The high density is also important for QD device applications as stated in Section 2.1.

2.3.3 Cleaved Edge Overgrowth

A technique to realize QD structures without using patterning is given by two-fold cleaved edge overgrowth (Grundmann and Bimberg, 1997; Wegscheider et al., 1997). The schematic representation of the technique is shown in Figure 2.9. In Figure 2.9(a), the one-dimensional quantum well structure is grown by conventional growth techniques. Cleaved edge overgrowth has been used to fabricate T-shaped quantum wires, which develop at the junction of two quantum well planes (Figure 2.9 (b)). The junctioning between three quantum well layer planes, which can be fabricated by twofold cleaved edge overgrowth, acts as an electronic QD (Figure 2.9 (c)). However, a weak confinement of only 10 meV and the tedious fabrication procedure prevents a use on any applications.

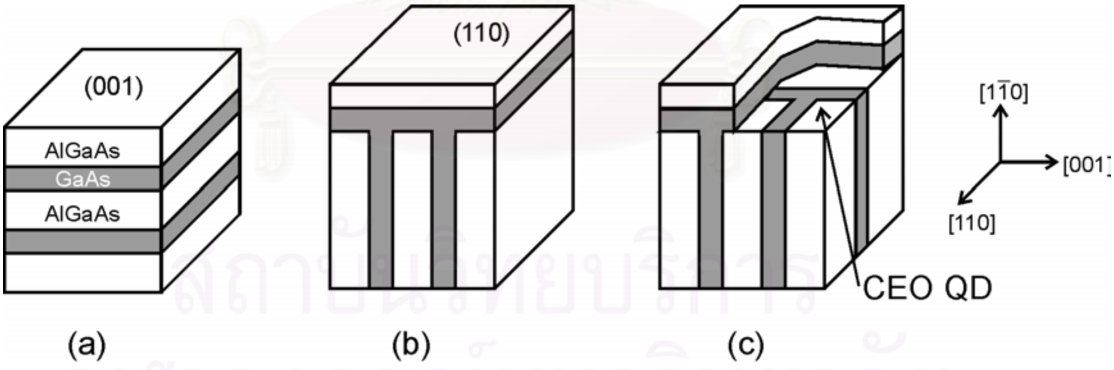

Figure 2.9 Sequence of fabrication procedure for QD fabricated by cleaved edge overgrowth technique. (a) The quantum well structure is first grown (a). By using *in situ* cleaving and overgrowth the T-shaped quantum wires are realized (b). By cleaving in another direction and growth on the top allows the fabrication of QD (Grundmann and Bimberg, 1997).

2.4 Self-Assembled Growth

The self-assembled growth, which can be realized a QD structure, is presented in more detail in this section because it is the QD fabrication technique which is used in this thesis work. The growth mode and growth conditions for this self-assembled growth are discussed in order to provide some basic understanding of this growth method.

2.4.1 Growth Modes

From the general theory of crystal growth by molecular beam epitaxy, there are three possible modes of crystal growth on the surface (Herman and Sitter, 1989). These modes are illustrated schematically in Figure 2.10. The difference between layer-by-layer or Frank-van der Merwe (Figure 2.10(a)) and island or Volmer-Weber mode (Figure 2.10(b)) can be explained by the surface/interface free energy model (Gilmer and Grabow, 1987). If we denote the free energy of the epilayer/vacuum interface by γ_e, that of the epilayer/substrate interface by γ_i, and that of the substrate/vacuum interface by γ_S, the layer-by-layer growth mode is favoured if

$$\Delta\gamma = \gamma_e + \gamma_i - \gamma_S < 0 \qquad (2.17)$$

In this case, as epilayers are formed, the free energy decreases initially before attaining a steady-state value for thicker films. Alternatively, if

$$\Delta\gamma > 0 \qquad (2.18)$$

island growth is favoured. Here, the free energy increases if epilayers are formed on the substrate, rendering a uniform layer thermodynamically unstable against a break-up into regions where the substrate is covered and those where it is uncovered.

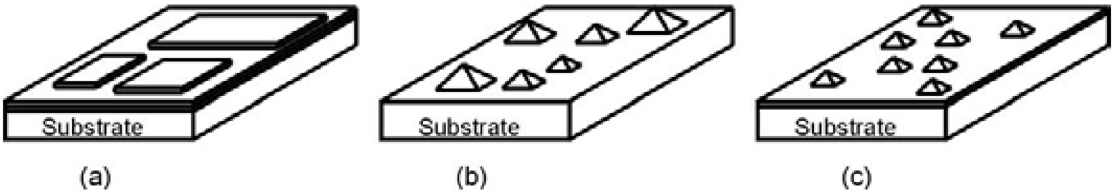

Figure 2.10 Schematic representation of the three crystal growth modes (a) Layer-by-layer or Frank-van der Merwe; (b) island or Volmer-Weber; (c) layer-plus-island or Stranski-Krastanow mode.

In case of layer-plus-island growth or Stranski-Krastanow mode (Figure 2.10 (c)), the growth proceeds in an intermediate case. After forming a few monolayers in layer-by-layer growth mode, the islands are formed on top of this "intermediate" layer, which is called the wetting layer (WL). The explanation on this growth mode is presented in the next section.

2.4.2 Self-Assembled Growth in Stranski-Krastanow Mode

In this section, we investigate the detail of Stranski-Krastanow growth mode, which provides defect-free self-assembled QDs structures. The illustration of the film growth in this growth mode is shown in Figure 2.11. First, a few monolayers of strained material grow in layer-by-layer growth mode. During the growth, elastic strain energy, $E(\mathrm{el})$ builds up due to the lattice mismatch, which is given by (Seifert et al., 1996)

$$E(\mathrm{el}) = \lambda\, \varepsilon^2 A\, t \qquad (2.19)$$

where λ is the elastic modulus, ε is the misfit, and A is surface area. The total energy for the layer-by-layer growth increases as a function of the film thickness t. Beyond the critical thickness, the layer-by-layer growth is unfavorable, and so elastic strain relaxation occurs. The nanoscale islands formed in this mode, which is still coherent, can be used to confine carrier in three dimensions. The nanostructures formed in the Stranski-Krastanow growth mode are called self-assembled QDs.

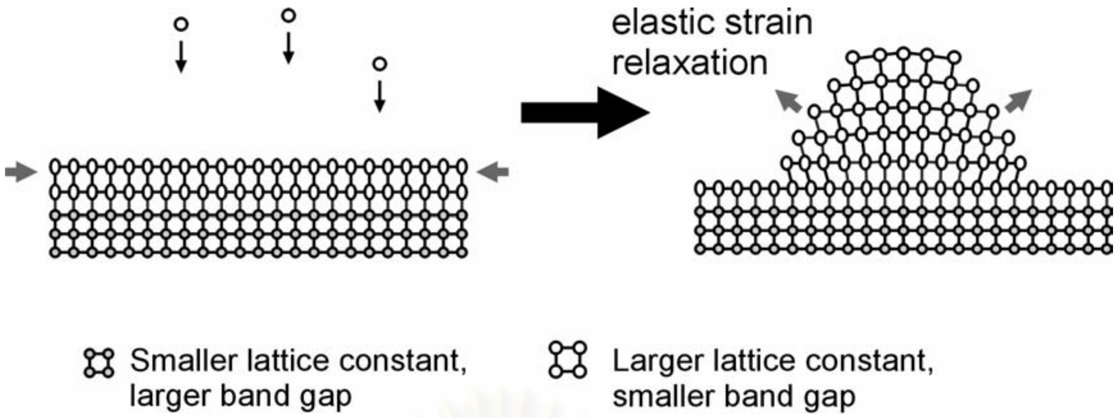

Figure 2.11 Illustration of island formation during epitaxial growth of a semiconductor material (bright) on top of another semiconductor with a smaller (by a few percent) lattice constant (dark) in Stranski-Krastanow mode. The island formation is energetically favorable if we deposit material beyond critical thickness, because the lattice can elastically relax compressive strain and thus reducing strain energy.

Although the QDs grown by this technique form into high density arrays and do not need any *ex situ* processing. There are still some disadvantages of this technique. For example, up to now we can not precisely control the locations of the QDs. Although, many groups have tried to achieve this goal (Kohmoto et al., 2002; Lee et al., 2000). The control of location is very important for using QDs in nanoelectronic applications. Moreover, the Stranski-Krastonow QDs exhibit large size fluctuations, which is undesirable for laser applications (see eq. (2.11)).

2.4.3 Material Considerations

Self-assembled growth can be carried out in several semiconductor material systems, e.g., In(Ga)As/GaAs, InP/InGaP, or SiGe/Si. The preliminary condition for the growth is that the QD material has a larger lattice constant and a smaller band gap compared with the substrate material. Figure 2.12 shows the band gap energy as a function of lattice constant for the III-As material systems. For laser applications in

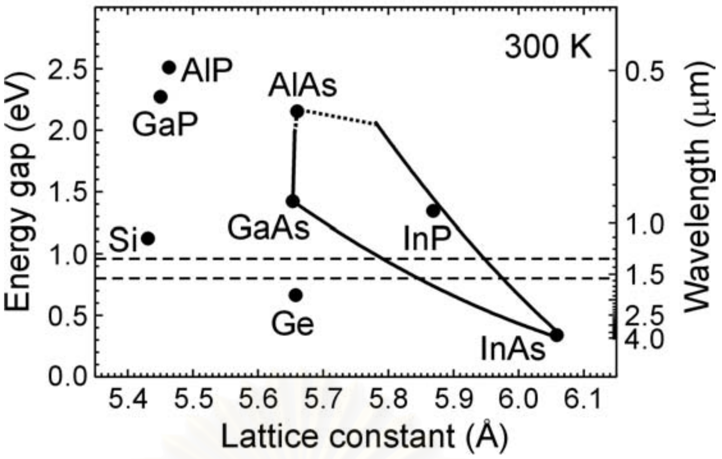

Figure 2.12 Lattice constant versus energy gap at room temperature for the III-As material system. The solid line is for direct band gap material and the dotted line is for indirect band gap material. From the figure we can see that there is a possibility to realize QD structures which emit light at the wavelength of 1.3 μm or 1.55 μm (dashed lines).

optical communication systems, technologically, GaAs is the most important substrate material. The self-assembled growth of InAs on GaAs substrate can provide QDs, which emit light at 1.3 μm or longer wavelength (Murray et al., 1999; Nakata et al., 2000; Tatebayashi et al., 2001). In this work, we will concentrate only on the InAs/GaAs material system.

2.5 Theories of Self-Assembled QD Formation

In order to improve the size homogeneity of self-assembled QD array, the theories on this self-assembled growth must be considered. From literatures there exist two theoretical concepts, which explain the QD formation and the natural size distribution. In this section, we will briefly review these two concepts, which are thermodynamically limited and kinetically controlled growths. Recently Meixner et al. (2001) used a kinetic Monte Carlo simulation to suggest that the QD formation is controlled kinetically. Thus, we will mainly use the kinetic aspects to explain our results.

2.5.1 Thermodynamically Limited Growth

Thermodynamic theory of three-dimensional coherently strained island growth was proposed by Shchukin et al. (1995) and was supported by several groups (e.g. Spencer and Tersoff, 1997; Wang et al., 2000; Medeiros-Ribeiro et al. 1998). Based on energy minimization, highly strained coherent 3D islands (QDs) equilibrate into ensembles with equilibrium size. The detail of this theory will be briefly introduced in this section.

If one considers the total energy of a single QD or island, the energy of a single island, E_{island}, can be written as a sum of three contributions, i.e.,

$$E_{\text{island}} = E_{\text{elastic}} + E_{\text{surf}} + E_{\text{edge}} \tag{2.20}$$

where E_{elastic} is the elastic strain energy, E_{surf} is the surface energy of the island, and E_{edge} is the island edge energy. Assuming that the island has a pyramidal shape with a squared base size L, the energy per unit volume of the L-dependent terms can be expressed as follows (Bimberg et al., 1999):

$$E(L) = E_0\left[-2\left(\frac{L_0}{L}\right)^2 \ln\left(\frac{e^{1/2}L}{L_0}\right) + \frac{2\alpha}{e^{1/2}}\left(\frac{L_0}{L}\right)\right] \tag{2.21}$$

where α is a control parameter which is a function of surface energy and elastic strain energy of QD structure. The α value can be positive or negative. The E_0 and L_0 are the characteristic energy and the characteristic length of the pyramid, respectively. The relationship of island energy per unit volume and base size L shown in eq. (2.21) are plotted in Figure 2.13 for different values of the control parameter α. Due to the lack of knowledge in the relationship between the QD shape and the energy contribution, we can not explicitly determine the control parameter, the characteristic energy, and the characteristic length. Nevertheless, analysis from eq. (2.21) reveals that if $\alpha \leq 1$, there exists an optimum island size L_{opt}, corresponding to the absolute minimum of the energy, min $E(L) \equiv E(L_{\text{opt}}) < 0$. On the other hand, the ripening of islands corresponds to $L \rightarrow \infty$, where the energy $E(L) \rightarrow 0$. Therefore an

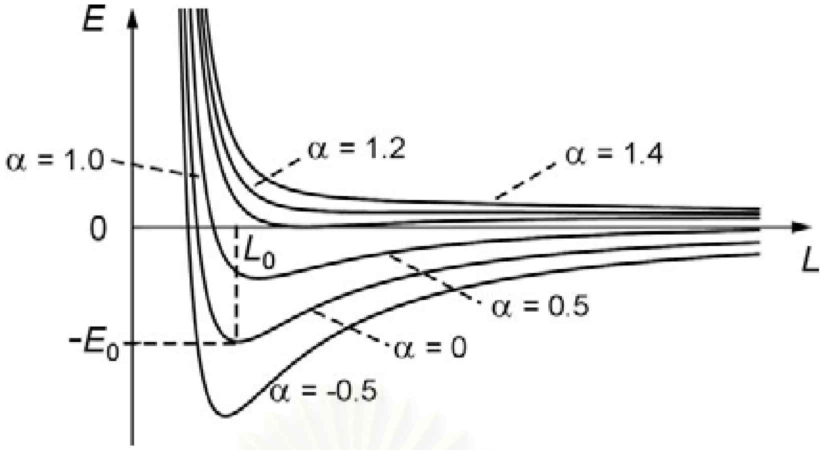

Figure 2.13 Energy of an array of 3D coherently strained islands per one atom versus island size *L*. The control parameter α depends on the contribution from the surface energy and the edge energy (Bimberg et al., 1999).

array of identical islands of the optimum size L_{opt} is a stable array, and the islands do not undergo ripening ($\alpha \leq 1$). If $1 < \alpha < 2e^{-1/2}$, there exists only a local minimum of the energy, corresponding to a metastable array where $E(L) > 0$. If $\alpha > 1.2$, the local minimum in the energy $E(L)$ disappears. For both cases where $\alpha > 1$, there exists a thermodynamic tendency towards ripening. This energy minimum then corresponds to a single huge cluster where all the deposited material is collected (Shchukin and Bimberg, 1999).

A more profound understanding of the equilibrium morphology of the system can be achieved if one takes into account the existence of the wetting layer. Due to mass conservation of the QD material (neglecting desorption and interdiffusion), which is distributed between the wetting layer and 3D islands. Neither the thickness of the wetting layer nor the total volume of all islands is separately fixed. To minimize the energy of the system, we have to take the energy stored in the wetting layer into account. Such a model was introduced by Daruka and Barabási (1997). The total energy per unit cell of this system is given by

$$E = E_{\mathrm{WL}}(Q_1) + Q_2\, E_{\mathrm{island}}(Q_2) + (Q - Q_1 - Q_2)\, E_{\mathrm{rip}} \qquad (2.22)$$

Here the energy of the wetting layer equals $E_{WL}(Q_1)$. Equation (2.22) implies that Q monolayers of material 2 are deposited, Q_1 monolayers form the wetting layer, Q_2 monolayers are assembled in 3D coherently strained islands of a given pyramidal shape and volume, and the rest of the material 2, which is equal to (Q - Q_1 - Q_2) monolayers, is assembled in the ripened islands. The energy of 3D pyramids per atom equals E_{island}, which has a little different form compared to that of the definition in eq. (2.20) (See Shchukin and Bimberg, 1999 and Daruka and Barabási, 1997 for detail discussion.). Hence the energy of the "ripened" islands is obtained if one takes the limit $L \rightarrow \infty$.

Equation (2.22) defines the total energy of the wetting layer and the 3D pyramidal islands, where the latter may exhibit *bimodal behavio*r, i.e., both small islands of size L_{opt} and large islands considerably larger than L_{opt} may be presented in the system. By minimizing the energy in eq. (2.22) with respect to Q_1 and Q_2 , one can obtain the equilibrium phase diagram of a lattice-mismatched heteroepitaxial system as a function of the lattice mismatch ε_0 and of the total amount of the deposited material Q. The calculated phase diagram is shown in Figure 2.14. A detailed explanation of each region in the diagram can be found in the original paper (Daruka and Barabási, 1997) or in several review articles (Merz et al., 1999; Barabási et al., 2000).

From the thermodynamic theories developed by Shchukin et al. (1995) and Daruka and Barabási (1997), we conclude that the QDs are formed because they are energetically more favorable than 2D growth and ripening, which introduces defects. However, the thermodynamic theories can not provide several aspects during the growth of the QDs. For example, the growth of the QDs is generally known to depend on the growth rate, which can not be explained by the equilibrium theory. Moreover, the predicted tendency of the QD size on the growth temperature from this theory contradicts to many experimental results (Meixner et al., 2001). Finally, the effects of the entropy, which is excluded in this consideration, should be considered in order to explain the QD size and the size distribution.

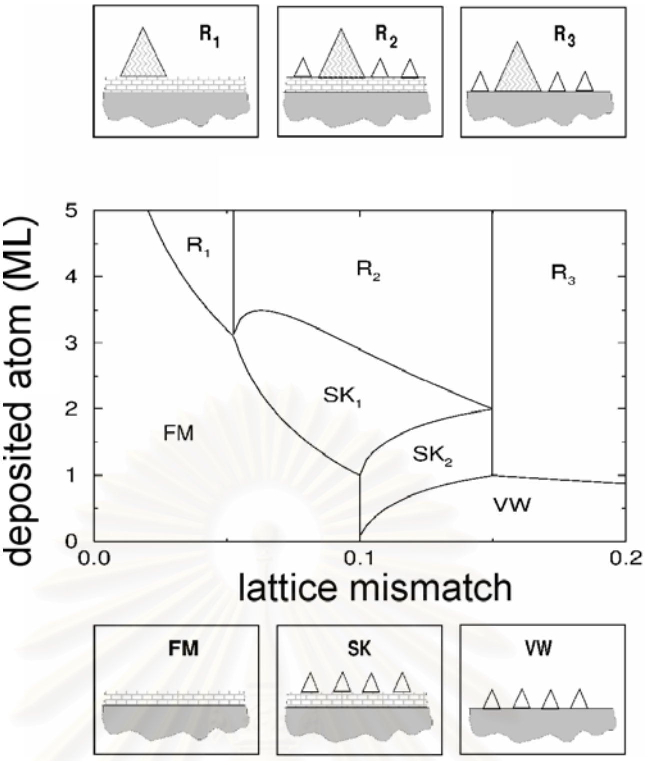

Figure 2.14 Equilibrium phase diagram of a lattice-mismatched heteroepitaxial system as a function of the total amount of deposited material *Q* and the lattice mismatch ε_0. The small panels on the top and bottom illustrate the morphology of the surface in the six growth modes. The small empty triangles indicate the presence of stable islands, while the large shaded ones refer to ripened islands (Daruka and Barabási, 1997).

2.5.2 Kinetically Controlled Growth

Another theory, which provides an effective prediction of the QD formation mechanism, is the kinetic theory of growth. This method is usually based on time-dependent calculations such as nucleation theory, kinetic Monte Carlo simulation (Schöll and Bose, 1998; Barabási, 1997). In this section, we describe the kinetically controlled growth of QDs in a qualitative way. This description follows mean-field theory developed by Dobbs et al. (1997).

A schematic diagram of atomic processes, which is described by the mean-field theory, is shown in Figure 2.15. First, the deposited atoms arrive at the surface and become adatoms. The number of adatoms increases constantly during the initial

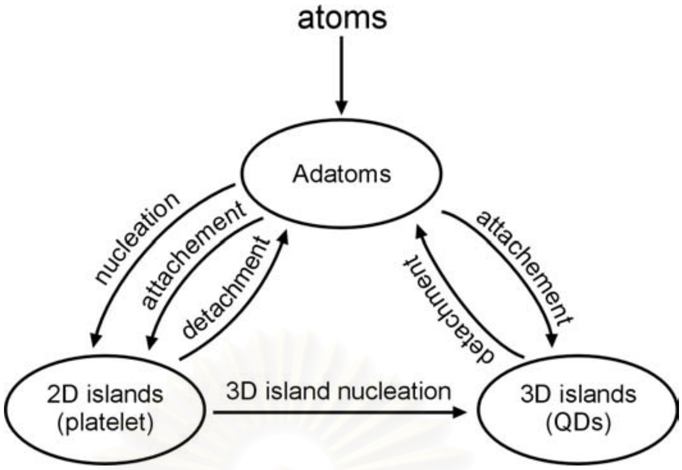

Figure 2.15 Schematic diagram of atomic processes relevant to the QD formation in the mean-field theory.

growth. The adatoms that migrate on the surface collide with one another and then nucleate into small 2D islands (platelet). Thermal fluctuations can break up these small 2D islands with sizes less than a critical value *i*, into adatoms again. During further material deposition, 2D islands become larger due to the attachment of new-coming adatoms. If the 2D island size exceeds the limiting value, the growth of these islands will change from the 2D to 3D growth mode. The adatoms can also attach to or detach from the nucleated 3D islands at the rates determined by the related energy contribution.

By solving the mean-field rate equations obtained from the atomic processes described above, the dependence of the 3D island (QD) density the on the growth parameters (temperature, growth rate) can be accurately predicted for InP QDs grown on GaP-stabilized GaAs(001) (Dobbs et al., 1997). The trend in InAs QD size evolution can be described by this theory as well (Koduvely, 2000).

Another kinetic aspect, which can describe the limited size of the QDs, is the self-limiting growth (Seifert et al., 1996; Chen and Washburn, 1996; Jesson et al., 1998). Figure 2.16 shows a schematic of the local strain energy density in and around a 3D island during the island formation (Seifert et al., 1996). The appearance in this

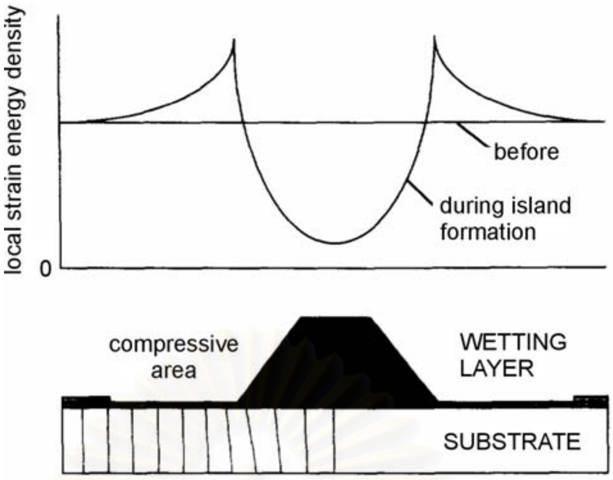

Figure 2.16 Schematic representation of the local strain energy density in and around the QD. The energy barrier for the adatoms' diffusion to the QD has a maximum at the edge of the QD (Seifert et al., 1996).

energy density due to the formation of the 3D island affects the surface chemical potential. The minimum of the potential locates at the top of the island where the material partially relaxes, while the maximum is at the island edge, where the high compressive strain exists. The compressive strain at the island edge propagates down to the substrate, increasing an inherent misfit between the substrate and the wetting layer around the island. Therefore, the high potential barrier around the island provides a zone, where the islands do not prefer to nucleate. Since the increase of the potential around the coherent islands depends on the island size, its formation has a self-limiting effect on the growth of the coherent islands. Chen and Washburn (1996) derived that due to this effect, the growth rate (increasing rate in 3D island size) decreases as the island size increases. The self-limiting process is also observed by considering the facet free energy as reported by Jesson et al. (1998).

CHAPTER 3

Experimental Details

The details of the sample fabrication by molecular beam epitaxial (MBE) growth and *in situ* etching used in this work are explained in this chapter. The calibration of growth and etching rate was done by *in situ* reflection high-electron energy diffraction (RHEED) observation, while the quantum dot (QD) samples were characterized by *ex situ* atomic force microscopy (AFM) and photoluminescence (PL) spectroscopy.

3.1 Molecular Beam Epitaxy

All samples in this work were grown in a modified RIBER 32P solid source MBE machine. The MBE system consists of three chambers, i.e., introduction chamber, transfer chamber, and growth chamber. A schematic drawing of the modified III-V MBE growth chamber is shown in Figure 3.1.

The group III and group V elements (In, Ga, Al, and As_4) are contained in PBN crucibles installed in separated effusion cells. All cells were heated by heaters and the temperatures were controlled by feedback from standard thermocouples (W-Re with 5 or 26% Re) through a computer. In case of the Ga cell, the special cell type called **hot lip** is used in order to prevent the Ga solidification at the lip. The beam flux is turned on and turned off by controlling of the tantalum shutter position in front of each cell.

The $AsBr_3$ *in situ* etching gas system was installed and connected to the growth chamber via a port at the middle of the cell flange. The tube is evacuated by a turbo-molecular pump and is heated to about 80°C to avoid the condensation of etching gas. The flow rate of the etching gas is controlled by a mass flow controller (MFC) (MKS Instrument type 250D). A detailed calibration of the etching rate will be presented in Section 3.3.

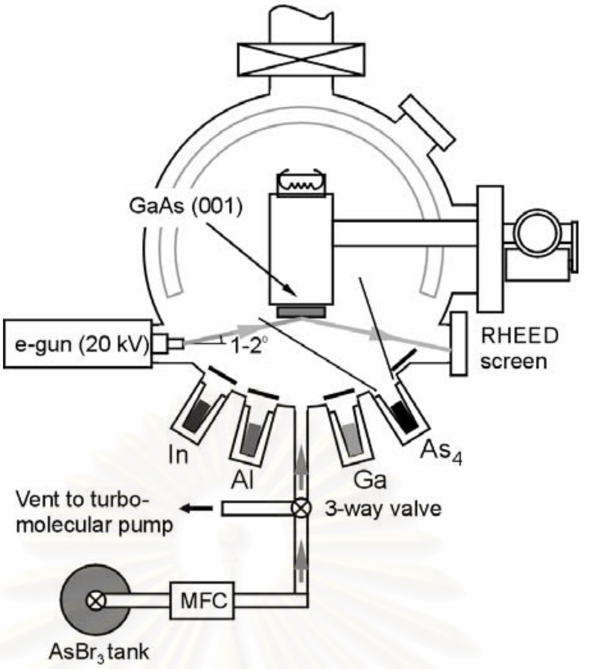

Figure 3.1 Schematic drawing of the growth chamber of the III-V MBE system modified with an $AsBr_3$ *in situ* etching gas system. The growth chamber is cooled by a closed circuit liquid N_2. It is pumped by a cryopump, an ion pump and a Ti-sublimation pump. The base pressure is less than 1×10^{-10} mbar.

In situ RHEED intensity oscillations are mainly used to deduce the absolute values of GaAs, AlAs, and InAs growth rates as a function of cell temperatures (see Section 3.3). This RHEED observation is also very important for the growth of QDs because the pattern transition from streaky (2D) to spotty (3D) pattern indicates the self-assembled QD formation in the Stranski-Krastanow mode. The equipment for RHEED experiments are a 20 kV electron gun, a fluorescent screen, a CCD camera, and a computer.

The detailed steps for sample preparation are as follows. First, an approximately $1\times1\text{-cm}^2$ piece of epi-ready semi-insulating (001) GaAs wafer is glued on an unpolished 3" Si wafer by using indium glue. The wafer was then mounted onto a molybdenum block. After transferring of the wafer into the introduction chamber, the block with the wafer is heated in the introduction chamber or in the transfer chamber to 300°C for more than 30 min in order to decontaminate the wafer from water (H_2O). Before growth, the sample is heated to desorb the oxide layer from the surface at 630°C for 10 min, under As_4 pressure of ~ 8×10^{-6} mbar. The surface structure was carefully observed by RHEED at this stage. After the oxide desorption at 630°C, the sample was cooled down and a 300-nm thick GaAs buffer layer was grown to flatten the surface. The GaAs growth rate is 0.6 monolayer/s (ML/s). The sharp and clear streaky (2×4) RHEED pattern is always observed after finishing the growth of this buffer layer. Then, the temperature calibration procedure by RHEED observation is performed to obtain the actual surface temperature. The details of this step will be presented in Section 3.2. After that, a 100-nm GaAs, a 20-nm $Al_{0.4}Ga_{0.6}As$, and a 20-nm GaAs layers were grown before ramping down the substrate temperature to 500°C. When the temperature was stable, a single layer of self-assembled InAs QDs was grown. For all QD layers, the growth temperature was fixed at 500°C. After growing the QD layer, a 100-nm GaAs, a 20-nm $Al_{0.4}Ga_{0.6}As$, and a 20-nm GaAs were grown to cap the QDs for PL observation. Finally, the same QD layer was grown again on the GaAs surface in order to investigate the QDs' structural properties by AFM. The schematic of the sample structure grown in this work is shown in Figure 3.2. Note that two 20-nm $Al_{0.4}Ga_{0.6}As$ layers were grown in order to improve the PL signal due to enhanced carrier confinement. The amount of the deposited InAs, the growth rate effects, the growth interruption after the QD formation, the capping temperature effect as well as the *in situ* etching of the QDs were studied in this work.

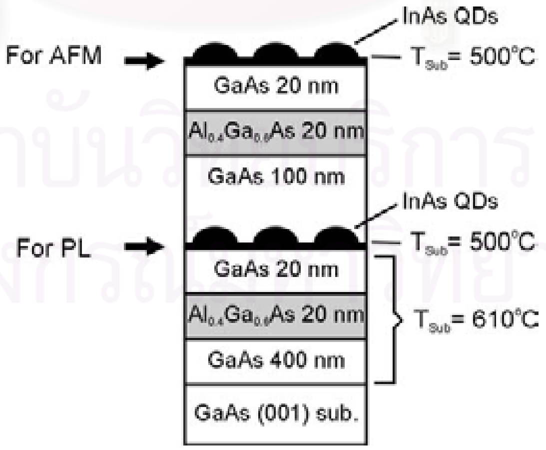

Figure 3.2 Schematic diagram of the sample structure grown in this work. The growth conditions for the InAs QD layer were given in the text.

3.2 RHEED Pattern Observation

Schematic representation of the RHEED observation system in the MBE growth chamber is shown in Figure 3.3(a). The high-energy electron beam intersects with the sample surface at a small angle ($\theta \sim$ 1-2°). It is diffracted by the surface atoms, which function as a grating, giving rise to the diffraction pattern. The pattern is observed on a fluorescent screen. Because the RHEED pattern depends on the surface atomic configuration and can be performed *in situ*, this observation is crucial for MBE growth.

The condition for imaging on the fluorescent screen is called the **Laue diffraction condition** (Kittel, 1996):

$$\boldsymbol{k}_{\text{in}} - \boldsymbol{k}_{\text{diff}} = \boldsymbol{G} \tag{3.1}$$

where $\boldsymbol{k}_{\text{in}}$ and $\boldsymbol{k}_{\text{diff}}$ are the wavevectors of the incident and diffracted electrons, respectively, and $\boldsymbol{G}$ is the reciprocal lattice vector. This condition corresponds to Bragg's law in the simple diffraction theory. The pattern position can be graphically determined by the Laue method — intersection of Ewald sphere in reciprocal lattice space (see Figure 3.3(b)). Because the electron beam is restricted to the toprmost atomic layers, diffracted electron at the flat surface are images onto the screen. Therefore, the surface layer is represented by a reciprocal lattice space rods,

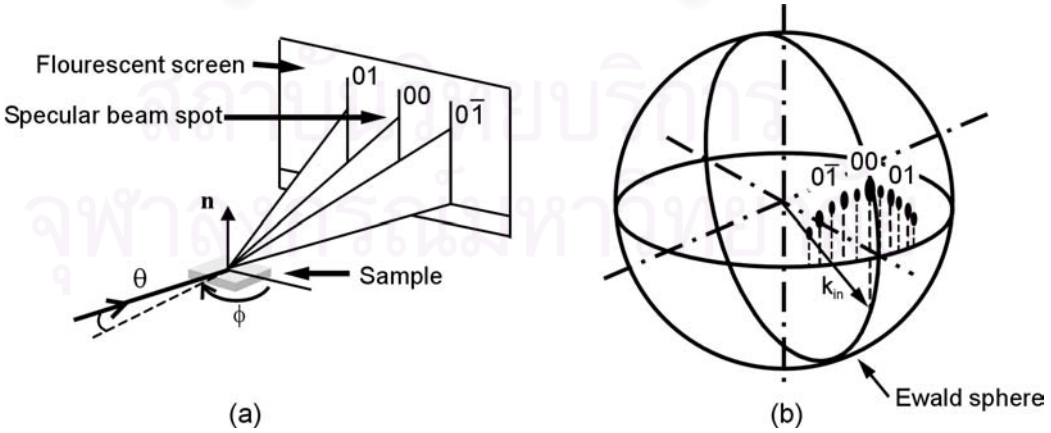

(a) (b)

Figure 3.3 (a) Schematic representation of the RHEED observation system and (b) Ewald sphere construction for a reconstructed surface in [-1 1 0] azimuth (Herman and Sitter, 1989).

which are normal to the real surface. If the surface has roughness in the order of an atomic scale, the surface layer in the reciprocal space will be represented by a three-dimensional point array. Therefore, we can simply interpret that the RHEED pattern as the reciprocal lattice representation of the sample surface, which reflects the surface morphology on the atomic scale. In general, the RHEED pattern provides information about a surface (Vvedensky, 2001) such as the crystallographic symmetry (from the symmetry of the diffraction pattern), the extent of long-range order (from the sharpness of the pattern), and whether growth proceeds in a 2D or a 3D mode. In this work, we use this RHEED observation to calibrate the substrate surface temperature and to monitor the growth mode (surface structure) during the growth of QD structure.

The transition of the reconstruction pattern as a function of substrate temperature is suitable to calibrate the absolute temperature of the substrate surface. In the specific case of the (001) GaAs surface, we can use the transition point from *c* (4×4) to (2×4) as a reference point. In this work, this transition temperature is defined as 500°C (Farrell and Palmstrøm, 1990), which is the self-assembled InAs QD growth temperature. The details of the atomic configuration and the observed RHEED patterns of both the *c*(4×4) and the (2×4) reconstruction are shown in Figure 3.4. Note that the (2×4) pattern corresponds to several atomic configurations (Esser et al., 2001; LaBella et al., 1999). Recent scanning tunneling microscopy (STM) results by LaBella et al. suggest that the most probable model is the β2(2×4) reconstruction.

3.3 RHEED Intensity Oscillation

RHEED intensity oscillations can be used to extract the growth rate. The schematic representation of the interpretation of RHEED intensity oscillation is shown in Figure 3.5(a). The RHEED intensity signal at every point on the pattern depends on the roughness of the surface. Under the normal growth condition, the RHEED intensity, i.e., surface roughness, changes according to the fraction of surface coverage where the period of the oscillation signal corresponds to

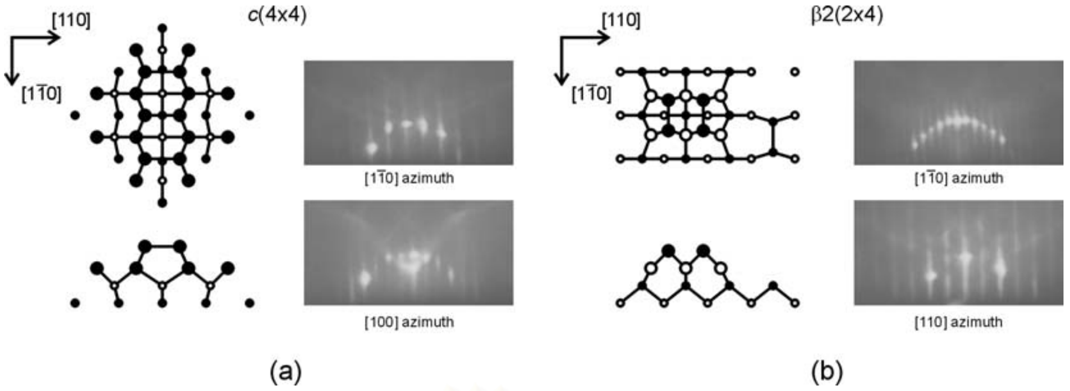

Figure 3.4 (a) Schematic representation of top view, side view of relaxed structure (Esser et al., 2001) and *c*(4×4) RHEED pattern of GaAs surface at 460°C in [1-10] and [100] azimuths; and (b) Schematic representation of top view, side view of relaxed structure (LaBella et al., 1999) and *β2*(2×4) RHEED pattern of GaAs surface at 580°C in [1-10] and [110] azimuths. Filled and empty circles represent As and Ga, respectively. Larger circles represent atoms closer to the surface.

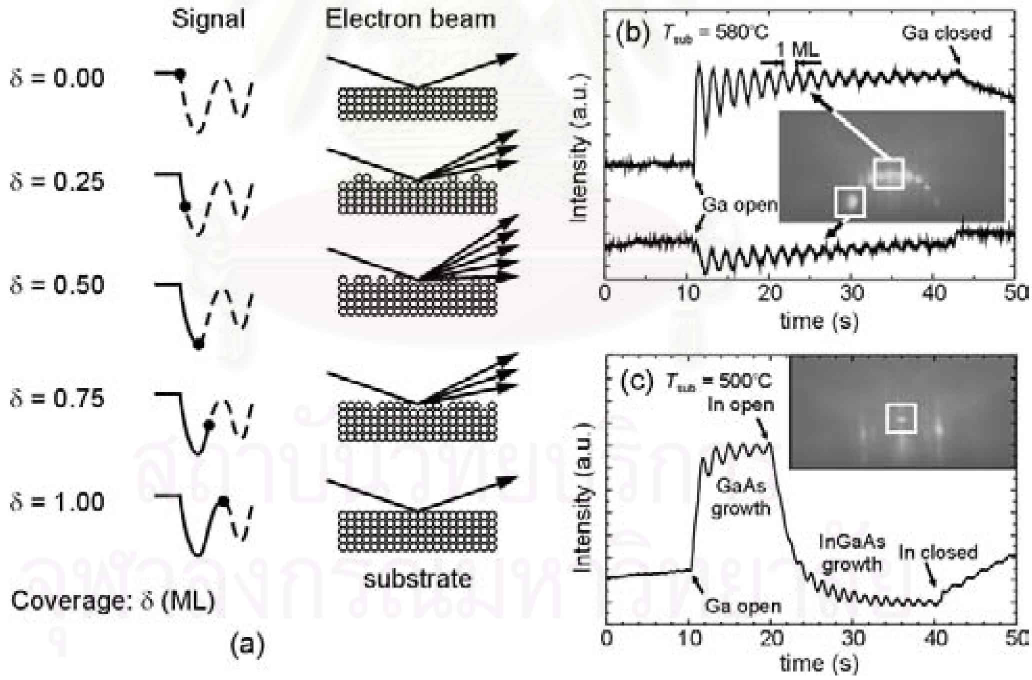

Figure 3.5 (a) Schematic representation of the interpretation of RHEED intensity oscillations. (b) and (c) are experimental results obtained during the growth of GaAs and InGaAs. The intensity signals were detected in the pattern area marked by white boxes shown in the insets.

the growth of 1 monolayer (ML). By this fact, the growth rate of GaAs and AlAs can be calibrated. The typical experimental data are shown in Figure 3.5(b). In case of the InAs, we use a different technique to calibrate the growth rate. In order to avoid the 3D growth, which forms self-assembled QDs, one has to grow thin lattice-mismatched InGaAs/GaAs. The InAs growth rate r_{InAs} can be determined by

$$r_{\mathrm{InAs}} = r_{\mathrm{InGaAs}} - r_{\mathrm{GaAs}} \tag{3.2}$$

where r_{GaAs} and r_{InGaAs} are the growth rates of GaAs and InGaAs, respectively. After depositing the InGaAs layer for the growth rate calibration, this layer must be buried by the GaAs buffer layer before growing the desired structure. A typical example of this calibration method is shown in Figure 3.5(c). However, the InAs calibration method presented here is not useful for the growth at very low growth rate due to the measurement error. Therefore, we take the QD formation time itself as the InAs growth rate calibration. In this work, we define the RHEED pattern transition during the growth of InAs, which corresponds to the growth mode changeover from streaky (2D) to spotty (3D) pattern, as 1.7 ML InAs deposition (Shchukin and Bimberg, 1999).

The growth rates of GaAs and AlAs as a function of cell temperature, calculated from the RHEED intensity oscillation experiment, are shown in Figure 3.6 (a). The growth rate of InAs calculated from the RHEED pattern transition from 2D to 3D is shown in Figure 3.6(b). The detailed experiment on the RHEED observation of InAs QD growth will be given in Section 4.1. Note that all experiments are calibrated under constant As_4 flux of about 8×10^{-6} mbar. The relationship between the growth rate (in log scale) and the inverse temperature was linearized in order to interpolate and extrapolate to the desired values.

In case of the etching by $AsBr_3$, the etching mechanism can be described as a reverse growth process in a suitable temperature range (Kaneko et al., 1995; Ritz et al., 1997; Schuler et al., 2000), i.e., the layer-by-layer etching. We use the RHEED intensity oscillation to calibrate the etching rate. A typical RHEED intensity signal during the etching rate calibration at substrate temperature of 500°C is shown in Figure 3.7(a). The flow rate of etching gas is 0.080 standard cubic centimeter (sccm),

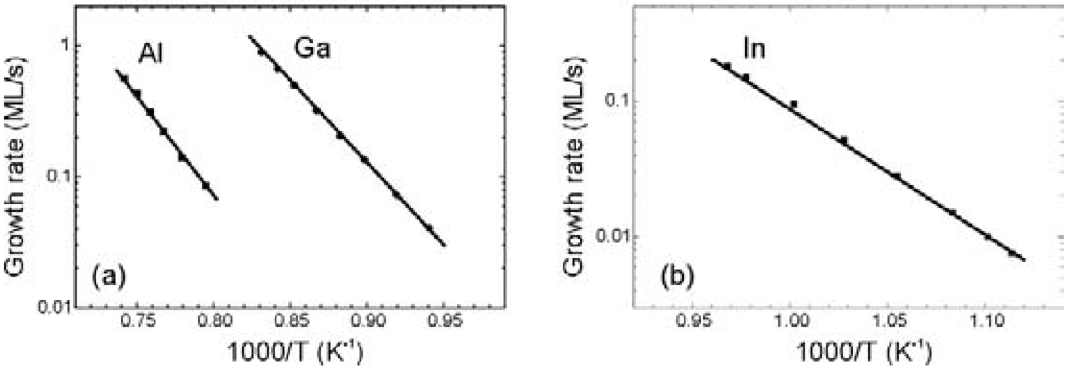

Figure 3.6 Plots of growth rates of GaAs, AlAs (a) and InAs (b) as a function of cell temperatures. The GaAs and AlAs growth rates were calibrated by RHEED intensity oscillation while the InAs growth rate was obtained from RHEED pattern transition during the growth of self-assembled QDs. All RHEED data were obtained from a 0.5×0.5 cm^2 GaAs substrate glued in the middle of a molybdenum block under As-rich condition.

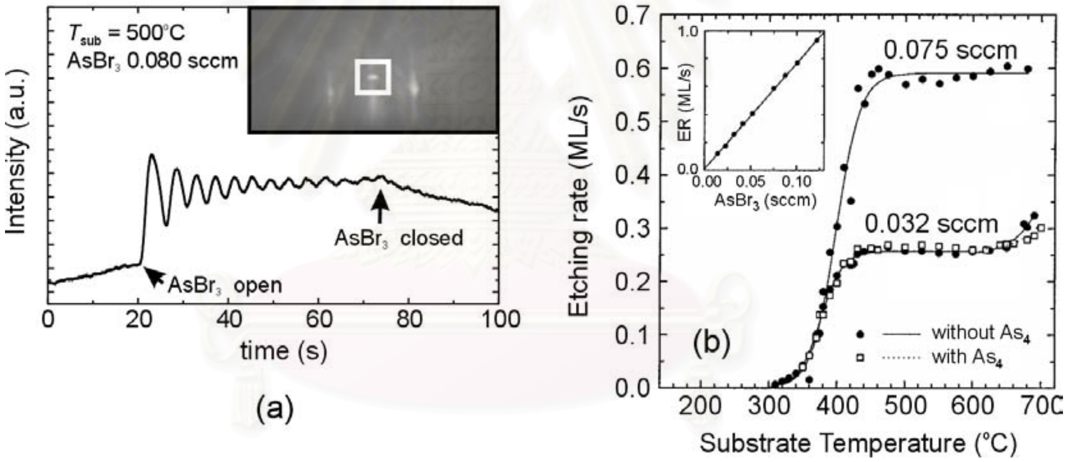

Figure 3.7 (a) RHEED oscillation result obtained during the etching of GaAs by $AsBr_3$ at 500°C. The intensity signal is obtained from the white box shown in the inset. (b) The etching rate obtained from RHEED intensity oscillation versus substrate temperature for two different $AsBr_3$ flow rates. For 0.032 sccm $AsBr_3$ flow rate, the etching rates with and without a concomitant As flux are shown. In the lower temperature region from 300 to 420°C, the etching is *reaction-rate-limited*; in the upper temperature region above 450°C it is *supply-rate-limited*. The etching rate in the supply-rate-limited regime, as a function of $AsBr_3$ flow rates, is shown in the inset (Ritz et al., 1997).

which is equivalent to an etching rate of 0.23 ML/s. From a previous study (see Figure 3.7(b)), we know that for the substrate temperature beyond about 500°C the etching rate does not depend on the As_4 flux nor substrate temperature (supply-rate-limited regime). Moreover, the etching rate is linearly dependent on the flow rate in the supply-rate-limited regime (see inset of Figure 3.7(b)); and thus, the etching rate can simply be calibrated and extrapolated.

3.4 Atomic Force Microscopy

All QD layers, which were grown on the surface, were measured by AFM. The AFM is performed using a DIGITAL INSTRUMENT (DI) Nanoscope IIIa. The AFM is operated in the tapping mode. The scan rate is ~ 1.2 Hz and the scan size is usually $2\times2\ \mu m^2$. The number of data points per scan line is 512, and so the lateral resolution of all AFM is ~ 4 nm. Due to the tip convolution (Keller and Franke, 1993; Gong et al., 1998), the exact shape and lateral size of the QD structure may not be correctly determined by this measurement. Nevertheless, the vertical resolution of this measurement is usually in subnanometer range. Therefore, in this work we only use the height distribution of the QD arrays obtained from analysis of the AFM images to determine the size homogeneity of the QDs. A set of computer programs to extract and analyze raw AFM data of QDs was written in MATLAB 5.0 Script language, and is described and shown in Appendix A.

3.5 Photoluminescence Spectroscopy

The main tool for sample characterization in this work is the photoluminescence (PL) spectroscopy. A schematic of the PL experimental setup is shown in Figure 3.8. The samples, which are buried InAs QDs in GaAs, were excited by the 488-nm line of an Ar^+ laser (SPECTRA PHYSICS SERIES 2000). The integrated laser power is 5 mW for measuring PL spectra of QD-related peaks, and 50-500 mW for measuring wetting layer and GaAs substrate peaks. The laser beam

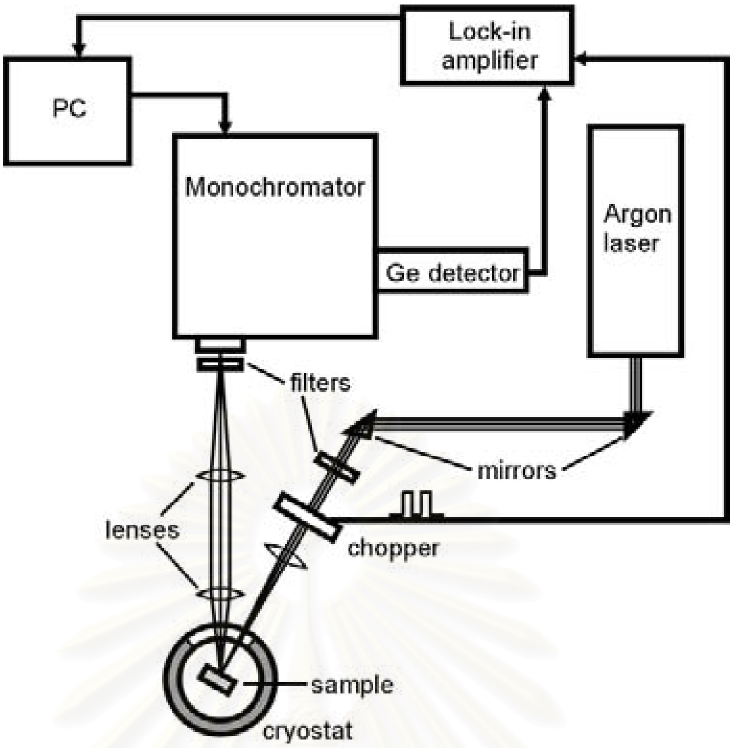

Figure 3.8 Schematic of the PL experimental setup.

was chopped and focused to the sample by a 33-cm focal length lens. An 8-cm focal length and a 40-cm focal length lens are used to collect the PL signal. The light signal is resolved by a 1-m monochromator (JOBIN YVON THR1000). Typically, the entrance and exit slit widths are 0.5 mm. A high-pass filter (RG668) is used to filter the visible-light noise and the reflected laser beam signal. The resolved light signal is detected by a liquid-N_2-cooled Ge detector (NORTHCOAST EO-817L). A chopper and the lock-in amplifier (EG&G 5207) are used to enhance the signal by the standard lock-in technique.

In this work, the interpretation of PL data can simply be described as shown in Figure 3.9 and Figure 3.10. For a case of QDs with different size in Figure 3.9, the ground state PL peak energy contains information about the size of the QD. The increase in QD size results in a lower number of quantized energy levels of both holes and electrons, which causes a lower PL peak energy position. Therefore, this PL peak position can be used to relatively compare the size of QD structure.

For the shape of PL spectrum from QD array (Figure 3.10), there exists broadening of the spectrum. This broadening, which is measured in terms of a full width at half maximum (FWHM) or PL linewidth, is related to the QD size

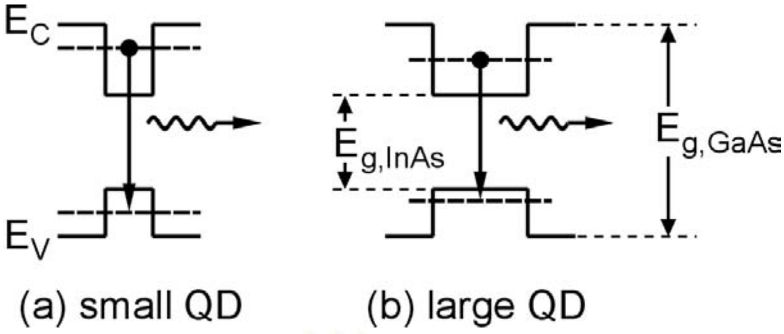

Figure 3.9 Simple interpretation of the PL data obtained from a QD structure. In case of small QD (a): the PL peak energy position is higher compared with large QD (b).

distribution. From experiments on single QD spectroscopy, we known that if the array contain a few number of QDs, the PL linewidth will usually less than 100 μeV (Zrenner, 2000), which corresponds to the delta-function-like density of states (see Section 2.1). However, in case of self-assembled QDs, there are large numbers of excited QDs, which have different size. This difference in QD sizes results in rather broad PL spectrum (~ 10-100 meV). The PL spectroscopy is therefore very important as it can be used to determine the homogeneity of the QD. In this work, we mainly use the PL linewidth to measure the homogeneity of self-assembled QD arrays.

Another interpretation of the PL results come from the fact that the loss of coherence and the onset of misfit dislocations in the epitaxial film create a high concentration of centers of nonradiative recombination and significantly reduce the integrated intensity of the PL spectrum. Therefore, we can roughly estimate and compare the defect density in the grown structure by comparing the PL intensity.

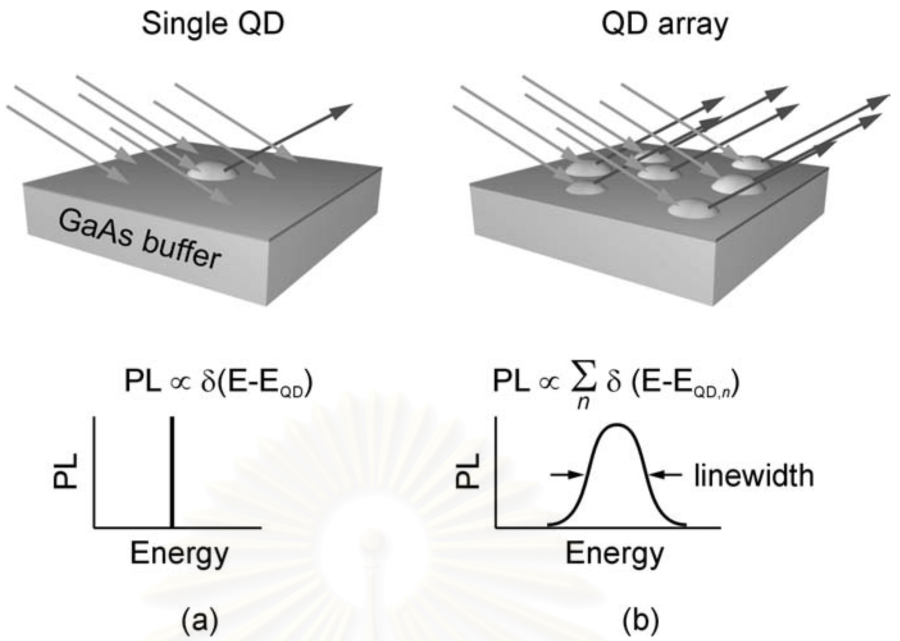

Figure 3.10 Simple interpretation of the PL spectrum obtained from the QD structure. In (a) the PL spectrum is very narrow due to the delta-function like density of states; and in (b) the average dot size corresponds to the PL peak energy position and the PL linewidth corresponds to the size distribution of the array.

CHAPTER 4

InAs/GaAs Self-Assembled Quantum Dots

The experimental results on the conventional growth of InAs/GaAs self-assembled QDs are shown in this chapter. By using RHEED observation, we can *in situ* monitor the QD formation and by using atomic force microscopy (AFM) and photoluminescence (PL), the effects of amount of InAs deposition and growth rates on the QD array can be investigated. And finally, the effects of capping on QD structure are studied.

4.1 QD Formation: *In Situ* RHEED Observation

Snapshots of RHEED patterns and intensities during the growth and the overgrowth of InAs QD layer on GaAs are shown in Figure 4.1(a) and (b), respectively. In this experiment, the RHEED pattern was observed along the [1-10] azimuth during the deposition of InAs at substrate temperature of 500°C with a growth rate equaled to 0.012 ML/s. Before opening the indium shutter, the RHEED shows a clear *c*(4×4) surface reconstruction. During the growth of InAs layer, the intensity signal gradually decreases (The signal was measured in a white box.), and the reconstruction pattern was hardly defined. With about 1.3 ML InAs deposition, the RHEED intensity starts to increase. This observation implies that the 3D InAs islands (QDs) start to nucleate on the 2D InAs surface in Stranski-Krastanow growth mode. For further InAs deposition, the RHEED pattern becomes spotty, and the intensity rapidly increases and finally saturates at about 1.7 – 1.8 ML InAs deposition. The deposition was stopped when the InAs thickness reaches 1.8 ML. The bright and spotty pattern of 1.8 ML InAs is shown in Figure 4.1(a). From this RHEED pattern, the chevron is not observed unlike in the case reported by Lee et al. (1998) and Joyce et al. (2001). This circumstance might be due to the fact that the different growth conditions from those experiments, which provided different QD shapes and sizes.

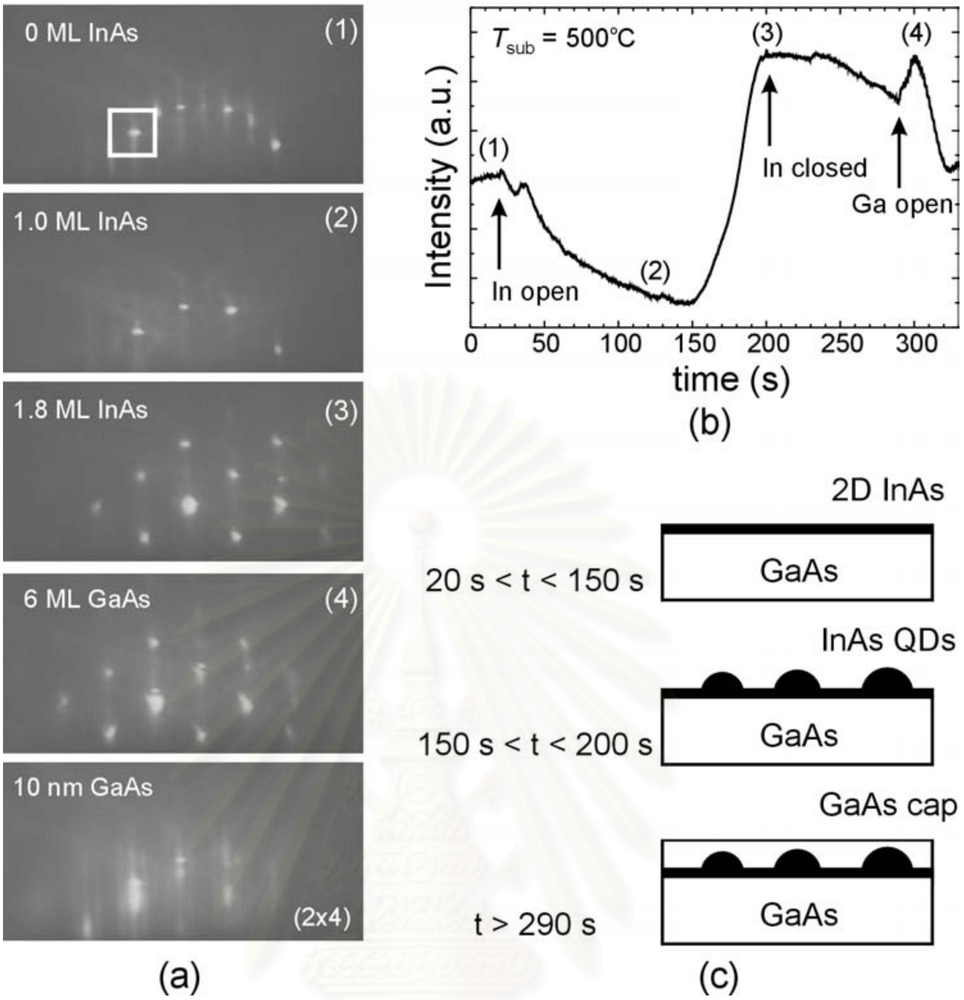

Figure 4.1 (a) RHEED patterns before (1), during growth (2) – (3) and capping (4) – (5) of InAs/GaAs self-assembled QDs in [1-10] azimuth. (b) Variation of the integrated RHEED intensity measured in the white box in Figure (a). (c) Schematic of the growth processes, i.e., layer-by-layer growth, island growth, and capping.

The shapes of the QDs also change during capping (Eberl et al., 2001; Joyce et al., 2001b), therefore the shape of the free standing QDs, which can be interpreted by the chevron shape and angle, may not be so interesting in respect to electronic properties.

The experimental results shown in Figure 4.1, after finishing InAs deposition, a 90-second growth interruption is inserted (from In-closed to Ga-open). During the growth interruption, the RHEED pattern as well as the intensity remains the same as in the initial state. After the capping of InAs with 6 ML GaAs, the RHEED pattern gradually changes back to streaky pattern as shown in Figure 4.1(a). For further capping with GaAs up to 10-15 nm, the RHEED pattern becomes completely streaky. This corresponding to layer-by-layer growth in conventional MBE growth process (Frank-van der Merwe mode).

The growth processes, which we investigate in this chapter, can be divided into three steps as shown in Figure 4.1(c), namely, the growth of InAs before the 3D transition, the growth during the 3D transition (QD formation), and the capping of these QDs. However, current researches are interested in the QD formation mechanism and the capping process. The growth of 2D InAs has been studied by several groups (Bimberg et al., 1999 and references therein).

We note that the effects of material desorption is also important in the growth of InAs layer. For the InAs QDs grown at very low growth rate of ~ 0.01 ML/s, this indium desorption limits the MBE growth temperature range. The dot formation time at different growth temperature, which is related to the desorption rate, is plotted in Figure 4.2. This dot time was measured by recording the time interval between the In-shutter opening and appearance of spotty pattern. The growth rate of ~ 0.011 ML/s, calibrated at low temperature (450°C), corresponds to the growth rate of about 0.009 ML/s at 500°C in this experiment. Furthermore, these low growth rate QD

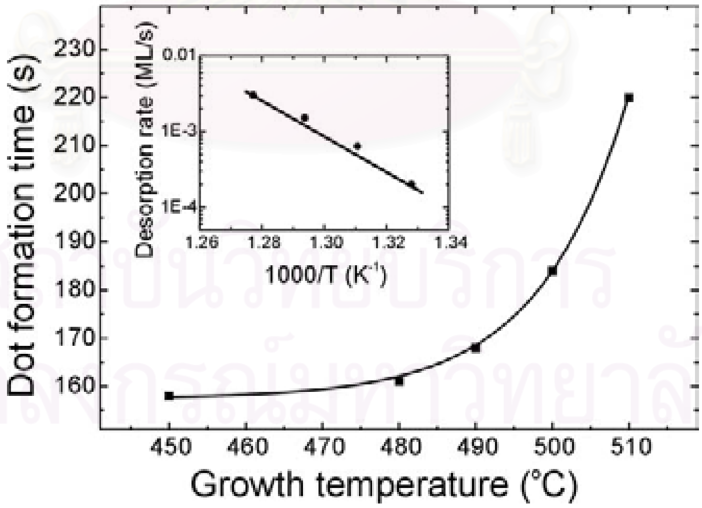

Figure 4.2 Dependence of QD formation time on the growth temperature. At high growth temperature the QDs are hardly formed due to thermal desorption of InAs. The desorption rate is calculated and shown in the inset.

cannot be grown at a substrate temperature higher than 520ºC due to thermal desorption. In addition, we cannot simply reproduce the QDs grown at the substrate temperature higher than 510°C because the changes in desorption rate is high at that temperature range ($T > 510$°C). The desorption rate of InAs, calculated from the dot formation time, is shown in the inset of Figure 4.2. The linear tendency in the Arrhenius plot implies that this desorption process is thermally activated. The fitting activation energy value in this process is ~ 4.2 eV. The calibration of this desorption rate is used as a reference data for the growth interruption and regrowth experiments (Sections 5.1 and 5.2).

4.2 QD Formation: Experiment

The origin of QD formation has been intensively studied during the last decade (Bottomley, 1998; Priester and Lannoo, 1995). There are several proposed ideas based on both theories and experimental data. In this work, the QD formation is also studied and explained in a qualitatively manner. First, the amount of deposited InAs is varied. Figure 4.3 shows AFM images of the surfaces deposited with different amounts of InAs deposition. The insets are high-contrast images (2 nm height scale). For InAs depositions less than 1.0 ML, the surfaces are atomically flat (Figure 4.3(a) and (b)). We observe terraces with 1-ML height that elongate in [1-10] direction. The elongation originates from an anisotropic diffusion coefficient of both gallium atoms and indium atoms on GaAs surface. These surfaces look similar to the typical GaAs surfaces grown at this temperature (Franke et al., 1998). For depositions larger than 1.0 ML InAs, small 2D islands with a few ML height, so-called platelets (Priester and Lannoo, 1995), are formed. These 2D islands are more clearly observed

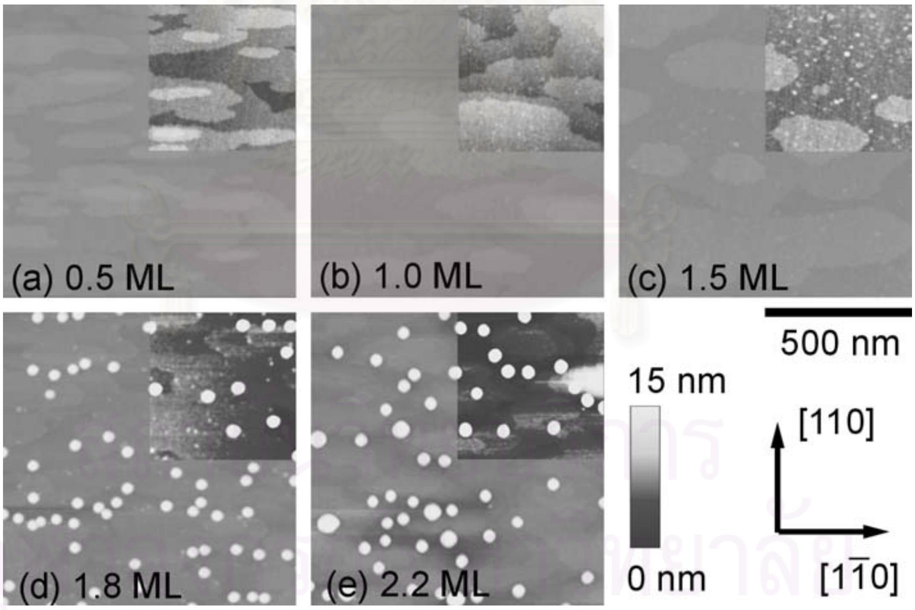

Figure 4.3 1×1 μm^2 AFM images of thin InAs on a GaAs surface. The InAs thicknesses are (a) 0.5 ML, (b) 1.0 ML, (c) 1.5 ML, (d) 1.8 ML, and (e) 2.2 ML. Each image has the same height scale of 15 nm. The inset shows height contrast images (2-nm height scale) in order to observe the 2D islands.

in high contrast height scale (cf. inset of Figure 4.3(c)). For further deposition of InAs to the thickness of about 1.7 – 1.8 ML leads to a transformation of the 2D islands into 3D islands or self-assembled QDs. However, the density of these small 2D islands is different from density of QDs. This might depend on the growth conditions (Amount of InAs deposition, growth rate, growth temperature). By using a low growth rate of about 0.01 ML/s at high substrate temperature (500°C), the created QDs have an average height (diameter) of 10.7 nm (37 nm) with a low density of about $3\text{-}6\times10^{9}$ cm^{-2}.

For this large, low-density QDs grown at low growth rate further deposition of InAs after QD formation increases the size of *some* QDs and the 2D islands disappear. The disappearance of 2D islands originates from the small stability of the structure compared with that of the QDs. Also, since some QDs are larger during the deposition for more than 1.8 ML, the size homogeneity decreases and the Ostwald ripening takes place. This Ostwald ripening causes the QDs to increase in size, so that the QDs act as a source of dislocations during the capping procedure due to excessively high tensile strain (Chen and Washburn, 1996; Eberl et al., 2001). In this work we concentrate on QDs of about 1.8 ML InAs deposition. However, the 2.2 ML InAs QDs was also studied for the comparison. The QDs shown in Figure 4.3(d) and (e) are used as a reference.

Thin InAs epitaxial layers shown in Figure 4.3, which were capped with GaAs were measured the PL. The room-temperature PL spectra of the structures are shown in Figure 4.4. From this measurement we can clearly resolve three peaks, which originate from three different structures. The peak energy at 1.424 eV corresponds to the energy gap of bulk GaAs at room temperature. The wetting layer (WL) peak is assigned to the 2D InAs layers. This peak gradually redshifts from 1.4 eV to 1.34 eV, and the intensity increases with increasing thickness. After QD formation at 1.8 ML, the peak from the QDs is observed at about 1.05 eV (1180 nm). This peak has very high intensity compared to the WL and GaAs peaks, which is the QW structure and that of the bulk material, respectively. A gradual redshift of the peak energy corresponds to the increase in the QD size, while a decrease in peak intensity might originate from dislocation defects. These PL results agree well with the observed QD structures measured by AFM.

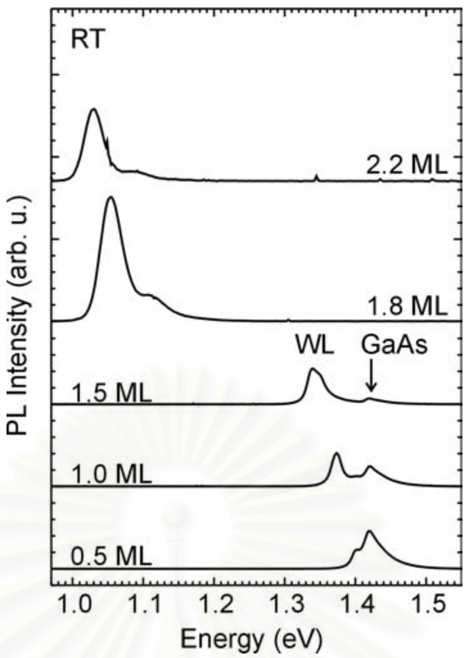

Figure 4.4 Room-temperature PL spectra of thin InAs (layers) shown in Figure 4.3 and capped with GaAs. Note that the PL measurement is performed at different power excitations. For less than 1.8 ML InAs deposition (before QD formation), the excitation is 500 mW. For more than 1.8 ML InAs deposition (after QD formation), the excitation is decreased to 5 mW.

The size distribution (homogeneity) of the self-assembled QDs in Figure 4.3 (d) or (e) can be fitted with the Gaussian distributions. As mentioned in Chapter 3, the average size of the QDs determines the peak energy level in the PL measurements (Figure 3.9 and 3.10). Moreover, the PL linewidth relates to the size distribution of QD array. The shape of the ground state PL peak spectrum from QD ensemble can also be fitted with the Gaussian distribution, and therefore we can use PL to deduce the structural properties of the QD arrays. The PL linewidth or QD size homogeneity is discussed Section 5.1.

The role of growth rate is also studied in this work. Figure 4.5 shows the AFM and corresponding height histogram extracted from the AFM figure by the algorithm described in Appendix A. We can clearly see from the figures that the dot density (ρ) increases when we increase the growth rate. From the height histogram,

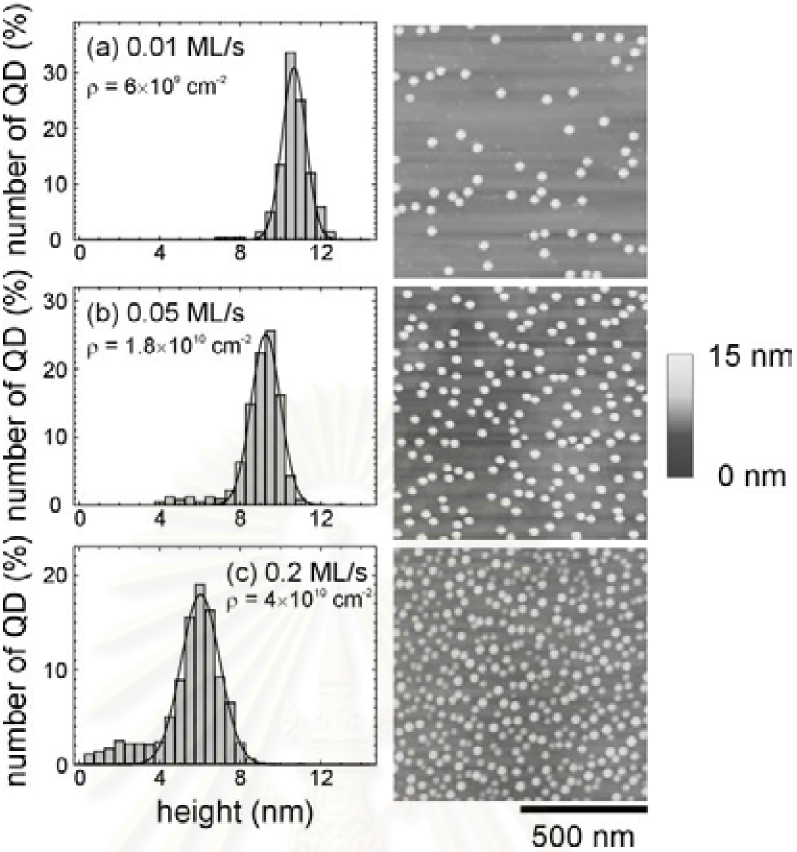

Figure 4.5 1×1 μm^2 AFM images and the corresponding height histogram of 1.8 ML InAs QD grown at different indium growth rates of (a) 0.01 ML/s, (b) 0.05 ML/s, and (c) 0.2 ML/s. The dot density increases as the growth rate increases.

we also find that the sizes (heights) of the QDs are reduced from the average height of 10.7 nm to 4.5 nm. The growth rate effect on the size of the QDs can be explained by the different time scale for the island formation (Seifert et al., 1996; Nakata et al., 1999). For a higher deposition rate, island formation is put into a narrow time interval. A narrow time interval results in less material diffusion as well as smaller diffusion length, thus the 2D-to-3D nucleation process occurs at a relatively higher rate. The effect of growth rate on the size of the QDs is relevant after the 3D nucleation. Due to material conservation, the low-density QDs (from deposition at low growth rates) must have larger sizes compared with those of the high-density QDs. However, the law of mass conservation can not be fully used to describe the total material in the QDs because there is also large Ga interdiffusion during the QD formation. The scanning tunneling microscopic (STM) results by Joyce et al. (2000) suggested that at higher deposition rates the interdiffusion effects change the indium fraction in the QD from InAs to InGaAs. The fraction of Ga in the QDs strongly depends on the growth conditions.

Figure 4.6 shows the room-temperature PL spectra of 1.8 ML InAs QDs grown at different growth rates. The PL results correspond well to the AFM results, i.e., the PL peak energy blueshifts from 1.05 eV to 1.15 eV due to the decrease in QD size when we increase the growth rate. The increment of the PL linewidth at higher deposition rates, which correspond to decrease in QD size homogeneity, may be explained as following. At a low growth rate, the adatoms can diffuse and reach more favorable sites before capping the QDs with GaAs. Therefore, the QD arrays grown at a low growth rate might approach a more energetically stable state compared with the QDs grown at high growth rate. The more stable QD ensemble results in a more homogeneous QD arrays as explained in terms of the PL linewidth. The low-growth-rate QDs also experience smaller change in size during a growth interruption (All results shown here have no growth interruption after QD formation). The experimental results on the growth interruption will be shown in Section 5.1.

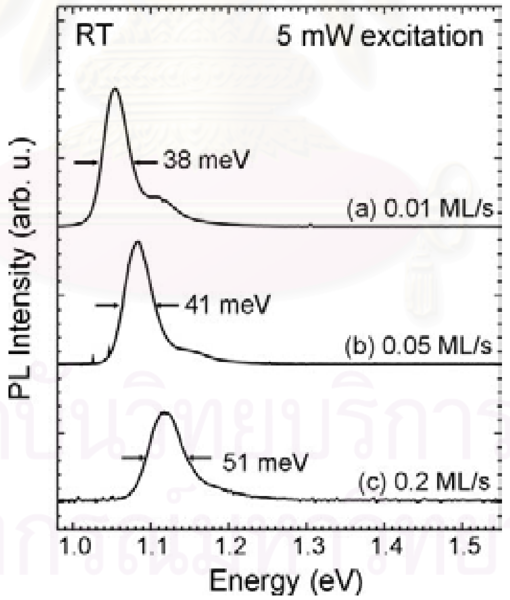

Figure 4.6 Room temperature PL spectra of 1.8 ML InAs QD grown at different indium growth rates of (a) 0.01 ML/s, (b) 0.05 ML/s, and (c) 0.2 ML/s. The PL linewidth agrees well with the QD height distribution (see Figure 4.5).

4.3 Conventional Capping Process

The capping process of large InAs QDs grown at low growth rates is studied in this section. Figure 4.7 shows the 1×1 μm^2 AFM images and the corresponding linescans of thin GaAs capped QD surface. Comparing the reference free-standing QDs shown in Figure 4.7(a) to the QDs with a 2-nm GaAs cap layer shown in Figure 4.7(b), we found that the QDs have drastically collapsed during the initial stage of the capping process. The QDs' height decreases from about 10 nm to less than 4 nm. Further capping of these QDs results in a mound-shaped structure of GaAs with a density similar to the initial QD layers. This capped dot surface becomes atomically flat at about 30 nm of GaAs cap thickness (not shown). The collapse of the QDs and the flattening phenomena can be explained by the chemical potential considerations (Srolovitz, 1989; Songmuang et al., 2003), which includes the effects of strain. The discussion of the growth of QDs will be presented and compared with the case of low-temperature capping in the Section 5.4.

Because there are both indium segregation and intermixing during capping, the AFM results shown in Figure 4.7 cannot be used to determine the QD shape and

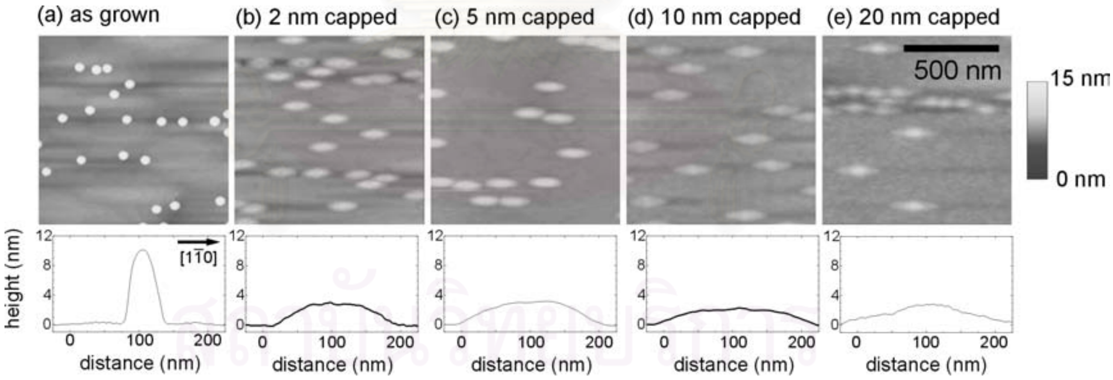

Figure 4.7 1×1 μm^2 AFM images of the 1.8 ML InAs QDs with thin GaAs capping layer thicknesses: (a) as grown, (b) 2-nm capped, (c) 5-nm capped, (d) 10-nm capped, (e) 20-nm capped. The bottom row shows the cross-sectional view of a nanostructure. The shape of the QDs drastically changes during the capping process.

size during cap. The atoms on the thin capped dot surface might be GaAs or InAs. The effects of indium segregation have been extensively studied in case of the growth of InGaAs/GaAs quantum wells (Yu et al., 1995; Disseix et al., 1997). For QDs, the effects are more complicated because of the 3D geometry. One tool, which can be used to interpret the capping effects is the low temperature photoluminescence (PL). Figure 4.8 shows the PL spectra, measured at 10 K, of QDs grown and capped with a thin GaAs capping layers. The explanation of the PL peak spectra is as follows. The small peak at 1.51 eV corresponds to the energy gap of the bulk GaAs. The peak at 1.49 eV is the exciton peak of GaAs bulk. The wetting layer (WL) peaks at 1.43 – 1.45 eV at 10 K can be clearly observed for the 20-nm cap. The ground state QD peak is 1.02 eV and 1.10 eV for 10 nm and 20 nm GaAs capped, respectively. The blueshift of the QD peak energy is due to the increase of strain when increasing the cap thickness (Pistol et al., 1995). Note that the growth is performed at 500°C, and so the intermixing effect is rather strong. This PL result will be discussed and compared with those of the low-temperature capped QDs in the next chapter.

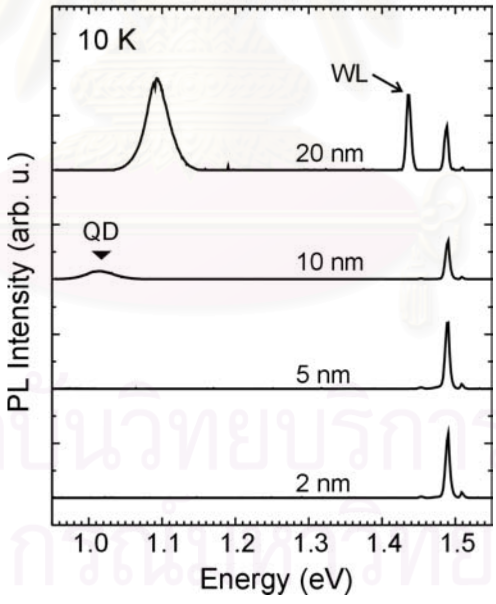

Figure 4.8 Low-temperature PL spectra of InAs QDs near the surface for different capping layer thicknesses.

From our AFM and PL results, the capping process of large QDs is schematically shown in Figure 4.9. During the initial stage of the capping procedure (Figure 4.9(a)), the indium atoms detach from the QD and intermix with GaAs. This results in an InGaAs profile with non-uniform indium content as shown in Figure 4.9 (b). The indium intermixing and detachment occur simultaneously during the capping on both the wetting layer surface and the QD surface therefore suggest that the profile of the indium looks as shown in Figure 4.9(c). We estimate that the indium gradient about 10 nm thick while the height of capped QD is less than 4 nm. The capping effects on these large QD were also systematically studied by Joyce et al. (2001b).

The results shown in this section implies that, in the case of the growth of stacked QDs, where another self-assembled QD layer is grown on the thin GaAs capped QD surface, the intermixing and undulated growth surface also affect the structural composition and shape of the second and subsequent QD layer (Lipinski et al., 2000; Le Ru et al., 2002).

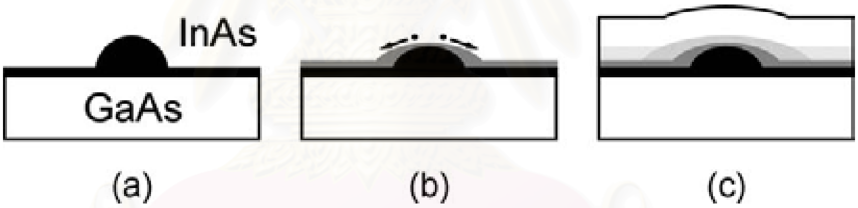

Figure 4.9 Schematic illustration of the capping procedure of InAs QD. (a) A free-standing QD collapses during capping with thin GaAs. (b) InAs atoms detach from the QD and diffuse to intermix with GaAs on flat GaAs surface. (c) Intermixing of the indium and gallium atoms during cap smooth the compositional profile.

CHAPTER 5

Homogeneity Improvement

The key experiments of this thesis are presented in this chapter. We investigate techniques to improve the QD size homogeneity including the introduction of growth interruption (GI), a repetitive desorption-regrowth procedure, low-temperature capping, and *in situ* etching. The interested QD arrays are both the large, low-density QDs and small, high-density QDs, which were initially grown at different growth rate.

5.1 Growth Interruption

In this section, the effects of a GI after QD formation are studied using three types of QD ensembles which are grown by using different growth conditions, namely, 1.8 ML InAs at low growth rate, high growth rate, and 2.2 ML InAs at low growth rate.

Figure 5.1 shows 1×1 μm^2 AFM images of 1.8 ML InAs QDs grown at a low growth rate (0.01 ML/s) with various GI times. The 500×500 nm^2 areas shown at the top-right corner of Figures 5.1(a) and (b) were have been adjusted to yield a high-contrast height scale (2 nm). These high-contrast images emphasize the difference between the as-grown QDs and QDs with a 30 s GI. As shown in Figure 5.1(a), besides large InAs QDs, small InAs clusters, which originate from small 2D island (cf. Figure 4.3) are distinctly observed on the flat wetting layer (WL) surface area. These InAs clusters have sizes of less than 30 nm in width and 2-3 nm in height (marked by an arrow). These clusters completely disappear after a 30 s GI was introduced (Figure 5.1(b)). Figures 5.1(c) and (d) reveal that the density of the low-growth-rate QDs is still in the range of $\sim 3\text{-}6\times10^9$ cm^{-2} while the QD height slightly decrease when 60 s and 120 s GIs are introduced. Extending the GI time to 1000 s, these QDs completely disappear due to the thermal desorption (not shown).

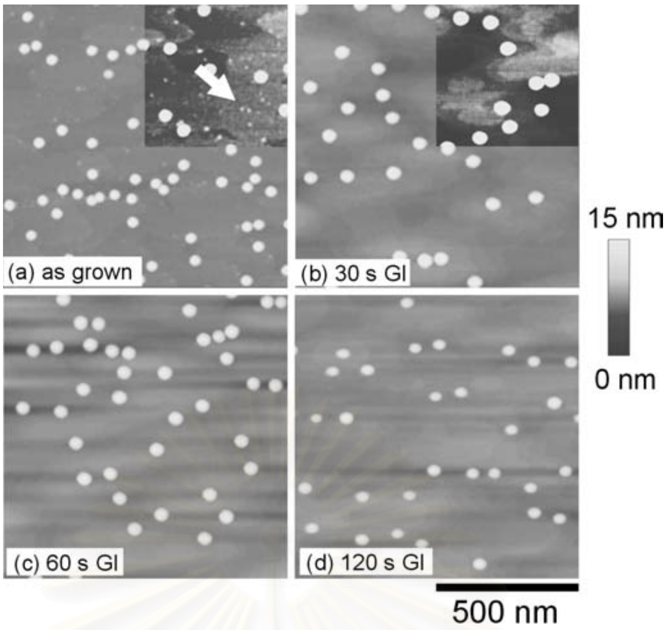

Figure 5.1 The 1×1 μm^2 AFM images of 1.8 ML InAs QDs grown at a low growth rate (0.01 ML/s) with (a) as grown, (b) 30 s GI, (c) 60 s GI, and (d) 120 s GI. The insets of (a) and (b) are high-contrast images (2 nm height scale).

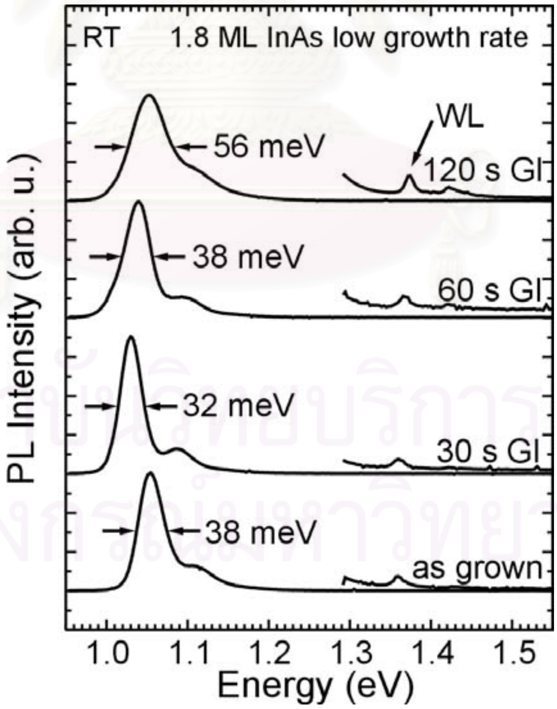

Figure 5.2 Room-temperature PL spectra of 1.8 ML InAs QDs grown by using a low growth rate with various GI times. The excitation power for the QD peak is 5 mW, whereas the excitation power for the WL peak is 50 mW.

Due to the rather low density of these QD arrays, the extracted height distribution from AFM results can not be used to explain the evolution in QD size homogeneity during GI. Therefore, we mainly use PL linewidth to interpret the size homogeneity resulted from this GI experiment. The room-temperature PL spectra of 1.8 ML InAs QDs grown by using the low growth rate and with 0, 30, 60, and 120 s GIs are shown in Figure 5.2. The PL peak energies of the ground state, the first excited state and of the WL are resolved. The linewidths of the ground-state peak, which correspond to the size homogeneity, are also indicated in the figure. These spectra show that the dot size uniformity is improved by using the 30 s GI compared with the growth without interruption and with this 30 s GI the linewidth is narrower from 38 meV to 32 meV. However, for even longer growth interruption times (more than 30 s GI), the PL linewidth broadens. The PL linewidth broaden to 56 meV for 120 s GI. Apart from the QD peak, we also find that the WL peak gradually shifts from 1.355 eV to 1.37 eV during the GI.

We can qualitatively explain the linewidth narrowing, which corresponds to the improvement in size homogeneity, by the local surface strain energy density contribution to the surface chemical potential (Seifert et al., 1999). According to the AFM and PL results, the atomic process during GI can be by a schematic shown in Figure 5.3. After the InAs WL formation, further depositing indium atoms causes the nucleation of 2D island. The increment in size of these 2D islands to larger than the critical size induces 3D islands formation. This 3D island or QD formation behave like a material sink for indium adatoms. During the growth of InAs layer there coexists 2D islands (InAs clusters) and 3D island (QD). As depicted in Figure 5.3(a), the InAs clusters have a higher total energy i.e. they are unstable compared with QD. Thus, during the GI thermal activation can easily cause indium atom detachment from the remaining InAs clusters. These detached indium atoms become adatoms, which then diffuse to the surface. This phenomenon provides an explanation for the disappearance of InAs clusters after early GI. During the GI process, the migrating indium adatoms look for more stable sites to be incorporated. However, the adatoms have to overcome the high strain energy barrier at the edge of the large QDs, causing a preferential attachment of indium adatoms to the smaller QDs as shown in Figure

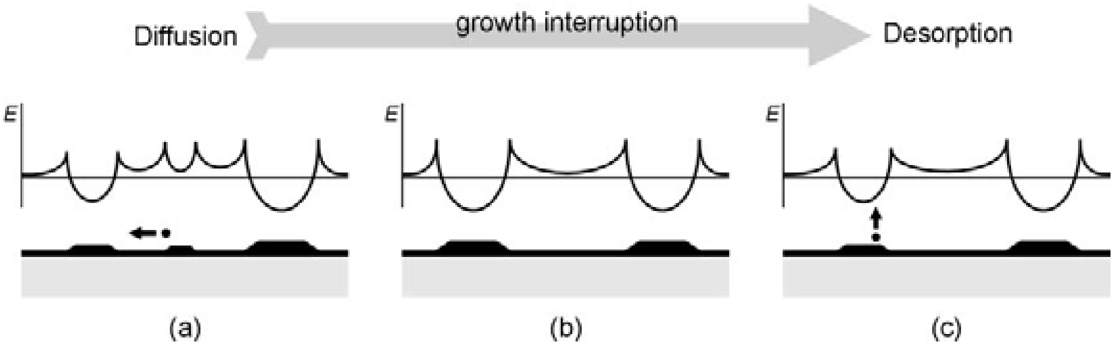

Figure 5.3 Schematic representation of atomic processes occurring during GI. The top panel shows the corresponding local surface strain energy density. (a) the InAs cluster is less stable, hence leading to the detachment of indium atoms from the clusters to the small InAs QD. (b) The diffusion process improves the size homogeneity of QD ensembles. (c) Indium atoms from the QDs start to desorb when the GI time is increased. This desorption process causes the strain energy to decrease, and thus indium atoms from the QD can diffuse out of the QD. This desorption results in the decrease of the QD size. Hence, the homogeneity worsens.

5.3(a). Because smaller QD has less potential barrier, this results in the improvement of the homogeneity of QDs (Figure 5.3(b)). Moreover, the QD size is larger at the initial GI as observed by AFM as shown in Figures 5.1(a) and (b). For a substrate temperature of 500°C, besides the diffusion of adatoms on the surface, some atoms may be desorbed due to thermal activation process. The desorption decreases the total number of indium atoms in the system (consisting of WL, InAs clusters, and QDs). After the InAs clusters completely disappear, the indium atoms from the QDs are detached and/or desorbed due to thermal activation energy. Consequently, QD size decreases. The dot size decrement decreases the energy barrier of the QDs and enhances the dissolution of indium adatoms from these dots. Therefore, a further increase of the GI time after the InAs clusters disappear leads to a decrease of the homogeneity. This behavior is evidenced by the PL linewidth broadening of the QDs grown with more than 30 s GI. A schematic diagram of the desorbing QD is shown in Figure 5.3(c).

The growth interruption effects on the high-growth-rate QDs are also studied. The situation is entirely different to the low-growth-rate QDs. Figure 5.4 shows the 1×1 μm^2 AFM images of QDs grown at a high growth rate (0.2 ML/s) with various GI times. The 500×500 nm^2 areas at the top-right corners of Figures 5.4(a) and (b) have been adjusted to yield a high-contrast height scale (2 nm) similar to these in Figure 5.1(a) and (b). In Figure 5.4(a), we do *not* observe InAs clusters on the surface compared with Figure 5.1(a). During the initial GI stage (0 – 60 s), the dot density decreases the dot size increases. After long GI time (120 s), the atoms from the QDs start to desorb, and the dot size and dot density drastically decreases.

The room-temperature PL spectra of 1.8 ML InAs QDs grown at the high growth rate with 0, 30, 60, and 120 s GI are shown in Figure 5.5. The PL peak energies of the ground state, the first excited state and the WL are not well resolved. The WL peaks are not shown in this figure. The PL spectra show that the dot size uniformity worsens by using the GI. The linewidth increases from 51 meV to 87 meV when the GI time is increased from 0 s to 120 s. Moreover, the peak intensity decreases after a longer GI time.

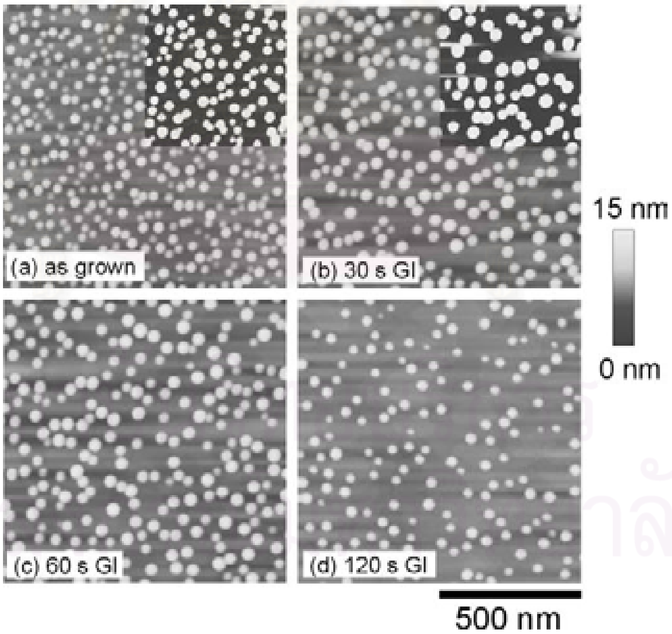

Figure 5.4 1×1 μm^2 AFM images of 1.8 ML InAs QDs grown at a high growth rate (0.2 ML/s) in (a) as grown, (b) 30 s GI, (c) 60 s GI, and (d) 120 s GI. The insets of (a) and (b) are high-contrast images.

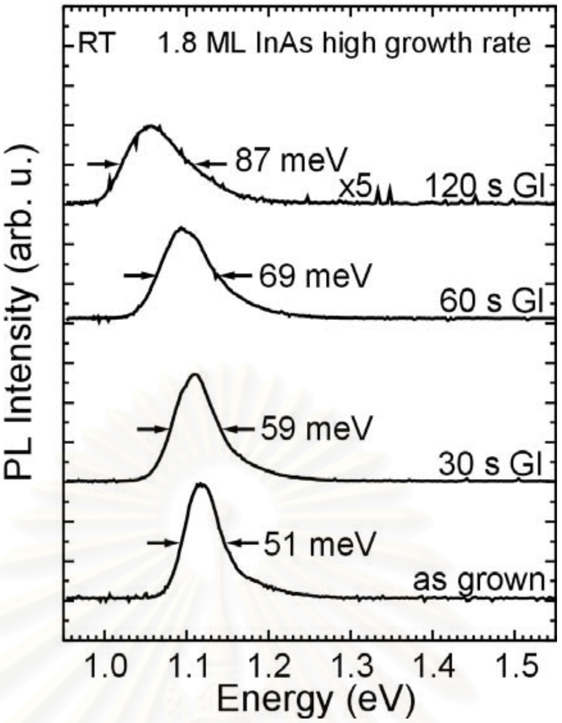

Figure 5.5 Room-temperature PL spectra of 1.8 ML InAs QDs grown at a high growth rate (0.2 ML/s) with various GI times. The excitation power is 5 mW.

From the AFM and PL results of high-growth-rate QDs grown with different GI times, we may describe the formation evolution as follows. From the AFM image of the as-grown QDs with the high growth rate in Figure 5.4(a), we do not observe the InAs clusters on the surface. For a high growth rate, the diffusion length of indium adatoms on the surface decreases and the indium adatoms have a smaller chance to be incorporate into the most stable sites. The 2D islands or InAs clusters, which we can observe in the case of QDs grown at the low growth rate, attract enough material to grow and become 3D islands. Due to material conservation, the high-density QDs have a smaller average size. We observe that the dot size distribution shows a bimodal behavior. The larger QDs in these arrays are more stable, therefore the indium atoms detach and diffuse from the smaller QDs to the larger ones, and hence causing the decrease of the QD density and an increase of QD size at the initial GI stage (Figure 5.4(a) and (b)). Since these small QD arrays are more stable compared with the InAs clusters, these small QDs will not rapidly dissolve; we observe in the AFM images that there exist the remaining of small QDs, which become smaller during GI and thus induce the PL linewidth broadening. The small QDs disappear after a long GI time (~ 60 s), and consequently, the PL peak redshifts to a lower energy. Due to a smaller QD density, the PL peak intensity decreases.

The last type of QD arrays, which is studied in these GI experiments, is the 2.2 ML InAs QDs grown at a low growth rate. Figure 5.6 shows the 1×1 μm^2 AFM images of QDs grown at a low growth rate (0.01 ML/s) with various GI times. The 500×500 nm^2 area shown at the top-right corner of Figure 5.6(a) has been adjusted to yield a high-contrast height scale (2 nm). In Figure 5.6(a) we do not observe InAs clusters on the surface compared with Figure 5.1(a). The disappearance of InAs clusters might occur during the growth of InAs QDs after their formation. During the deposition of InAs ~ 40 s after the QD formation (from 1.8 ML to 2.2 ML, at the growth rate of 0.01 ML/s), the indium atoms from the InAs clusters diffuse to attach to the nucleated QDs. Therefore, the as-grown QDs in this case might be equivalent to the QDs grown at the low growth rate with a 40 s GI. The increment of amount of deposited material results in increase in size of *some* QDs. During the GI, the

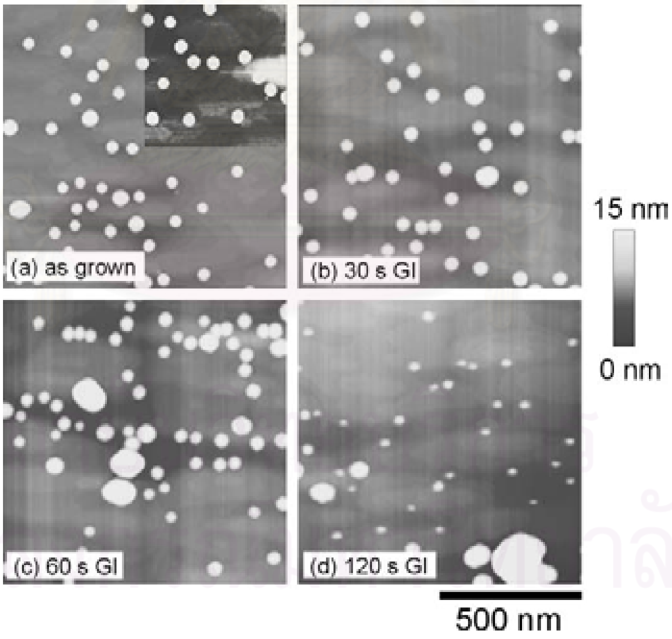

Figure 5.6 1×1 μm^2 AFM images of 2.2 ML InAs QDs grown at a low growth rate (0.01 ML/s) with (a) 0 s GI, (b) 30 s GI, (c) 60 s GI, and (d) 120 s GI. The inset of Figure (a) is a high-contrast image.

extraordinary large dots act as a sink for adatoms diffusion, and so the large QDs become larger while the QDs, which have an average QD size become smaller. Finally, due to the desorption, the QDs disappear.

The room-temperature PL spectra of 2.2 ML InAs QDs at a low growth rate (0.01 ML/s) with 0, 30, 60, and 120 s GIs are shown in Figure 5.7. The PL intensity reduced by an order of magnitude when the GI is applied. This might correspond to defect formation within extraordinary large QDs. Due to this defect formation, these QD array might not suitable for optical application. Therefore, the homogeneity is not concerned in this case.

The PL peak energies and linewidths of 1.8 ML InAs QDs grown at low and high growth rates are summarized in Figures 5.8(a) and (b), respectively. In Figure 5.8(a), the PL blueshift of low-growth-rate QDs with GI more than 45 s is attributed to a height reduction of the QDs due to the indium desorption. From the AFM results of these QDs with long GI (45-120 s), the density of the low-growth-rate QDs does not change but the height is decreased. The PL spectra of the high-growth-rate QDs, in contrast, show a clear redshift, which we assign to an increasing diameter and

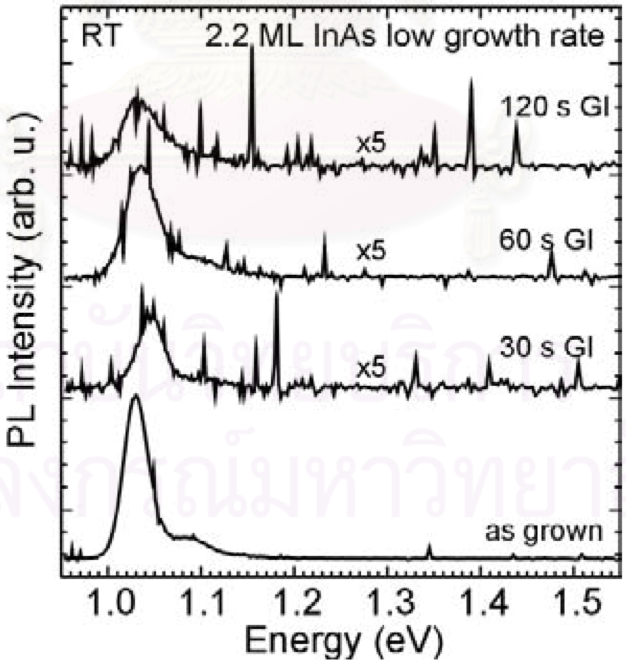

Figure 5.7 Room-temperature PL spectra of 1.8 ML InAs QDs grown with various GI time at low growth rate (0.01 ML/s). The excitation power for the QD peak is 5 mW.

height of the existing QDs (measured by AFM). We attribute the increase in the QD size to the diffusion of the atoms from less stable QDs to more stable QDs. This also corresponds to a reduction of the high-growth-rate QDs' density when the GI time is increased. Comparing Figure 5.2 and 5.5, we find that the effects of the GI on the PL spectra of the low-density, low-growth-rate QDs are evidently different from the high-density, high-growth-rate QDs. The former shows a linewidth narrowing and a peak blueshift, and the latter shows a linewidth broadening and a continuous redshift of the PL peak. Figure 5.8(b) shows the relationship between the full width at half maximum (FWHM) of the QD's PL emission spectrum and the GI time. Whereas the FWHM of the high-growth-rate QDs becomes increasingly broad, the low-growth-rate QDs exhibit a distinct minimum at around 30 s GI. The narrowing of PL linewidth originates from the diffusion of indium atoms from the InAs clusters to the QD during the initial stage of the GI.

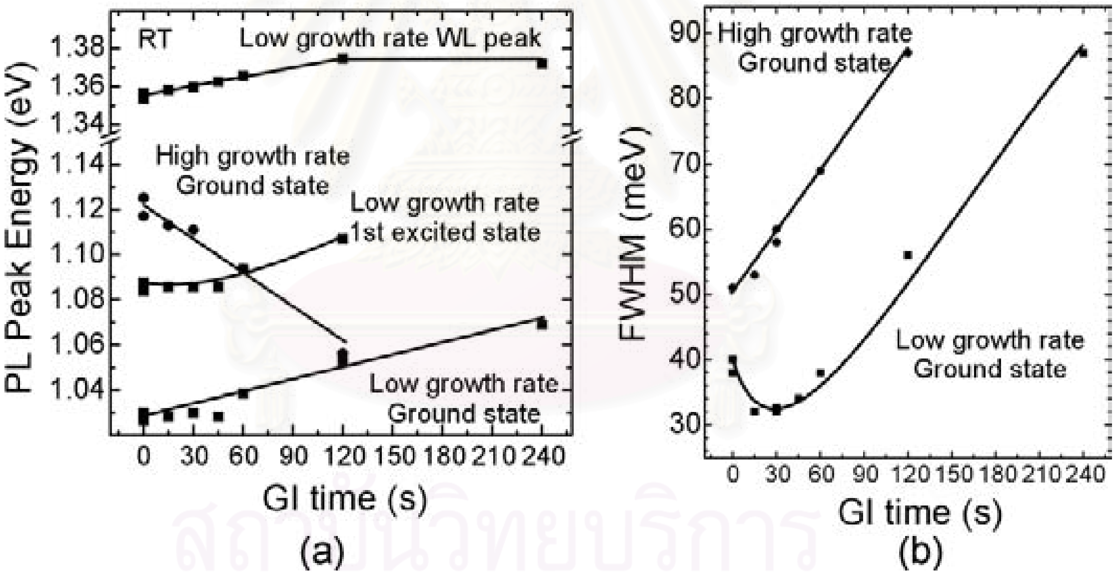

Figure 5.8 (a) Dependence of PL peak energy of 1.8 ML InAs QDs on various GI times for a low growth rate (0.01 ML/s) (square) and at a high growth rate (0.2 ML/s) (circle). (b) The dependence of the linewidth of 1.8 ML InAs QDs on various GI times at the low growth rate (square) and the high growth rate (circle).

5.2 Repetitive Desorption-Regrowth

Based on the GI experiments, the diffusion of adatoms seems to be one parameter, which can be used to improve the size homogeneity of QD ensemble. However, the improvement by the GI technique is prevented by the desorption process. A repetitive desorption-regrowth technique is proposed to maintain a constant number of indium adatoms on the surface (Schmidt et al., 2002), and to prolong the diffusion time of indium adatoms. With this technique, we allow the desorption of atoms from the QD surface for a limited time interval and then deposit the same amount of indium atoms during the regrowth time. The results on both large (low-growth-rate) and small (high-growth-rate) QDs are presented in this section.

The PL and AFM results from the repetitive desorption-regrowth experiments on the large QDs are shown in Figure 5.9. This repetitive desorption-regrowth cycle is done by 15 s GI and 0.03 ML InAs re-deposition. From this experiment the spectrum narrows from 38 meV to 32 meV after a 15 s GI. This linewidth remains constant at 32 meV for 1-time, 2-times, and 5-times repetitive desorption-regrowths. The linewidth broadens to 38 meV for 10-times repetitive desorption-regrowth. This PL linewidth broadening might be due to the experimental calibration error during the growth. The long growth time (~ 150 s GI for 10 time repetitive desorption-regrowth) results in more experimental error. The QDs measured by AFM as shown in Figures 5.9(b) and (c) have almost the same height and diameter. The results reveal that the large, low-density QDs are more stable and the adatoms variation has less effect on these QD arrays. The linewidth of 32 meV corresponds to the best homogeneity obtained from the QDs. (Note that an improved PL linewidth is achieved if the capping temperature is changed. See Section 5.3.)

In contrast to the large, low-density QDs, the repetitive desorption-regrowth technique can be used to improve the size homogeneity for the small dots with high density. The AFM images and the corresponding height histograms of the QDs grown at a high growth rate with repetitive desorption-regrowth using 30-s GI and 0.1 ML InAs re-deposition several times are shown in Figure 5.10. The size distribution is determined by fitting the height histogram with a Gaussian function and measuring in

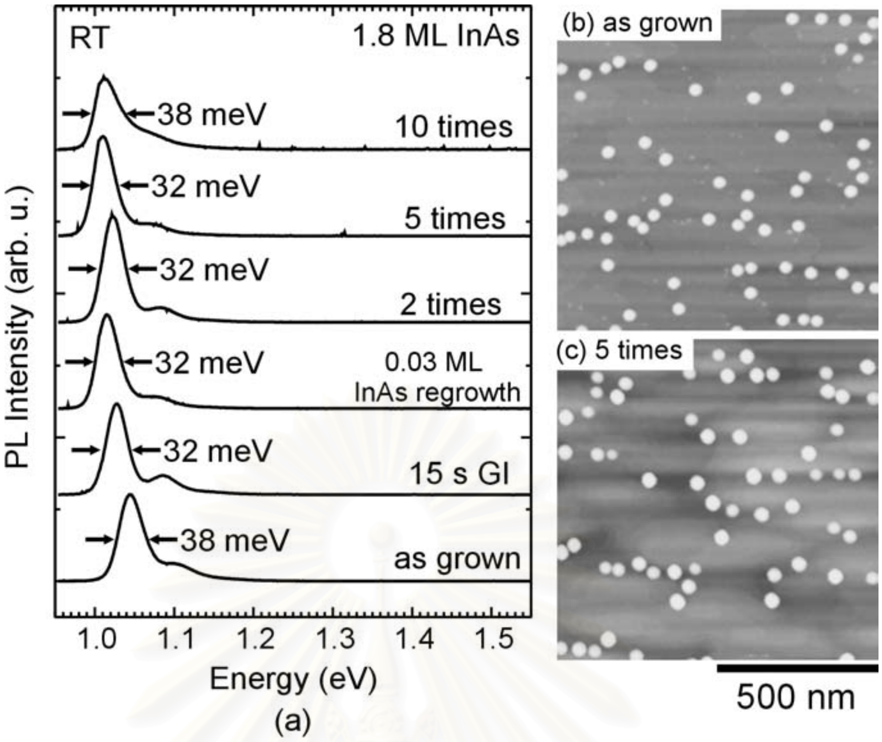

Figure 5.9 (a) Room-temperature PL spectra of 1.8 ML InAs QDs grown at a low growth rate with repetitive desorption-regrowth technique. The PL linewidth is constant at 32 meV for several repetitive desorption-regrowth times. The broadening at 10 times repetitive desorption-regrowth might be due to the calibration error during growth. (b) 1×1 μm^2 AFM image of as grown QD array, and (c) 1×1 μm^2 AFM image of 5-times repetitive desorption-regrowth QD array.

terms of the FWHM. The percentage value is calculated by normalizing the FWHM to the average QD height. It is clearly seen from these results that the 10-times repetitive desorption-regrowth QDs in Figure 5.10(c) are more homogeneous than the as-grown and the 5-times repetitive desorption-regrowth QD arrays. The broad size distribution at 5-times repetitive desorption-regrowth might correspond to the transition in shape of some QDs in the array. Note that the QD densities of these regrowth samples are almost identical (~2×10^{10} cm^{-2}) after a 30 s GI. The decrease of the QD density for an as-grown sample (compared with the 30 s GI QDs) was already discussed in the previous section.

The QDs fabricated by the repetitive desorption-regrowth procedure were capped for PL measurement. The room-temperature PL spectra of these samples are shown in Figure 5.11. Note that the PL spectrum from as-grown sample with linewidth of 51 meV is shown in Figure 5.5. The broadening of the linewidth agrees well with the AFM results (Figure 5.10(b) for 5-times repetitive desorption-regrowth). However, the 10-times repetitive desorption-regrowth sample shows a distinct narrowing of the linewidth to 39 meV which agree with the size homogeneity improvement observed in AFM. The redshift of the peak energy is due to the change in QDs shape during repetitive desorption-regrowth. This is due to the fact that the height of these self-assembled QD highly affects the peak energy. The change of QD

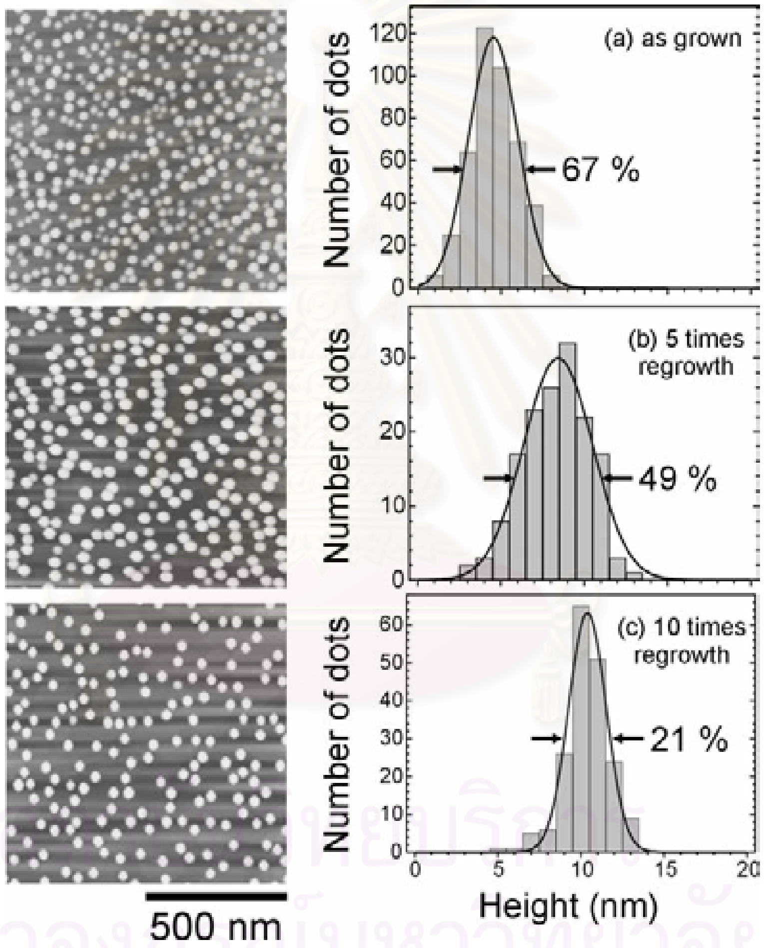

Figure 5.10 1×1 μm^2 AFM images and the corresponding height histograms of (a) as-grown QD array, (b) 5-times repetitive desorption-regrowth QD array and (c) 10-times repetitive desorption-regrowth QD array. One repetitive desorption-regrowth step comprises a 30 s GI and 0.1 ML InAs deposition. The histograms have been fitted with a Gaussian distribution and the variation in QD heights is normalized to the average height.

shape during repetitive desorption-regrowth from low to high aspect ratio might be similar to the case of different amounts of InAs deposition (Mukhametzhanov et al., 1999; Saito et al., 1999).

The effects of the repetitive desorption-regrowth technique on the QD size uniformity can be schematically explained as shown in Figure 5.12. From the evidence that the formed QDs have different properties (size, density, size distribution) when we change the kinetic parameters during growth (mainly the growth rate). We believe that the QDs form by the kinetic-controlled process (Dobbs et al., 1997; Meixner et al., 2001). After the QD formation, the system, which consists of QDs on the flat WL surface with 2D islands (platelet) and adatoms, approaches equilibrium by the adatoms' diffusion process. Due to the statistical nature of the QD size distribution, the approach towards thermodynamic equilibrium

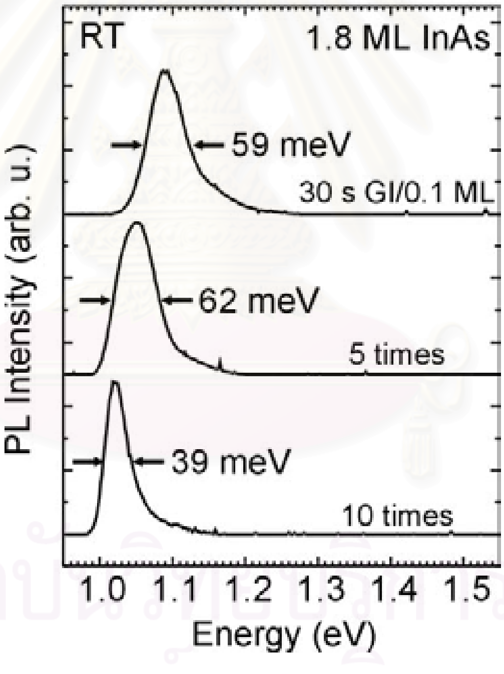

Figure 5.11 Room-temperature PL spectra of the high-growth-rate QD samples with 1, 5, and 10 repetitive desorption-regrowth times. Note that the PL of the as-grown sample has previously been shown in Figure 5.5.

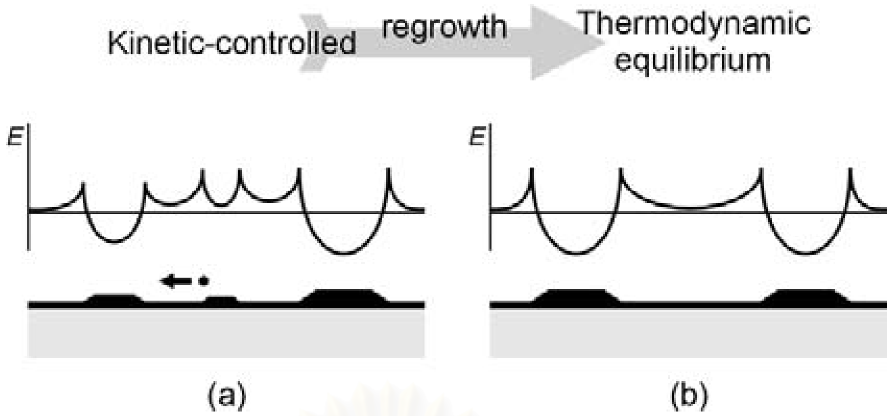

Figure 5.12 Schematic representation of atomic processes occurring during repetitive desorption-regrowth. The top panel shows the corresponding local surface strain energy density. In Figure (a), the indium atoms in InAs cluster are less stable, so they detached from the cluster and preferentially diffuse to the small InAs QD. The diffusion process improves the size homogeneity of QD arrays, as shown in Figure (b). The repetitive desorption-regrowth of indium atoms suppresses the desorption process, so the homogeneous QD arrays can be obtained.

for a QD array might take a long time. While the QDs approach the equilibrium via adatoms' diffusion, some QDs might dissolve, and the QD size and shape might change. Moreover, there is also desorption, which complicate this process. The repetitive desorption-regrowth technique can be used to compensate the desorption of indium atoms from the surface, and this results in homogeneous high-density QD arrays.

From a practical point of view, this repetitive desorption-regrowth technique is difficult to realize. This is because there exists an error in the calibration of temperature, and the growth rate (flux). The errors are obvious when the repetitive desorption-regrowth time is increased. This problem reduces the reproducibility of the QD samples.

5.3 Low Temperature Capping

As discussed in Section 4.4, the capping process drastically changes the QD shape and size. In this section, we will first investigate low temperature capping, which can be used to improve the homogeneity of QD and make the emission wavelengths to redshift (Lipinski et al., 2000; Eberl et al., 2001). Because the QDs are capped, the improvement of the QD size homogeneity is induced from the PL linewidth. The homogeneity improvement on both low- and high-growth-rate QDs are presented in this section.

Figure 5.13 shows the 1×1 μm^2 AFM images and the corresponding linescans of a capped-QD nanostructure along [1-10] direction. The capping of the first 6 ML GaAs is performed at 470°C. Then, the substrate temperature is ramped up to 500°C while continuing to deposit the GaAs cap. The QDs capped by this process are called low temperature capped (LTC) QDs. The LTC QDs approximately experience the same collapsed height as that of the conventionally capped (CC) QDs (see Section 4.3). The QD height for thin GaAs layers is about 4 nm. This implies that the effects

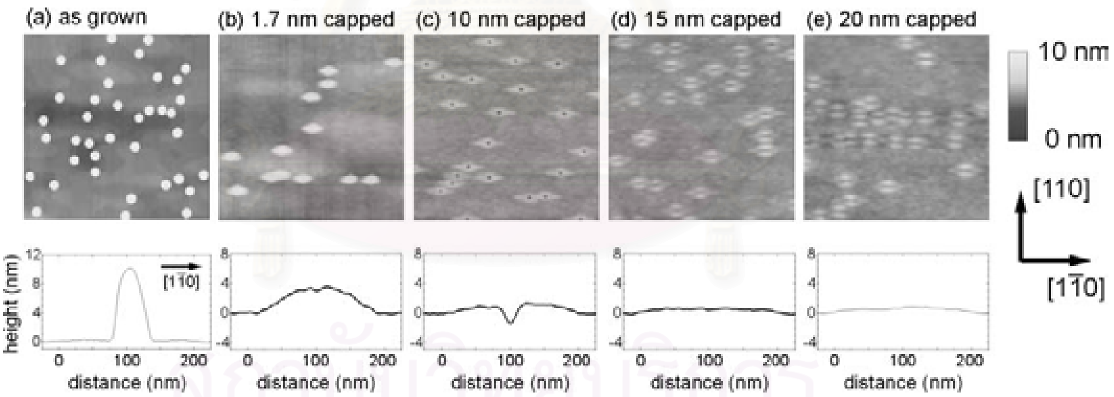

Figure 5.13 1×1 μm^2 AFM images of the 1.8 ML InAs QDs with thin GaAs capping layer thicknesses: (a) as-grown, (b) 1.7 nm (6 ML) capped, (c) 10 nm capped, (d) 15 nm capped, (e) 20 nm capped. The bottom row is the cross section of a nanostructure. Obviously, the shape of QDs drastically changes during the cap. Nanostructures on the top of the QDs develop into rhombus-shaped structures with a hole in the middle and ridge-valley structures for 10 nm thick caps and 15 and 20 nm caps, respectively. (Heidemeyer et al., 2002)

of the capping process do not exclusively depend on the capping temperature. This phenomena may be described by the increase of elastic strain energy during capping and the wetting layer formation (Ledenstov et al., 1996; Songmuang et al., 2003). However, capping at different temperatures provides different degrees of intermixing, which alter the morphology of the thicker GaAs capping surface.

Compared with the CC QDs (cf. Figure 4.11), the low temperature capping produces different morphologies on the thin GaAs capping layer. For capping the QDs at a low temperature with 10 nm GaAs, we observe rhombus-shaped structures with a hole in the middle (Heidemeyer et al., 2002). The hole has a depth of approximately 0.7 nm with respect to the surface level of the sample and is surrounded by a rim of 1 nm high. The width and the length of the nanostructures are approximately 66 nm in the [110], and approximately 150 nm in the [1-10] direction, respectively. When the capping layer thickness is increased to 15 nm, the rhombus-shaped structure with a hole in the middle will make a transform into an island with a trench through the center. This structure is called ridge-valley structure (Joyce et al., 2001b). The structure is oriented in the [1-10] direction and the bottom of the valley is at the same level as the surface of the sample. The ridge has a height of approximately 1.6 nm, measured along the [110] direction. The observed results are believed to originate from the surface diffusion of gallium adatoms, which are in turn driven by the surface curvature and the surface strain profile (lattice parameter mismatch) (Joyce et al., 2001a).

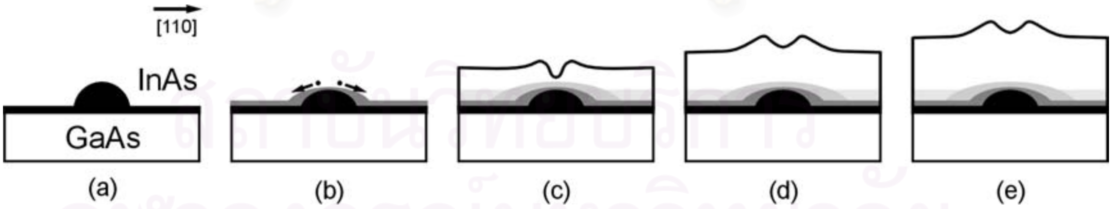

Figure 5.14 Schematic illustration of the QD capped at a low temperature. (a) A free-standing InAs QD. (b) The QD collapses during capping with thin GaAs. The indium atoms detach from the QD and diffuse to intermix with GaAs on a flat GaAs surface. Due to less intermixing at the low temperature capping, the indium compositional profile induces non-preferential growth on the top of the QDs (c). (d) and (e) The effects of the compositional profile are less pronounced for thick capping layer thicknesses.

The evolution of the morphological features is schematically shown in Figure 5.14. In Figure 5.14(a) the initial QDs are formed on the surface by the deposition of 1.8 ML InAs and a 30 s GI. For the capping layers, the QDs collapse, similarly to the case of capping at the conventional temperatures (cf. Figure 4.13). The collapse of the QDs provides additional indium adatoms on the GaAs capping layer surface. The intermixing of gallium and indium, which occurs at this stage, forms a non-uniform InGaAs layer on both the WL surface and around the QD regions. For further capping with GaAs, the gallium adatoms prefer not to grow on the top of the QDs due to the highly relaxed InAs at those areas. In addition, the surface curvature also drives the gallium adatoms out of the convex surface. The GaAs prefers to grow around the QDs because the relaxation of InAs on the QDs compresses the lattice spacing of the WL around the QDs. Including the effects of anisotropic diffusion length of Ga adatoms, the rhombus-shaped structure with a hole in the middle is formed as shown in Figure 5.14(c). For further deposition of GaAs, the strain field from the InAs QDs decreases, and the surface is flattened due to the adatom diffusion, which depended on the surface curvature (Barabási and Stanley, 1995). Eventually, the hole develops into a flat surface and the nanostructure gradually disappears after a 30 nm GaAs capping.

Low-temperature PL of near surface LTC QDs is performed in order to confirm the difference of the InAs profiles of the LTC QDs and the CC QDs. The result is shown in Figure 5.15. The three peaks on the high energy (1.44-1.52 eV) are similar to the case of CC QDs (cf. Figure 4.12). Although the morphologies of the LTC QDs with 15 nm and at 20 nm cap are similar, the LTC QDs starts to emit light for 20 nm GaAs capping. The PL peak position for both the WL and the QDs are quite different from those of the CC QDs, which start to emit light at 10 nm GaAs capping. This result can be partially explained by the effect of intermixing. The InAs profile smears out due to the intermixing and provides alternation of confinement potential. For large intermixing in CC QDs, the confinement potential is shallow and broadens so the PL peaks from the transition in the quantized state of both the QDs and the WL are observed at higher energy. However, the contribution of surface relaxation (Pistol et al., 1995; Kamiya et al., 1998) and of surface states (Yu and Cardona, 1999) are also important to explain the dependence of PL intensity on the capping layer thickness.

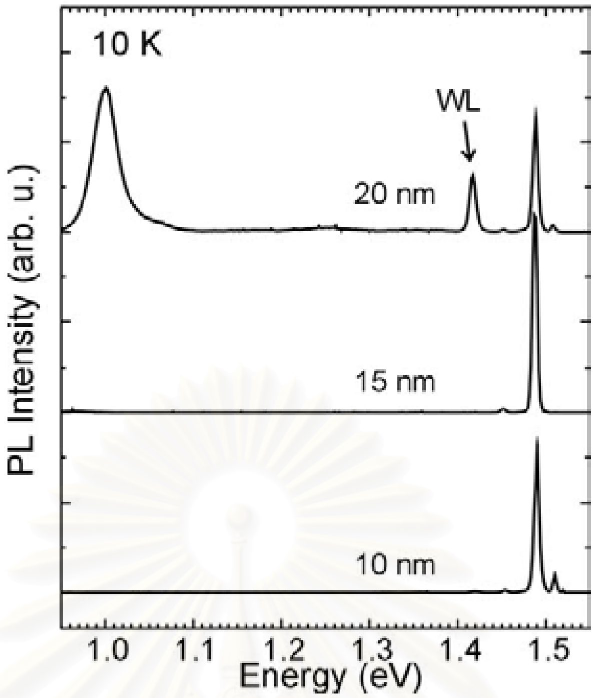

Figure 5.15 Low-temperature PL spectra of low temperature capped InAs QDs near the surface. The GaAs cap layer thickness is indicated for each spectrum. The QDs start to luminesce at 1.00 eV for 20 nm cap thickness, which implies that the indium composition in the QDs is different to the case of capping at the conventional growth temperature (500°C). (Compared with Figure 4.13)

For the QDs grown at high growth rates, we did not investigate the morphology evolution due to the less stable nature of these QDs. The reader is referred to the works published by Joyce et al. (2001a) and Ferdos et al. (2002) for the high-growth-rate QDs.

The influence of the capping temperature on the optical properties of the QDs is investigated by PL measurements. Figure 5.16 shows comparative room-temperature PL spectra of the CC QDs and the LTC QDs grown at growth rates of 0.01 ML/s (upper panel) and 0.2 ML/s (lower panel). The PL peaks of the QDs overgrown at the low temperature show a clear redshift for both large and small dots. The shifts of the peak energy are 95 meV and 112 meV for the large (low-growth-rate) and small (high-growth-rate) QDs, respectively. Furthermore, the linewidths decrease from 38 and 51 meV to 23 and 26 meV with decreasing overgrowth

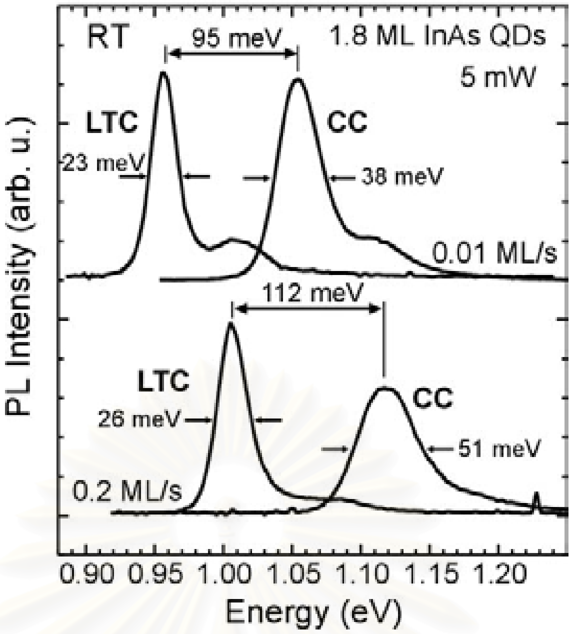

Figure 5.16 Comparative room-temperature PL spectra of conventionally capped (CC) InAs QD and low-temperature capped (LTC) QDs grown at both low growth rate (0.01 ML/s) and high growth rate (0.2 ML/s).

temperature, respectively. The 1.3-μm emission can be achieved by a combination of the low-growth-rate and low-temperature capping techniques. The narrower linewidth of the LTC QDs compared to that of the CC QDs implies that the conventional capping process significantly affects the homogeneity of the QDs, especially for the small QDs grown at high growth rate. We attribute the redshift and the linewidth narrowing mainly to the suppression of indium-gallium intermixing during the GaAs overgrowth at low temperatures. In addition, the LTC technique is expected to partially preserve the indium profile in the QDs during the capping process (Eberl et al., 2001). The PL results reveal that the indium-gallium intermixing has a strong effect on the small QDs. We explain this circumstance by the higher ratio of the surface area to the volume of small dots. Since intermixing removes material from the surface, the small QDs, which have a high ratio of surface area to volume, should show a stronger intermixing effect. This indium-gallium intermixing can also be suppressed by using a strain-reducing layer (Schmidt et al., 2002; Nishi et al., 1999).

5.4 *In Situ* Etching

The homogeneity of low-growth-rate QDs can also be improved by introducing an $AsBr_3$ etching gas to the InAs QD surface. Figure 5.16 shows the room-temperature PL spectra and the corresponding 1×1 μm^2 AFM images of 1.8 ML InAs QD grown at 0.01 ML/s and etched with $AsBr_3$ *in situ* etching gas for various etching times. In this experiment, the flow rate of the etching gas is calibrated to be 0.010 sccm (0.03 ML/s GaAs removal rate). During etching of the QD surface, we observe a PL linewidth narrowing from 38 meV (cf. Figure 5.2), to 34 meV at the initial etching stage. This might be explained in a similar way to the case of the GI. Due to the lower stability of InAs clusters, the etching gas might prefer to attach to the indium atoms of the InAs clusters and desorb. Therefore, the size homogeneity can be improved.

However, there are two differences between the GI and the etching. First, the etching accelerates the time for InAs desorption. By applying the etching gas to the QD surface, a flat surface is observed after 40 s etching time. Second, the etching produces a clear anisotropic QD shape as shown in the AFM image for 24 s etching (Figure 5.17(c)).

In the technical viewpoint, the etching technique might not suitable for improving homogeneity of the QD ensemble. This is because we can obtain the same results by using a simple GI.

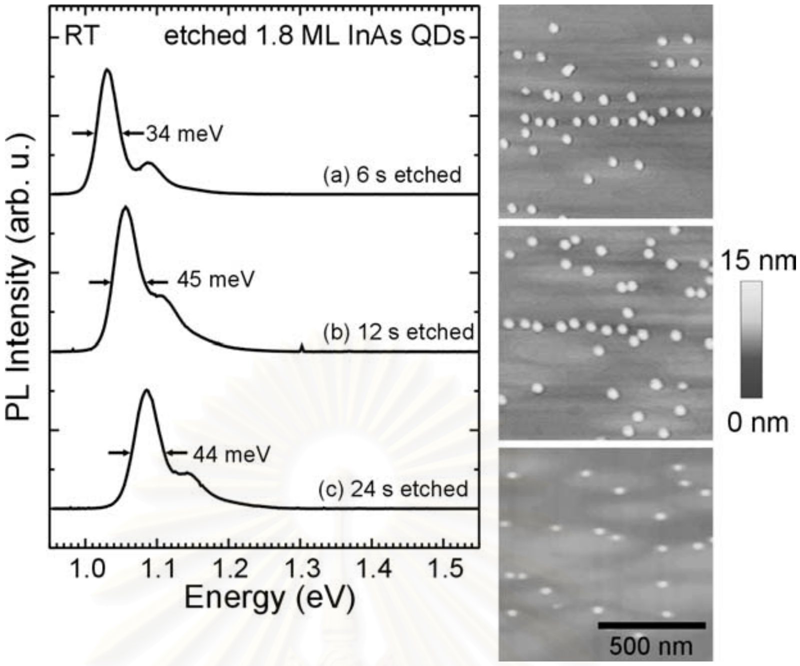

Figure 5.17 Room-temperature PL spectra and the corresponding 1×1 μm^2 AFM images of 1.8 ML InAs QDs grown at 0.01 ML/s and etched with $AsBr_3$ *in situ* etching gas for (a) 6 s, (b) 12 s, and (c) 24 s. The anisotropic etching produces elliptic QDs as shown in the AFM image of 24-s etched QDs.

CHAPTER 6

Conclusions

This work presents several growth techniques to improve the size homogeneity of InAs/GaAs self-assembled QD grown by MBE in the Stranski-Krastanow growth mode.

First, a brief overview on the properties of low-dimensional nanostructures, especially QDs, was given. As examples, several fabrication methods to realize QD structures were described. Details of self-assembled growth in the Stranski-Krastanow mode were given. From material considerations, the InAs/GaAs QDs are chosen for applications in optoelectronics.

In situ RHEED observations were used to calibrate the substrate temperature and the growth rates. The structural properties and the size homogeneity of QD samples were characterized by *ex situ* AFM and room-temperature PL.

The conventional growth of InAs/GaAs self-assembled QDs was investigated before presenting techniques, which use to improve the size homogeneity. The growth was divided into 3 stages: layer-by-layer growth, island (QD) growth, and cap-layer growth. The effects of growth rate on the QD structure were studied. Large, low-density and small, high-density QDs were realized by changing the InAs growth rates. For the capping of large QD at a growth temperature of 500°C, the mound-shaped structure on the top of the QD region could be observed.

The techniques to improve the QD's size homogeneity in this work can be divided into 4 categories:

1. Growth interruption for 30 s can improve the homogeneity of large, low-density QDs. The homogeneity improvement was confirmed by narrowed PL linewidth: from 38 meV to 32 meV. This phenomenon can be explained by a dependence of an adatom diffusion process on the strain energy potential of the surface decorated with QDs.
2. For small, high-density QDs, the homogeneity can be improved by repetitive desorption-regrowth technique. By this repetive desorption-regrowth technique, the homogeneity improved as can be seen from the

size (height) distribution, which decreased from 67% to 21% as measured by AFM.

3. A low temperature capping technique improves the size and alloy homogeneity of InAs QDs in GaAs. By lowering the capping temperature to 470°C, large and small QDs exhibit a linewidth narrowing, to 23 and 26 meV, respectively.
4. *In situ* etching also improves the homogeneity of large, low-density QDs. The explanation of the size homogeneity improvement is by the removal of atoms from InAs clusters at the initial etching stage similar to the case of growth interruption.

REFERENCES

Alferov, Z. I. 2001. Nobel Lecture: the double heterostructure concept and its applications. Reviews of Modern Physics 73: 767-782.

Arakawa, Y., and Sakaki, H. 1982. Multidimensional quantum well laser and temperature dependence of its threshold current. Applied Physics Letters 40: 939-941.

Asada, M., Miyamoto, Y., and Suematsu, Y. 1986. Gain and the threshold of three-dimensional quantum-box lasers. IEEE Journal of Quantum Electronics QE-22: 1915-1921.

Barabási, A.-L. 1997. Self-assembled island formation in heteroepitaxial growth. Applied Physics Letters 70: 2565-2567.

Barabási, A.-L. 1999. Thermodynamic and kinetic mechanisms in self-assembled quantum dot formation. Material Science and Engineering B 67: 23-30.

Barabási, A.-L., and Stanley H. E. 1995. Fractal concepts in surface growth Cambridge: Cambridge University Press.

Bastard, G., and Brum, J. A. 1986. Electronic states in semiconductor heterostructures. IEEE Journal of Quantum Electronics QE-22: 1625-1644.

Bimberg, D., Grundmann, M., and Ledentsov, N. N. 1999. Quantum dot heterostructures. Chichester: Wiley.

Bottomley, D. J. 1998. The physical origin of InAs quantum dots on GaAs(001). Applied Physics Letters 72: 783-785.

Chen, Y., and Washburn, J. 1996. Structural transition in large-lattice-mismatch heteroepitaxy. Physical Review Letters 77: 4046-4049.

Cheng, K.-Y. 1997. Molecular beam epitaxy technology of III-V compound semiconductors for optoelectronic applications. Proceeding of IEEE 85: 1694-1714.

Cho, A. Y. 1983. Growth of III-V semiconductors by MBE and their properties. Thin Solid Film 100: 291-317.

Daruka, I., and Barabási, A. L. 1997. Dislocation-free island formation in heteroexpitaxial growth: a study at equilibrium. Physical Review Letters 79: 3708-3711.

Davies, J. H. 1998. Elastic and piezoelectric fields around a buried quantum dot: A simple picture. Journal of Applied Physics 84: 1358-1365.

Disseix, P., et al. 1997. Optical study of segregation effects on the electronic properties of molecular-beam-epitaxy grown (In,Ga)As/GaAs quantum wells. Physical Review B 55: 2406-2412.

Dobbs, H. T., et al. 1997. Mean-field theory of quantum dot formation. Physical Review Letters 79: 897-900.

Eberl, K., et al. 2001. Self-assembling quantum dots for optoelectronic devices on Si and GaAs. Physica E 9: 164-174.

Eliseev, P. G., et al. 2001. Ground-state emission and gain in ultralow-threshold InAs-InGaAs quantum-dot lasers. IEEE Journal on Selected Topics in Quantum Electronics 7: 135-142.

Esaki, L. 1986. A bird's-eye view on the evolution of semiconductor superlattices and quantum wells. IEEE Journal of Quantum Electronics QE-22: 1611-1624.

Esser, N., et al. 2001. Atomic structure and optical anisotropy of III-V(001) surfaces. Journal of Vacuum Science and Technology B 19: 1756-1761.

Farrell, H. H., and Palmstrøm, C. J. 1990. Reflection high energy electron diffraction characteristic absences in GaAs(100) (2x4)-As: A tool for determining the surface stoichiometry. Journal of Vacuum Science and Technology B 8: 903-907.

Faux, D. A., and Pearson, G. S. 2000 Green's tensors for anisotropic elasticity: application to quantum dots. Physical Review B 62: R4798-R4801.

Franke, T., et al. 1998. In situ RHEED, AFM, and REM investigations of the surface recovery of MBE-grown GaAs(001)-layers during growth interruptions. Journal of Crystal Growth 193: 451-459.

Gilmer, G. H., and Grabow, M. H. 1987. Models of thin film growth modes. Journal of Metal June: 19-23.

Gong, Q., et al. 1998 Analysis of atomic force microscopic results of InAs islands formed by molecular beam epitaxy. Journal of Crystal Growth 192: 376-280.

Grundmann, M., and Bimberg, D. 1997. Formation of quantum dots in twofold cleaved edge overgrowth. Physical Review B 55: 4054-4056.

Grundmann, M. 2000. The present status of quantum dot laser. Physica E: 5 167-184.

Heidemeyer, H., et al. 2002. Closely stacked InAs/GaAs quantum dots grown at low growth rate. Applied Physics Letters 80: 1544-1546.

Herman, M. A., and Sitter, H. 1989. Molecular beam epitaxy fundamentals and current status Berlin: Spinger-Verlag.

Jesson, D. E., et al. 1998. Self-limiting growth of strained faceted islands. Physical Review Letters 80: 5156-5159.

Joyce, P. B., et al. 2000. Effect of growth rate on size, composition, and optical properties of InAs/GaAs quantum dots grown by molecular-beam epitaxy. Physical Review B 62: 10891-10895.

Joyce, P. B., et al. 2001a. Shape and surface morphology changes during the initial stages of encapsulation of InAs/GaAs quantum dots. Surface Science 492: 345-353.

Joyce, P. B., et al. 2001b Surface morphology evolution during the overgrowth of large InAs-GaAs quantum dots. Applied Physics Letters 79: 3615-3617.

Kamiya, I., Tanaka, I., and Sakaki, H. 1998. Optical properties of near surface InAs quantum dots and their formation processes. Physica E 2: 637-642.

Kaneko, T., et al. 1995. Reentrant layer-by-layer etching of GaAs(001). Physical Review Letters 74: 3289-3292.

Keller, D., and Franke, F. 1993. Envelope Reconstruction of Scanning Probe Microscope Images. Surface Science 294: 409-419.

Kittel, C. 1996. Introduction to solid state physics. 7 th ed. New York: Wiley.

Koduvely, H. M., and Zangwill, A. 1999. Epitaxial growth kinetics with interacting coherent islands. Physical Review B 60: R2204-R2207.

Kohmoto, S., et al. 1999. Site-controlled self-organization of individual InAs quantum dots by scanning tunneling probe-assisted nanolithography. Applied Physics Letters 74: 3488-3490.

Korutcheva, E., Turiel A. M., and Markov, I. 2000. Coherent Stranski-Krastanov growth in 1+1 dimensions with anharmonic interactions: an equilibrium study. Physical Review B 61: 16890-16901.

LaBella, V. P., et al. 1999. Atomic structure of the GaAs(001)-(2x4) surface resolved using scanning tunneling microscopy and first-principles theory. Physical Review Letters 83: 2989-2993.

Landolt-Bernstein 1982. Numerical data and functional relationship in science and technology, O. Madelung (ed.) Berlin: Springer-Verlag.

Le Ru, E. C., et al. 2002. Strain and electronic interactions in InAs/GaAs quantum dot multilayers for 1300 nm emission. Journal of Applied Physics 91: 1365-1370.

Ledentsov, N. N., et al. 1996. Direct formation of vertically coupled quantum dots in Stranski-Krastanow growth. Physical Review B 54: 8743-8750.

Lee, H., et al. 1998. Determination of the shape of self-organized InAs/GaAs quantum dots by reflection high energy electron diffraction. Applied Physics Letters 72: 812-814.

Leonard, D., et al. 1993. Direct formation of quantum-sized dots from uniform coherent islands of InGaAs on GaAs surfaces. Applied Physics Letters 63: 3203-3205.

Lipinski, M. O., et al. 2000. MBE growth conditions for 1.3 μm light emission from InAs quantum dots. Proceeding of SPIE conference: 215-218.

Medeiros-Ribeiro, G., et al. 1998. Shape transition of germanium nanocrystals on a silicon (001) surface from pyramids to domes. Science 279: 353-355.

Meixner, M., et al. 2001. Self-assembled quantum dots: crossover from kinetically controlled to thermodynamically limited growth. Physical Review Letters 87: 236101-1 – 236101-4.

Merz, J. L., et al. 1999. Nanostructure self-assembly as an emerging technology. In S. Luryi, J. Xu, and A. Zaslavsky Future trends in microelectronics the road ahead New York: Wiley.

Morkoç, H., Sverdlov, B., and Gao, G.-B. 1993. Strained layer heterostructures, and their applications to MODFET's, HBT's, and Lasers. Proceedings of the IEEE 81: 493-556.

Mukhametzhanov, I., et al. 1999. Punctuated island growth: an approach to examination and control of quantum dot density, size, and shape evolution. Applied Physics Letters 75: 85-87.

Murray, R., et al. 1999. 1.3 μm room temperature emission from InAs/GaAs self-assembled quantum dots. Japanese Journal of Applied Physics 1 28 part 1: 528-530.

Nakata, Y., et al. 2000. Molecular beam epitaxial growth of InAs self-assembled quantum dots with light-emission at 1.3 μm. Journal of Crystal Growth 208: 93-99.

Nishi, K., et al. 1999. A narrow photoluminescence linewidth of 21 meV at 1.35 μm from strain-reduced InAs quantum dots covered by $In_{0.2}Ga_{0.8}As$ grown on GaAs substrates. Applied Physics Letters 74: 1111-1113.

O'Reilly, E. P., 1989. Valence band engineering in strained-layer structures. Semiconductors Science and Technology 4: 121-137.

Pan, E., and Yang, B. 2001. Elastostatic fields in anisotropic substrate due to a buried quantum dot. Journal of Applied Physics 90: 6190-6196.

Pimpinelli, A., and Villain, J. 1998. Physics of crystal growth Cambridge: Cambridge University Press.

Pistol, M.-E., et al. 1995. Observation of strain effects in semiconductor dots depending on cap layer thickness. Applied Physics Letters 67: 1438-1440.

Priester, C., and Lannoo, M. 1995 Origin of self-assembled quantum dots in highly mismatched heteroepitaxy. Physical Review Letters 75: 93-98.

Rajkumar, K. C. et al. 1992. Optically active three-dimensionally confined structures realized via molecular beam epitaxial growth on nonplanar GaAs (111)B. Applied Physics Letters 63: 2905-2907.

Ritz, M., Kaneko, T., and Eberl, K. 1997. The effect of surface reconstructions on the surface morphology during *in situ* etching of GaAs. Applied Physics Letters 71: 695-697.

Saito, H., Nishi, K., and Sugou, S. 1999. Shape transition of InAs quantum dots by growth at high temperature. Applied Physics Letters 74: 1224-1226.

Schmidt, O. G., et al. 2002 Self-assembled semiconductor nanostructures: climbing up the ladder of order. Surface Science 514: 10-18.

Schöll, E., and Bose, S. 1998. Kinetic Monte Carlo simulation of the nucleation stage of the self-organized growth of quantum dots. Solid-State Electronics 42: 1587-1591.

Schuler, H., et al. 2000. *In situ* etching with $AsBr_3$ and regrowth in molecular beam epitaxy. Semiconductor Science and Technology 15: 169-177.

Seifert, W., et al. 1996. In-situ growth of quantum dot structures by the Stranski-Krastanow growth mode. Progress in Crystal Growth and Characterization 33: 423-471.

Seifert, W., et al. 1999. Continuous and discontinuous metal-organic vapour phase epitaxy of coherent self-assembled islands effects on size homogeneity. Journal of Crystal Growth 197: 19-24.

Shchukin, V. A., et al. 1995. Spontaneous ordering of arrays of coherent strained islands. Physical Review Letters 75: 2968-2971.

Shchukin, V. A., and Bimberg, D. 1999. Spontaneous ordering of nanostructures on crystal surfaces. Reviews of Modern Physics 71: 1125-1171.

Songmuang, R., et al. 2003. Shape evolution of InAs quantum dots during overgrowth. Journal of Crystal Growth 249: 416-421.

Spencer, B. J., and Tersoff, J. 1997. Equilibrium shapes and properties of epitaxially strained islands. Physical Review Letters 79: 4858-4861.

Srolovitz, D. J., 1989. On the stability of surfaces of stressed solids. Acta Metallurgica 37: 621-625.

Sugawara, M., 1999. Theoretical based of the optical properties of semiconductor quantum nano-structures. In M. Sugawara (ed.), Semiconductors and Semimentals vol. 60: Self-assembled InGaAs/GaAs quantum dots, pp. 1-116, San Diego: Academic Press.

Tatebayashi, J., et al. 2001. Over 1.5 μm light emission from InAs quantum dots embedded in InGaAs strain reducing layer grown by metalorganic chemical vapor deposition. Applied Physics Letters 78: 3469-3471.

Tsao, J. Y., 1993. Materials fundamentals of molecular beam epitaxy Boston: Academic Press.

Vvedensky, D. D., 2001. Epitaxial growth of semiconductors. In K. Barnham and D. Vvensky (eds.) Low-dimensional semiconductor structures fundamentals and device applications Cambridge: Cambridge University Press.

Wang, L. G., and Zunger A. 1999. Linear combination of bulk bands method for large-scale electronic structure calculation on strained nanostructures. Physical Review B 59: 15806-15818.

Wang, L. G., et al. 2000. Size, shape, and stability of InAs quantum dots on the GaAs (001) substrate. Physical Review B 62: 1897-1904.

Wegscheider, W., et al. 1997. Atomically precise GaAs/AlGaAs quantum dots fabricated by twofold cleaved edge overgrowth. Physical Review Letters 79: 1917-1920.

Weisbuch, C., and Vinter, B. 1991. Quantum semiconductor structures fundamentals and applications. San Diego: Academic Press.

Wolfe, C. M., Holonyak, N., Jr., and Stillman, G. E. 1989. Physical properties of semiconductors. Englewood Cliffs, New Jersey: Prentice Hall.

Yamaguchi, K., et al. 2000. Stranski-Krastanov growth of InAs quantum dots with narrow size distribution. Japanese Journal of Applied Physics 39: L1245-L1248.

Yu, P. Y., and Cardona, M. 1999. Fundamentals of semiconductors: physics and materials properties. 2 nd ed. Berlin: Springer-Verlag.

Yu, H., Roberts, C., and Murray, R. 1995. The effects of In segregation on the emission properties of InGaAs/GaAs quantum wells. Material Science and Engineering B 35: 129-132.

Zhukov, A. E., et al. 2000. 3.5 W continuous wave operationfrom quantum dot laser. Materials Science and Engineering B 74: 70-74.

Zrenner, A., 2000. A close look on single quantum dots. Journal of Chemical Physics 112: 7790-7798.

APPENDIX A

The M-file script routines for AFM analysis.

The routine to analyses raw AFM data is divided into 3 files. They are

histo3.m ---	The routine to generate height and diameter data from each dot in a AFM scan.
afm.m ---	The routine to change the AFM data format from Nanoscope IIIa to MATLAB compatible format.
readDi2.m ---	The subroutine called by afm.m.

Note that: the readDi2.m and a part of afm.m were from the Digital Instrument engineer (Dr. Rohit Jain).

List of the routines:

histo3.m

```
% AFM-image analysis subroutine
% developed by Suwit Kiravittaya
%
clear;
file='63043';
load(file);
m=m*zsc/65536.;
minvalue = min(min(m));
recwidth1 = 14;         % recwidth1 when determine the position of
the QDs
recwidth2 = 16;         % recwidth2 when extract each dot
numdot = 1000;
for ii=1:numdot,
    [value(ii),index(ii,1)] = max(max(m));
    [value(ii),index(ii,2)] = max(m(:,index(ii,1)));
    % m(index(ii,2),index(ii,1)) is maximum
    for jj=1:recwidth1,
        jjj = index(ii,2)+jj-recwidth1/2;
              if ( jjj < 1 )
            jjj = 1;
        elseif ( jjj > 512 )
            jjj = 512;
        end
        for kk=1:recwidth1,
            kkk = index(ii,1)+kk-recwidth1/2;
            if ( kkk < 1 )
                kkk = 1;
            elseif ( kkk > 512 )
                kkk = 512;
            end
              if( sqrt((jj-recwidth1/2)^2+(kk-recwidth1/2)^2) <
recwidth1/2 )
                  m(jjj,kkk) = minvalue;
             end
        end
    end
```

```
end

imagesc(m)
title(cat(2,fname,'; Z range :
',num2str(zsc),zunit),'Interpreter','none');
xlabel(cat(2,num2str(xsiz),xunit,' : ',num2str(c),'
columns'),'Interpreter','none');
ylabel(cat(2,num2str(xsiz*r/c),xunit,' : ',num2str(r),'
rows'),'Interpreter','none');
grid; colorbar;

load(file);
m=m*zsc/65536.;
for ii=1:numdot,

x1 = index(ii,2)-recwidth2/2;
if (x1<1)
      x1=1;
end

x2 = index(ii,2)+recwidth2/2;
if (x2>512)
      x2=512;
end

dot = m(x1:x2,index(ii,1));
ddot = diff(dot);
[v1,ind1] = max(ddot);
[vm,indm] = max(dot);
baseind = ind1 - 1 ;           % minus 1 to compensate diff function
india = indm-baseind;
hdia(ii) = ((india)*2000.)/512.;
baseind = baseind - 2;  % change baseind to reach background height
if (baseind < 1)
      baseind = indm;
end

height(ii) = vm - dot(baseind);
end

numbaddot = 0;
for ii=1:numdot
      if hdia(ii) <= 0
            hdia(ii) = 0;
            height(ii) = 0;
            numbaddot = numbaddot + 1;
      elseif height(ii) <= 0
            height(ii) = 0;
            hdia(ii) = 0;
            numbaddot = numbaddot + 1;
      end
end
```

afm.m

```
% afm.m generates 2 data files i.e. [fname].DES and [fname].DAT.
% [fname].DES contain parameter of AFM scan and [fname].DAT contain
raw
% AFM data in MATLAB compatible format.

% get image name - image should be specified as a fully qualified
filename
%fname=input('Enter fully qualified filename --> ','s');
% or do it by a dialog
[fname,pname]=uigetfile('*.*','Plug Application');
fname=strcat(pname,fname)
% call read function
[m,zsc,zunit,xsiz,xunit]=readDi2(fname);
```

```
[r,c]=size(m);
% display the image
imagesc(m*zsc/65536);
title(cat(2,fname,'; Z range :
',num2str(zsc),zunit),'Interpreter','none');
xlabel(cat(2,num2str(xsiz),xunit,' : ',num2str(c),'
columns'),'Interpreter','none');
ylabel(cat(2,num2str(xsiz*r/c),xunit,' : ',num2str(r),'
rows'),'Interpreter','none');
grid; colorbar;
% allow x,y,z display on mouse-click
set(findobj(gcf,'type','image'),'ButtonDownFcn','im_pos');
fid1 = fopen(cat(2,fname,'.DES'),'W');
fprintf(fid1,'Source file: %s\n',fname);
fprintf(fid1,'x size (unit): (%s)\n',xunit);
fprintf(fid1,'%s\n',num2str(xsiz));
fprintf(fid1,'z size (unit): (%s)\n',zunit);
fprintf(fid1,'%s\n',num2str(zsc));
fprintf(fid1,'number of row\n');
fprintf(fid1,'%s\n',num2str(r));
fprintf(fid1,'number of column\n');
fprintf(fid1,'%s\n',num2str(c));

fclose(fid1);


fid2 = fopen(cat(2,fname,'.DAT'),'W');
% r = row index , c = column index
for i=1:r,
      for j=1:c,
            fprintf(fid2,'%7d',m(i,j));
      end
            fprintf(fid2,'\n');
end
fclose(fid2);
```

readDi2.m

```
function [m,sc,unit,xsiz,xunit]=readDi2(file_name)
% readDi - reads DI image files
% input is file_name: a fully qualified filename in single quotes
% outputs are m : image data matrix
%             sc : z scale
%             unit : z units
%             xsiz : x and y scale
%             xunit : x and y units
if isempty(file_name)
   error('File not found')
end
% read input file as text
fin = fopen(file_name,'r');
if fin == -1
   error('File could not be opened');
end
line=fgets(fin);
% new technique
flag=0; do1=1;
while flag == 0
   [token,rem]=strtok(line);
   if strncmp(line,'\@2:Z scale:',12)
      flag=1;
      [nfac1,rem]=strtok(rem,'[');
      [nfac1,rem]=strtok(rem,']');
      nfac1=strcat('\@',nfac1(2:length(nfac1)),':');
      [fac2,rem]=strtok(rem,')');
      fac2=str2num(strtok(rem(3:length(rem)-3)));
   elseif strncmp(line,'\Z scale:',9)
      flag=2;
      [sc,rem]=strtok(rem);
      [sc,unit]=strtok(rem);
      sc=str2num(sc);
      unit=strtok(unit);
   elseif strncmp(line,'\Data offset:',13)
      [token,offset]=strtok(rem,':');
      offset=str2num(offset(2:length(offset)));
   elseif strncmp(line,'\@Sens. Zscan:',14)
      [zscan,rem]=strtok(rem,'V');
      [zscan,zscanunit]=strtok(rem(3:(length(rem)-4)));
      zscan=str2num(zscan);
   elseif strncmp(line,'\@Sens. LinZ:',13)
      [zlin,rem]=strtok(rem,'V');
      [zlin,zlinunit]=strtok(rem(3:length(rem)-4));
      zlin=str2num(zlin);
   elseif strncmp(line,'\Samps/line:',12)
      c=str2num(rem);
   elseif strncmp(line,'\Number of lines:',17)
      [token,rem]=strtok(rem,':');
      r=str2num(rem(3:length(rem)));
   elseif strncmp(line,'\Valid data len',15)
      axis=line(17);
      if axis == 'Y'
         [token,c]=strtok(rem,':');
         c=str2num(c(2:length(c)));
      else
         [token,r]=strtok(rem,':');
         r=str2num(r(2:length(r)));
      end
   elseif (do1 & strncmp(line,'\Scan size:',11))
      [token,rem]=strtok(rem);
      [xsiz,xunit]=strtok(rem);
      xsiz=str2num(xsiz);
      do1=0;
   end
   line=fgets(fin);
end
```

```
if flag == 1
   if strncmp(nfac1,'\@Sens. Zscan:',14)
      sc=fac2*zscan; unit=zscanunit;
   elseif strncmp(nfac1,'\@Sens. LinZ:',13)
      sc=fac2*zlin; unit=zlinunit;
   else
      error(strcat('Z scale reference is: ',nfac1));
   end
end

fclose(fin);
% read input file as binary
fin = fopen(file_name,'rb');
status=fseek(fin,offset,'bof');
[m,n] = fread(fin,[r,c],'int16'); % 16 bit signed integers
fclose(fin);
unit=unit(double(unit) > 30);
xunit=xunit(double(xunit) > 30);
% rotate so MATLAB imagesc function displays similar to DI software
m=rot90(m);
```

List of Publications

1. International Journals and International Conferences

1. **Suwit Kiravittaya**; Uttachai Manmontri; Suwat Sopitpan; Somchai Ratanathammaphan; Choompol Antarasen; Montri Sawadsaringkarn; and Somsak Panyakeow. 1998. AlGaAs/GaAs/InGaAs composite MQW structures for photovoltaic applications. Proceedings of the 2nd World Conference and Exhibition on Photovoltaic Solar Energy Conversion 3617-3620.

2. **Suwit Kiravittaya**; Rudeesun Songmuang; Supachok Thainoi; Suwat Sopitpan; Songphol Kanjanachuchai; Somchai Ratanathammaphan; Montri Sawadsaringkarn; and Somsak Panyakeow. 2000. Self-assembled composite quantum dots for photovoltaic applications. Proceedings of the 28th IEEE Photovoltaic Specialists Conference 818-821.

3. **Suwit Kiravittaya**; Uttachai Manmontri; Suwat Sopitpan; Somchai Ratanathammaphan; Choompol Antarasen; Montri Sawadsaringkarn; and Somsak Panyakeow. 2001. AlGaAs/GaAs/InGaAs composite MQW structures for photovoltaic applications. Solar Energy Material and Solar Cells 68: 89-95.

4. **Suwit Kiravittaya**; Rudeesun Songmuang; Pornchai Changmuang; Suwat Sopitpan; Somchai Ratanathammaphan; Montri Sawadsaringkarn; and Somsak Panyakeow. 2001. InAs/GaAs self-organized quantum dots on (411)A GaAs by molecular beam epitaxy. Journal of Crystal Growth 227-228: 1010-1015.

5. Rudeesun Songmuang; **Suwit Kiravittaya**; Supachok Thainoi; Pornchai Changmuang; Suwat Sopitpan; Somchai Ratanathammaphan; Montri Sawadsaringkarn; and Somsak Panyakeow. 2001. Selective growth of InAs/GaAs self-organized quantum dots by shadow mask technique. Journal of Crystal Growth 227-228: 1053-1056.

6. **Suwit Kiravittaya**; Nakamura, Y.; and Schmidt, O. G. 2002. Photoluminescence linewidth narrowing of InAs/GaAs self-assembled quantum dots. Physica E 13: 224-228.

7. Heidemeyer, H.; **Suwit Kiravittaya**; Müller, C.; Jin-Phillip, N. Y.; and Schmidt, O. G. 2002. Closely stacked InAs/GaAs quantum dots grown at low growth rate. Applied Physics Letters 80: 1544-1546.

8. Nakamura, Y.; Schmidt, O. G.; Jin-Phillip, N. Y.; **Suwit Kiravittaya**; Müller, C.; Eberl, K.; Gräbeldinger, H.; and Schweizer, H. 2002. Vertical alignment of laterally ordered InAs and InGaAs quantum dot arrays on patterned (001) GaAs substrates. Journal of Crystal Growth 242: 339-344.

9. Schmidt, O. G.; **Suwit Kiravittaya**; Nakamura, Y.; Heidemeyer, H.; Rudeesun Songmuang; Müller, C.; Jin-Phillip, N. Y.; Eberl, K.; Wawra, H.; Christiansen, S.; Gräbeldinger, H.; and Schweizer, H. 2002 Self-assembled semiconductor nanostructures: climbing up the ladder of order. Surface Science 514: 10-18.

10. **Suwit Kiravittaya**; Rudeesun Songmuang; and Schmidt, O. G. 2002. Self-assembled quantum dots and nanoholes by molecular beam epitaxial growth and atomically precise *in situ* etching. Proceedings of the Material Research Society Symposium 722: K10.11.1-6.

11. Schmidt, O. G.; Deneke, C.; **Suwit Kiravittaya**; Rudeesun Songmuang; Heidemeyer, H.; Nakamura, Y.; Zapf-Gottwick, Y.; Müller, C.; and Jin-Phillip, N. Y. 2002. Self-assembled nanoholes, lateral quantum-dot molecules, and rolled-up nanotubes. IEEE Journal of Selected Topics in Quantum Electronics 8: 1025-1034.

12. Suraphol Kamprachum; **Suwit Kiravittaya**; Rudeesun Songmuang; Supachok Thainoi; Songphol Kanjanachuchai; Montri Sawadsaringkarn; and Somsak Panyakeow. Multi-stacked quantum dots with graded dot sizes for photovoltaic applications. Proceedings of the 29th IEEE Photovoltaic Specialists Conference (in press).

13. Rudeesun Songmuang; **Suwit Kiravittaya**; and Schmidt, O. G. 2003. Shape evolution of InAs quantum dots during overgrowth. Journal of Crystal Growth 249: 416-421.

14. **Suwit Kiravittaya**; Rudeesun Songmuang; Jin-Phillip, N. Y.; Panyakeow, S.; and Schmidt, O. G. Self-assembled nanoholes and lateral QD bi-molecules by molecular beam epitaxy and atomically precise *in situ* etching. Journal of Crystal Growth (in press).

15. Rudeesun Songmuang; **Suwit Kiravittaya**; Montri Sawadsaringkarn; Somsak Panyakeow; and Schmidt, O. G. Photoluminescence investigation of low temperature capped self-assembled InAs/GaAs quantum dots. Journal of Crystal Growth (in press).

16. Rudeesun Songmuang; **Suwit Kiravittaya**; and Schmidt, O. G. Formation of lateral quantum dot molecules around self-assembled nanoholes. Applied Physics Letters (in press).

2. Domestic Journals and Domestic Conferences

1. **Suwit Kiravittaya**; Suwat Sopitpan; Somchai Ratanathammaphan; Montri Sawadsaringkarn; and Somsak Panyakeow. 1998. The study of AlGaAs/GaAs/InGaAs composite quantum well (CQW) structure. Proceedings of the 21st Electrical Engineering Conference 123-126.

2. **Suwit Kiravittaya**; Montri Sawadsaringkarn; and Somsak Panyakeow. 2000. Single electron transistor: theory and applications. Research and Development Journal, The Engineering Institute of Thailand 11: 20-27.

3. **Suwit Kiravittaya**; Montri Sawadsaringkarn; and Somsak Panyakeow. 2000. Quantum dots structure for optoelectronic devices. Proceedings of RGJ-Ph.D. Congress I 144.

4. **Suwit Kiravittaya**; Rudeesun Songmuang; Montri Sawadsaringkarn; and Somsak Panyakeow. 2000. *In-situ* RHEED investigation of MBE-grown InAs QDs on (0 0 1) GaAs epilayer. Proceedings of the 23rd Electrical Engineering Conference 689-692.

5. Rudeesun Songmuang; **Suwit Kiravittaya**; Montri Sawadsaringkarn; and Somsak Panyakeow. 2000. InAs/GaAs, InGaAs/GaAs, and InAs/InGaAs/GaAs composite quantum dots. Proceedings of the 23rd Electrical Engineering Conference 685-688.

6. Rudeesun Songmuang; **Suwit Kiravittaya**; Montri Sawadsaringkarn; and Somsak Panyakeow. 2002. The growth of InAs self-organized quantum dots by molecular beam epitaxy. Research and Development Journal, The Engineering Institute of Thailand 13: 34-41.

7. **Suwit Kiravittaya**; Rudeesun Songmuang; Montri Sawadsaringkarn; and Somsak Panyakeow. 2002. Kinetic Monte Carlo simulation of molecular beam epitaxial growth. Proceedings of the 25th Electrical Engineering Conference EL134-EL138.

List of Presentations

1. International Presentations

- *Poster presentation*

  Suwit Kiravittaya; Rudeesun Songmuang; Pornchai Changmuang; Suwat Sopitpan; Somchai Ratanathammaphan; Montri Sawadsaringkarn; and Somsak Panyakeow. InAs/GaAs self-organized quantum dots on (411)A GaAs by molecular beam epitaxy. The 11th International Conference on Molecular Beam Epitaxy, Beijing, China, September 10-15 (2002).

- *Poster presentation*

  Suwit Kiravittaya; Nakamura, Y.; and Schmidt, O. G. Photoluminescence linewidth narrowing of InAs/GaAs self-assembled quantum dots. The 10th International Conference on Modulated Semiconductor Structures, Linz, Austria, July 23-27 (2001).

- *Poster presentation*

  Rudeesun Songmuang; **Suwit Kiravittaya**; Montri Sawadsaringkarn; Somsak Panyakeow; and Schmidt, O. G. Photoluminescence investigation of low temperature capped self-assembled InAs/GaAs quantum dots. The 12th International Conference on Molecular Beam Epitaxy, San Francisco, U.S.A., September 16-20 (2002).

- *Oral presentation*

  Suwit Kiravittaya; Rudeesun Songmuang; Jin-Phillip, N. Y.; Somsak Panyakeow; and Schmidt, O. G. Self-assembled nanoholes and lateral QD bi-molecules by molecular beam epitaxy and atomically precise *in situ* etching. The 12th International Conference on Molecular Beam Epitaxy, San Francisco, U.S.A., September 16-20 (2002).

2. Domestic Presentations

- *Oral presentation*

  Suwit Kiravittaya; Suwat Sopitpan; Somchai Ratanathammaphan; Montri Sawadsaringkarn; Somsak Panyakeow. The study of AlGaAs/GaAs/InGaAs composite quantum well (CQW) structure. The 21st Electrical Engineering Conference, King Mongkut's University of Technology Thonburi, Bangkok, November 12-13 (1998).

- *Oral presentation*

  Suwit Kiravittaya; Montri Sawadsaringkarn; and Somsak Panyakeow. Quantum dot structure for optoelectronic devices. RGJ-Ph.D. Congress I, Felix hotel, Kanjanaburi, May 2-4 (2000).

- *Oral presentation*

  Suwit Kiravittaya; Rudeesun Songmuang; Montri Sawadsaringkarn; and Somsak Panyakeow. *In-situ* RHEED investigation of MBE-grown InAs QDs on (0 0 1) GaAs epilayer. The 23rd Electrical Engineering Conference, Empress hotel, Chiang-Mai, November 23-24 (2000).

- *Oral presentation*

  Suwit Kiravittaya; Montri Sawadsaringkarn; Somsak Panyakeow; and Schmidt, O. G. Homogeneity improvement of self-assembled InAs/GaAs quantum dots. RGJ-Meeting, Chulalongkorn University, Bangkok, November 19 (2002).

- *Oral presentation*

  Suwit Kiravittaya; Rudeesun Songmuang; Montri Sawadsaringkarn; and Somsak Panyakeow. Kinetic Monte Carlo simulation of molecular beam epitaxial growth. The 25th Electrical Engineering Conference, Prince of Songkla University, Songkla, November 21-22 (2002).

VITAE

Suwit Kiravittaya was born in Bangkok, Thailand on December 20, 1976. In June 1994, he entered Chulalongkorn University and received the Bachelor of Engineering in Electrical Engineering Program in May 1998.

He entered the Graduate School of Chulalongkorn University in June 1998, as a Ph.D. student. His work is financial supported by National Science and Technology Development Agency (NSTDA) through “Sis Kon Kuti” Program. Since December 1998, he has received Royal Golden Jubilee Scholarship from Thailand Research Fund.

Between October 1999 and December 1999, he was sent to the Universität der Bundeswher, Munich, Germany and Max-Planck-Institute for Solid State Research, Stuttgart, Germany for doing a short research program.

Between December 2000 and April 2002, he received the DAAD-RGJ Scholarship and worked as a guest scientist in Max-Planck-Institute for Solid State Research, Stuttgart, Germany. His research activity there is the growth of self-assembled quantum dots as well as study and maintain molecular beam epitaxy machine.